FACULTY
OF MATHEMATICS
AND PHYSICS
Charles University

DOCTORAL THESIS

Rostislav Králík

Influence of Sc on properties of model Al-Li-based alloys prepared by twin-roll casting

Department of Physics of Materials

Supervisor of the doctoral thesis: doc. RNDr. Miroslav Cieslar, CSc.

Study programme: Physics

Specialization: Physics of Condensed Matter and Materials Research

Prague 2024

I declare that I carried out this doctoral thesis independently and only with the cited sources, literature, and other professional sources. It has not been used to obtain another or the same degree.

I understand that my work relates to the rights and obligations under the Act No. 121/2000 Sb., the Copyright Act, as amended, in particular, the fact that the Charles University has the right to conclude a license agreement on the use of this work as a school work pursuant to Section 60 subsection 1 of the Copyright Act.

In . . . . date . . . .

Author’s signature

My thanks belong to Oleksandr Grydin of the University of Paderborn for providing us with the twin-roll cast materials, his warm welcome and mentorship during my stay there, and seamless scientific cooperation throughout the years. Furthermore, I would like to thank Vladivoj Očenášek of SVÚM a.s. for his work on manufacturing the mold-cast products and Ján Škoviera and the Slovak Academy of Sciences for manufacturing the melt-spun strips.

Gratitude and high praise should also be extended to all those at the Department of Physics of Materials responsible for keeping the place running, especially those responsible for the individual laboratories. Most of all, I would like to thank Miroslav Cieslar for his leadership and patience.

I want to give special thanks to my wife, Martinka Králíková, who has kept me sane for the last nine years and was endlessly patient during Spring 2024 when this work was being finalized.

Title: Influence of Sc on properties of model Al-Li based alloys prepared by twin-roll casting

Author: RNDr. Rostislav Králík

Department: Department of Physics of Materials

Supervisor: doc. RNDr. Miroslav Cieslar, CSc.

Abstract: The solidification rate of high-strength aluminum alloys strongly impacts the cast structure. The size of eutectic cells could be reduced from several hundred micrometers, typical for ingot-cast materials, down to sub-micrometer size in rapidly solidified materials. Finer initial microstructures reduce the necessary high-temperature homogenization holding times, detrimental to some beneficial dispersoid-forming microalloying elements. A typical example is Sc, which positively influences the formation of fine-grained structures in post-processed materials. However, it is prone to coarsening and a loss of the beneficial effects at high temperatures. Two Al-Cu-Li-Mg-Zr-based alloys, one with an addition of Sc, were conventionally ingot-cast, twin-roll cast, and melt-spun. A relationship between solidification kinetics and the size of the eutectic cells was established, and a significant homogenization holding time reduction was confirmed. A model processing route based on physical metallurgy was proposed. The beneficial effects of Sc on texture, fine-grained structure, and mechanical properties were fully exploited and confirmed.

Keywords: Al-Cu-Li-Mg-Zr-(Sc), twin-roll casting, rapid solidification, age hardening, mechanical properties

Název práce: Vliv Sc na mikrostrukturu a vlastnosti plynule odlévaných modelových slitin na bázi Al-Li

Autor: RNDr. Rostislav Králík

Katedra: Katedra fyziky materiálů

Vedoucí práce: doc. RNDr. Miroslav Cieslar, CSc.

Abstrakt: Rychlost tuhnutí vysokopevnostních hliníkových slitin má zásadní vliv na jejich strukturu v litém stavu. Velikost eutektických buněk může být snížena z několika stovek mikrometrů typických pro standardní materiály odlité ve formě ingotu, až pod jeden mikrometr v případě materiálů odlitých metodami rychlého tuhnutí. Jemnější počáteční struktura zkracuje vysokoteplotní homogenizaci, což umožňuje využití příznivého vlivu některých legur tvořících disperzoidy. Typickým příkladem je Sc, které má příznivý účinek na zjemňování struktury zrn ve finálně zpracovaných materiálech. Při vystavení vysokým teplotám žíhání částice Sc hrubnou, čímž ztrácí svůj pozitivní vliv. V předložené práci byly studovány dvě slitiny na bázi Al-Cu-Li-Mg-Zr, přičemž jedna ze slitin obsahuje přídavek Sc. Slitiny byly odlity konvenčně ve formě ingotu, metodou plynulého odlévání mezi válce a metodou rychlého tuhnutí na rotujícím válci. Studiem těchto slitin byl ustanoven vztah mezi rychlostí tuhnutí a velikostí eutektických buněk a byla potvrzena možnost zásadního zkrácení délky homogenizačního žíhání. Na základě studia metodami fyzikální metalurgie bylo navrženo a validováno nové schéma zpracování těchto slitin které plně využívá pozitivního vlivu Sc na jejich texturu, velikost zrn a mechanické vlastnosti.

Klíčová slova: Al-Cu-Li-Mg-Zr-(Sc), plynulé odlévání mezi válce, metody rychlého tuhnutí, precipitační vytvrzování materiálu, mechanické vlastnosti

Preface

The development of Al alloys with the addition of lithium began in the late 50s, driven mainly by the aerospace industry in search of materials with high strength and good fatigue properties while having low density, thus leading to savings in fuel consumption.

Early Al-Li-based alloys carried notable drawbacks – crack deviation caused by planarity of slip, anisotropy of mechanical properties, low fracture toughness, and poor thermal stability of mechanical properties. Decades of adjustments of alloying element contents and thermomechanical processing have led to the refinement of the favorable mechanical properties while reducing the harmful intrinsic faults to a point where the AA2195 alloy has found use as a material for the construction of a super lightweight fuel tank of space shuttles.

These materials were traditionally direct-chill cast, an ingot casting method producing billets with several decimeters or meters dimensions. An alternative could come from continuously cast materials, such as those manufactured by the twin-roll casting method. Twin-roll casting can produce sheet materials that are almost net-shaped and only several millimeters thick. Still, the difference in solidification kinetics causes a disparity between as-cast state microstructures and the required thermomechanical post-processing. Similarly, rapid solidification casting methods such as melt spinning could produce these alloys as various functional materials.

Finer microstructures associated with higher solidification rates of twin-roll casting and rapid solidification methods could open up an avenue for using previously unviable alloying elements, such as scandium. Scandium is known for its positive effects on recrystallization kinetics, grain refinement, and strengthening. However, the positive impact of scandium requires the formation of fine Al-Sc-based dispersoids, which coarsen and lose their benefits during traditional high-temperature and long-term thermal processing typical for ingot-cast materials. Casting methods that do not require these high temperature/long holding times processing steps may be the solution for developing materials fully exploiting the potential of Sc alloying.

1. The current state of research

1.1. Al-based systems

Aluminum is the most abundant metal in the Earth's crust, the third most abundant element, second only to oxygen and silicon [1]. Aluminum alloys are the second most used metallic material, second only to steel. Their wide use is due to their low density, good formability, thermal and electric conductivity, and relatively low price [2]. The low density makes them a desirable material for the aerospace and automotive industries.

The present study focuses on the influence of solidification conditions on the microstructure and processing of Al-Cu-Li-Mg-Zr-based alloys and the role of Sc addition. The studied alloys are based on the AA2195 alloy [2] with a reduced total alloying element content. The materials are characterized by a high Cu/Li ratio, standard in modern Al alloys containing Li, where the main strengthening effect originates from Al_2CuLi precipitates.

1.1.1. Al-Li system

A significant advantage of Li addition to aluminum alloys is their lower total density, with Li being the lightest metal. The addition of 1 wt. % causes an average 3 % decrease in density and a 6-8 % increase of elastic modulus if present in binary strengthening precipitates [3-6]. The primary strengthening precipitate in binary Al-Li systems is the metastable Al_3Li (δ') phase – a small spherical coherent strengthening precipitate with the cubic $L1_2$ structure. While a significant contributor to the total strengthening of the early generation of Al-Li-based alloys, it is easily shearable and leads to the activation of coplanar slip and the formation of slip bands during deformation. These effects deteriorate specific properties, such as fracture toughness [3]. Kumar and Heubaum [7] studied alloys with varying concentrations of Li and Cu content between 5.0 and 6.5 wt. %. They found that the strength of alloys increases with increasing Li content up to 1.3 wt. % and decreases again with higher concentrations regardless of other additions (including Ag, Mg, and Zr, all of which are present in the studied materials). While this study does show the harmful effects of high Li content, it only attributes this to a change in the ratio of binary Al-Cu/binary Al-Li precipitates above a certain Li content (0.5 wt. %). However, it ignores the formation of possible ternary Al-Cu-Li phases. They assumed ternary Al-Cu-Li phase precipitation kinetics become competitive with binary phases only after plastic deformation before artificial aging. This fact was confirmed by Gable et al. [8], who observed a three times increase in ternary Al-Cu-Li phase number fraction with a 2 % pre-stretch before aging.

The eutectic composition in the Al-rich corner is 9.9 wt. % lithium, and the eutectic temperature is 600 °C. Li has a high solubility in Al, with a maximum of 5.2 wt. % at eutectic temperaure [2] (Figure 1.1). The solubility of Li decreases only slowly with decreasing temperature. At 500 °C, the solubility of Li in Al is around four wt. %. This percentage is much higher than the usual Li content in Al-Cu-Li-based alloys, allowing solution treatments above this temperature to redistribute Li content into the matrix quickly. The diffusivity coefficient of Li in Al at 510 °C is $2.97.10^{-9}$ $cm^2 \cdot s^{-1}$ for 1.9 wt. % Li content [9].

The stable binary Al-Li phase is the δ phase, which has a face-centered cubic structure [10]. The lattice mismatch between the δ phase and the aluminum matrix is too high for the phase to be coherent. It forms primarily through heterogeneous nucleation on grain boundaries and other material defects. The phase forms at higher annealing temperatures and longer holding times after the entire dissolution of the metastable δ' phase [11].

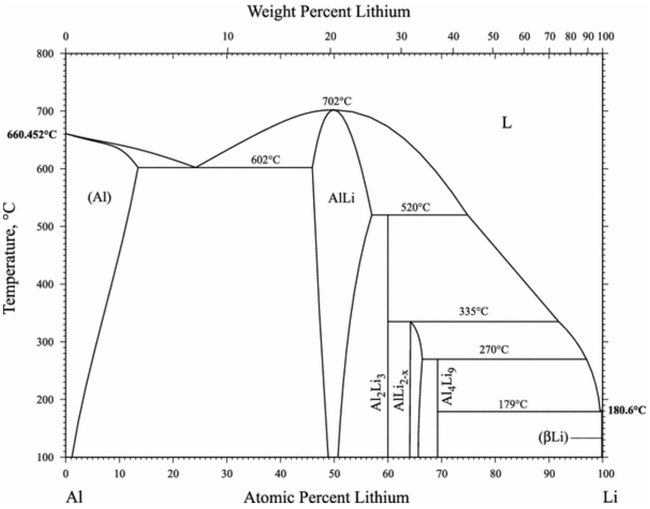

Figure 1.1: Al-Li binary phase diagram [12].

1.1.2. Al-Cu system

Al alloys containing Cu as a primary strengthening element form the basis of the 2XXX system [2]. Like the Al-Li system, the Al-Cu system is eutectic in the Al-rich corner with an eutectic temperature of 548 °C and an eutectic composition of 33.2 wt. % Cu. The non-stochiometric Al_2Cu θ phase forms the other side of the Al-rich eutectic system (Figure 1.2) [2].

The θ phase has a specific precipitation sequence from a supersaturated solid solution (SSSS), the coherent parts of which contribute significantly to material strengthening. The highest strengthening effect per atom is reached through the precipitation of so-called Guinier-Preston (GP) zones, whose thickness is between a single atom plane and several nanometers [13,14]. GP zones form from clusters of increased Cu concentration, which aggregate in the supersaturated matrix even at room temperatures [15]. However, these clusters are unstable and generally not promoted by the thermomechanical processing of standard alloys. There are four stages of Al_2Cu precipitation in total. GP1 and GP2 are coherent and formed by singular (GP1) or multiple (GP2) Cu layers. High-resolution transmission electron microscopy (HRTEM) image of a GP1 and GP2 zone in an Al-Cu-Li-based alloy is shown in Figure 1.3 [16]. GP2 zones grow from GP1 zones. The Cu layers in GP1 and GP2 zones are formed along the $\{100\}_{Al}$ matrix planes. GP2 zones are formed by consecutive Cu layers separated by three Al layers. They are also occasionally called the θ'' (Al_3Cu) phase since they, in principle, contain long-range ordering and have a definite local crystal structure [17]. This structure is also confirmed to be the ground state of coherent precipitation in Al-Cu systems by calculations from the first principles [18]. However, experimental observations using atomic resolution TEM have shown GP2 zones with at most three consecutive Cu layers [15,19]. The formation of GP2 zones from GP1 zones necessitates forming a new Cu layer within three Al layers of the first, making it essentially a coarsening reaction of a GP1 zone. However, it appears as a two-stage reaction due to the relative increase of local Cu content and the diffusion required to facilitate it. The transition is a competition between decreased ordering energy and increased interfacial energy [17,20]. Higher temperatures of isothermal annealing and longer aging times lead to forming θ' and, consequently, θ phases from GP zones. Both phases have the same composition - Al_2Cu but differ in structure. Whereas the θ' is a semi-coherent precipitate (with coherency about the (100) plane) with a tetragonally distorted structure of cubic fluorite, the θ phase is incoherent with a tetragonal I4/mcm structure [17,21]. The θ' phase has a specific orientation relationship with the Al matrix originally proposed by Silcock et al. [22]:

$$(100)_{Al}//(100)_{\theta'},\ [001]_{Al}//[001]_{\theta'}.$$

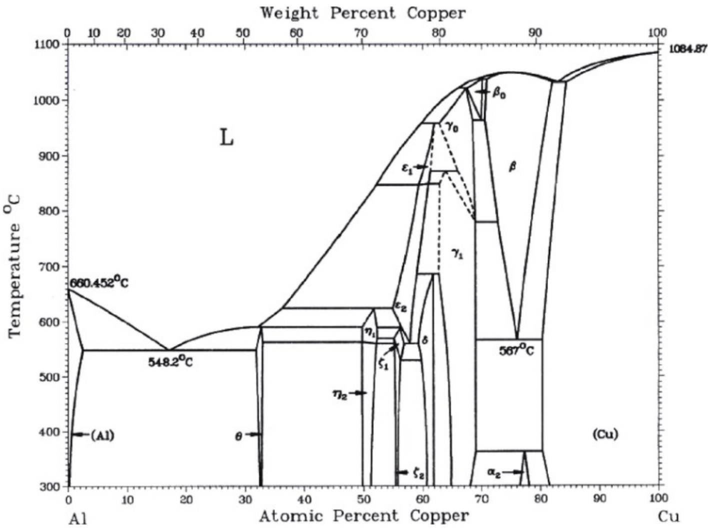

Figure 1.2: The Al-Cu binary phase diagram [23].

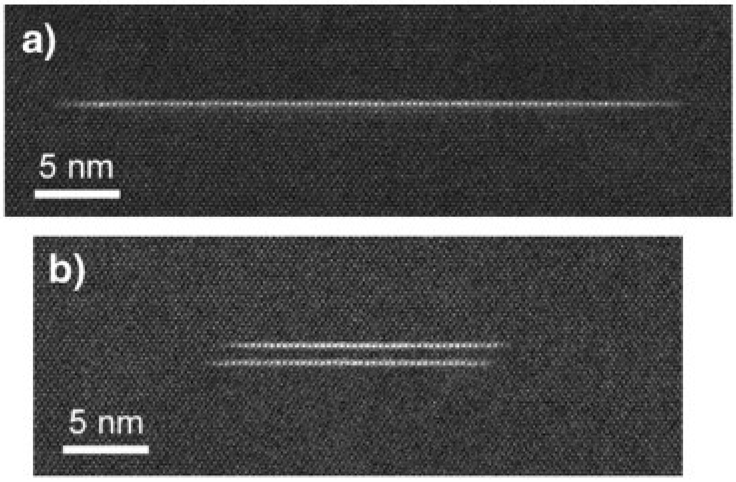

Figure 1.3: HRTEM of GP1 and GP2 zones [16].

The θ' precipitates form rectangular or octagonal plates on {100} Al matrix planes. A complete θ' to θ transformation carries a significant decrease in material hardness due to the loss of coherency, and it is essential to prevent it when considering material processing. The complete precipitation sequence in Al-Cu alloys can be written as:

$$\mathrm{SSSS} \rightarrow \mathrm{Cu-rich\ clusters} \rightarrow \mathrm{GP1} \rightarrow \mathrm{GP2}\ (\theta'') \rightarrow \theta'\mathrm{Al_2Cu} \rightarrow \theta\ \mathrm{Al_2Cu}.$$

The highest hardness is reached when a balance between the two mechanisms of dislocation motion past precipitates – the Orowan mechanism of looping and particle cutting - is reached. This balance applies to any particle and, in the Al-Cu system, corresponds to a time/temperature treatment (typically at temperatures no higher than 180 °C), which produces a coexistence of coherent and semi-coherent precipitates [15]. θ' strengthening contribution can be estimated using a modified Orowan-Ashby equation proposed by Bahl et al. [24]

$$\sigma_{OR} = \frac{MGb}{2\pi\sqrt{1-\upsilon}}\left(\frac{1}{\lambda}\right)\ln\left(\frac{0.981\sqrt{dt_p}}{b}\right), \tag{1.1}$$

where d and t_p are precipitate diameter and thickness, G is shear modulus (25.4 GPa for Al), b is the Burgers vector (0.286 nm), υ is the Poisson ratio (0.33), M is the Taylor factor (~ 3.06 in FCC materials), and λ is interparticle spacing, which can be calculated as:

$$\lambda = 1.23\frac{1.03}{\sqrt{f_N d}} - \frac{\pi d}{8} - 1.061 t_p\,. \tag{1.2}$$

f_N is the particle number fraction defined as the number of θ' particles per unit sample volume.

Al-Cu-based alloys played a crucial part in the development of aerospace alloys from the very beginning, being present even in the very first Wright flyer and in the development of understanding precipitation hardening as a whole [21,25]. Some key questions are still open regarding the mechanisms of their stabilization, which leads to the unique mechanical properties they provide [14], especially when vacancies are considered, as they are the main facilitators of diffusion necessary for the formation of solute clusters and, subsequently GP1 zones in the Al matrix. Interstitial diffusion is theoretically possible, but the energy for forming interstitial atoms is at least an order of magnitude higher than the energy needed for vacancy formation [15,26,27]. A high concentration of solute atoms participates in diffusion, formation of clusters, and subsequent precipitation, which results from solution treatment, which is done at temperatures that provide maximum solubility of Cu in the matrix. Solution treatment temperatures are generally selected close to 547 °C, which is the temperature of maximum Cu solubility in Al. Quenching from this temperature also introduces a high density of thermal vacancies [15]. These vacancies immediately contribute to the decomposition of the quenched solid solution, forming solute clusters and GP1 zones, as shown by the positron-annihilation spectroscopy experiments of Elsayed et al. [15]. They concluded that most (about 80 %) of GP1 zones contain structural vacancies to compensate for the Cu-lean conditions of their growth. TEM observations also confirm the presence of structural vacancies [18]. However, they are not present in the Cu layers of GP2 zones at higher temperatures. The study by Elsayed et al. [15] states that the dissolution range of θ' precipitates is between 400 °C and 460 °C and the dissolution range of θ precipitates between 520 °C and 540 °C. These temperatures are crucial when designing thermal processing schemes for Al-Cu-X-based materials. At 500 °C, the diffusion coefficient of Cu in Al is around 4.10^{-10} $cm^2 \cdot s^{-1}$ [28] - an order of magnitude lower than the Li and Mg diffusion coefficients.

1.1.3. Al-Cu-Li system

Numerous phases can precipitate in low alloyed Al-Cu-Li-based systems. In the context of Al-Cu-Li alloys, they are denoted as T-type phases. The T_1 phase is the principal strengthening semicoherent precipitate in these alloys. Undesirable incoherent phases (T_2, T_B) can also be present, mainly at the grain boundaries of the material [16].

The T_1 phase (Al_2CuLi) has a hexagonal structure with p6/mmm symmetry and forms platelets on {111} planes of the Al matrix. High-resolution TEM showed that the structure consists of a central Li-rich layer, and a close-packed arrangement of Li and Al with a 2:1 ratio formed by a Cu-rich bilayer, and a layer of non-close-packed Al and Cu atoms with a 1:1 ratio [29]. The structure is bounded by a corrugated, close-packed, ordered Al-Cu-Li layer. The corrugated layer has a minimal lattice mismatch with the Al matrix, allowing coherency even at large platelet extensions [30].

Generally, the T_1 phase does not precipitate homogeneously. Precipitation models for the T_1 phase rely on the presence of dislocations as nucleation centers. An increased density of dislocations and their overlapping diffusion fields lead to a more homogeneous formation and smaller size of T_1 [8,16]. The thin platelets of the hexagonal phase nucleate on stacking faults of the {111} Al matrix planes. The stacking fault forms by dissociating a perfect 1/2 <110> matrix dislocation into partial 1/6 <112> dislocations. Dissociation occurs at the opposite sides of a jog or a cross-slipped screw dislocation. The concentration of these jog/cross-slipped screw elements is crucial for the kinetics of T_1 precipitation [31]. This type of formation is called stacking fault precipitation and is common in several other Al-based systems, such as Al-Ag and Al-Mg-Zn [31].

However, the stacking fault energy (SFE) of Al is high, and the formation of dissociated dislocations is less probable. Adding elements that reduce SFE in Al (Mg, Ag) improves the precipitation kinetics of T_1 [16,31,32]. Al-Cu-Li-based alloys, including standard AA2195-type alloys, often contain small additions of these elements (< 1 wt. %). Recovered dislocations are formed into lower-energy configurations, cells, and subgrains, making subgrain boundaries suitable locations for T_1 precipitation. Grain refining additions can lower the average subgrain size, creating a more homogeneous dispersion of subgrain boundary-bound T_1 plates [33]. This synergy highlights the influence of proper homogenization treatment, which promotes a homogeneous distribution of grain refining phases, the retarding forces of grain growth, and by extension, the homogeneity of subgrain distribution [34].

Total content and Li/Cu ratios are essential in precipitation kinetics and the total influence on the mechanical properties of the material. The contribution to strengthening by T_1 precipitates was estimated by Dorin et al. [35] as

$$\sigma_{OR} = \frac{1.211 d \gamma^{\frac{3}{2}}}{{t_p}^2} \sqrt{\frac{b f_V}{\Gamma}} \, , \tag{1.3}$$

where d is the precipitate diameter, t_p is the precipitate thickness, and γ is interfacial energy equal to 0.107 $J \cdot m^{-2}$. Γ is dislocation line tension, approximated as $1/2Gb^2$, and f_V is the precipitate volume fraction.

1.1.4. Al-Zr-Sc system

Zirconium and Scandium are minor alloying elements that can be added to alloys, such as those of the AA7XXX type. They serve several purposes: improving stress corrosion resistance, increasing hardness, and as grain refiners [2]. The Al-rich corner of the Al-Zr system is peritectic, with the reactant being the Al_3Zr phase. The peritectic horizontal lies at 660 °C and corresponds to a maximum solubility of 0.28 wt. %. The solubility decreases rapidly and reaches only 0.05 wt. % at 500 °C (Figure 1.4) [2].

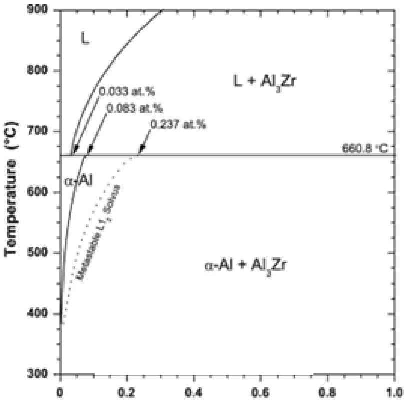

Figure 1.4 The equilibrium Al-Zr phase diagram [36].

Low solubility, combined with the low diffusivity of Zr in Al, makes Al_3Zr a very stable precipitate resistant to coarsening and redissolution, making it desirable when present in the form of nanometer-sized dispersoids [36]. However, they could not be dissolved when present in the form of extensive micrometer-sized constituents, which can form at low cooling rates directly during casting as it is the first solid to form in the peritectic condition. Al_3Zr has two possible structures. Al_3Zr precipitates from the SSSS and the melt in a cubic phase with an $L1_2$ structure. However, this is only a metastable Al_3Zr phase. The stable phase has a tetragonal $D0_{23}$ structure, formed by the transformation at high temperatures between 400 °C and 500 °C, with long holding times lasting over 100 h. The transformation occurs by the dissolution of smaller $L1_2$ precipitates. The surplus Zr then re-precipitates heterogeneously at dislocations and (sub)grain boundaries. Alternatively, a part of the precipitates can coarsen and transform into a stable structure directly [36-41]. A low solubility and a relatively low diffusivity of Zr suppress precipitation near grain boundaries [36,41]. A modified homogenization can reduce this effect. One-step annealing is generally performed at temperatures above 450 °C. However, Jia et al. [37,42] reported increased strength and recrystallization resistance after two-step homogenization annealing at 350 °C or 250 °C for 48 h and then 450 °C for 60 h. These procedures produce a higher number density of Al_3Zr [42]. Jia et al. also infer a relationship between θ precipitation and Al_3Zr precipitation kinetics [37]. They explain the existence of oriented Al_3Zr precipitate clusters through Zr diffusion and precipitation on the θ phase sites. Al_3Zr precipitation is also supported by other elements, such as Fe and Si, through precipitation on solute clusters, though these elements are detrimental impurities [43].

Grain refinement and increased corrosion resistance are commonly mentioned as positive results of Zr addition. Increased corrosion resistance is a byproduct of grain refinement, as a finer recrystallized grain structure is generally more corrosion resistant [44]. The primary grain refinement occurs during casting, where Zr-precipitates formed from the melt serve as nucleation centers [36]. During recrystallization, the nanometer-sized precipitates retard grain and subgrain boundary motion through an increased Zener drag [34,36,45].

Another role of Al_3Zr is the influence on the T_1 precipitation through the interfacial precipitation on the Al_3Zr/α interface. This influence was initially observed for both T_1 and θ phases, which were found to precipitate either on the interfacial dislocations or the Al_3Zr particle directly [46]. Analysis of interfacial energies indicates that the size of the "first terrace" of the new precipitate is directly proportional to the spherical particle radius. Small particle size could place this terrace size below the size of a critical nucleus, making interfacial precipitation less likely to occur [46]. Adding Sc could further benefit this effect since the Sc-containing precipitates are larger while providing a more robust Zener drag.

Like Zr, Sc forms a trialuminide Al_3Sc with the $L1_2$ structure in low alloyed Al alloys. No other forms of Al_3Sc were observed [47]. Early works suggested that the Al-rich corner of the Al-Sc phase diagram is peritectic with the peritectic horizontal at 665 °C [48,49]. However, later studies have shown that it is eutectic, with a eutectic temperature reported between 655 °C and 660 °C, which is just below the solidification temperature of pure Al at 660.452 °C. The eutectic composition is 0.6 wt. % Sc and the solid solubility of Sc in Al at the eutectic temperature is approximately 0.35 wt. % Sc [48,50,51]. Sc causes disproportionately higher strengthening and grain refinement than other elements, even at low concentrations.

There is a significant solubility of Zr in the Al_3Sc phase of (~ 35 wt. %) and lower solubility of Sc in the Al_3Zr phase of (~ 5 wt. %). The diffusion of either element into the opposite phase yields a decrease in the lattice parameter [48]. The Al_3Sc can form in several ways, including detrimental formation during solidification. The precipitation from the SSSS is preferred. It can occur continuously or discontinuously [48]. The continuous precipitation of Al_3Sc can be described in standard nucleation-growth-coarsening stages with mostly homogeneous nucleation, leading to spherical precipitates. These precipitates are coherent to a certain size, which depends on the precipitation temperature. No metastable precipitation stages were reported for this phase. Rare heterogeneous nucleation on grain boundaries and dislocations has also been reported. Models of heterogeneous precipitation predict that it is preferred at high transformation temperatures and low Sc concentrations [48,52].

Precipitation kinetics of Zr and Sc-containing phases are affected by other elements, including each other. Due to the high Zr concentration in Al_3Sc, it makes sense to talk about an $Al_3Sc_{1-x}Zr_x$ phase instead. Initial precipitation stages of Al_3Sc are largely unaffected by the addition of Zr. However, adding Zr slows down the later stages of particle transformation, and $Al_3Sc_{1-x}Zr_x$ is more resistant to coarsening than pure Al_3Sc particles [48,50,51,53]. There is a higher tendency towards the diffusion of Zr into the phase at higher temperatures due to the low diffusivity of Zr in Al. At 300 °C, the content of Zr in the ternary phase is reported to be less than one wt. %. Regardless, enough Zr diffuses to form an outer Zr layer, preventing coarsening even at aging temperatures as low as 350 °C [54,55].

Clouet et al. [56] combined HRTEM imaging, high-angle annular dark field (HAADF) imaging, HR X-ray analysis, 3DAP measurements, and ab initio calculations when studying precipitation in Al-Sc-Zr-based materials. Monte Carlo-enhanced simulations of annealing of a supersaturated Al matrix show an Sc-rich core with Zr concentration, which initially decreases with distance from the center of the core but significantly increases at the very edge of the precipitate, forming a Zr-rich shell. 3D atom probe (3DAP) experiments then proved that the precipitated particles are not homogeneous but formed by a pure Al_3Sc core and an $Al_3Sc_{1-x}Zr_x$ outer shell.

1.1.5. Al-Cu-Mg system

Phases of the ternary Al-Cu-Mg system are called S-phases. Like the binary Al-Cu phases, they precipitate in a specific sequence.

A good representation of an Al-Cu-Mg precipitation sequence, as described by Wang and Starink [17], is:

$$\text{SSSS} \rightarrow \text{co-clusters} \rightarrow \text{GPB2/S}'' \rightarrow \text{S}.$$

Co-clusters are predominantly Cu-Mg clusters, also termed GPB1 (Guinier-Preston-Bagaryatsky) zones. GPB2 is an orthorhombic coherent phase with an approximate composition of $Al_{10}Cu_3Mg_3$. S is the equilibrium phase with Al_2CuMg composition. S'' and the S phase can coexist with the semi-coherent S' phase. The composition of the S´ phase is nominally the same as the equilibrium S phase. This phase was first reported by Bagaryatsky [57] in his interpretation of the precipitation sequence

$$\text{SSSS} \rightarrow \text{GPB zone} \rightarrow \text{S}'' \rightarrow \text{S}' \rightarrow \text{S}$$

Silcock first used the term GPB zone in his publication [58], suggesting that their structure differed from the previously discovered GP zones. While both precipitation sequences are often cited, their exact structure is a point of contention [17].

Several models were proposed for the structure of the S phase based on XRD patterns [59], HRTEM observations [60], and first-principle calculations [61]. However, the original Perlitz and Westgren (PW) model [59] is correct. According to this model, the S phase has the *Cmcm* orthorhombic structure. In precipitation heat treatments, the S phase forms lathes on {210} planes of the Al matrix elongated along the <100> direction [17]. The orientation relationship between the S phase and the Al matrix is [17,57]:

$$[100]_{Al}//[100]_{S},\ [02\bar{1}]_{Al}//[010]_{S},\ [012]_{Al}//[001]_{S}.$$

These orientation relationships can produce 12 equivalent variants.

Bagaryatsky, in his original work [57], has reported the S' phase to only differ slightly in lattice parameters from the equilibrium S phase. Both phases can only be distinguished from the misfit [17]. Therefore, many modern publications do not differentiate between the phases, use S' and S interchangeably, or refer to S' as semi-coherent S instead. The precursor to the S phase – the GPB2 zone – has a structure closely connected to one of the S phases. The exact structure and orientation relationships of the S'' phase have been the subject of many changes since the original publication of Bagaryatsky [57]. Current studies indicate that the phase has an orthorhombic structure with $Al_{10}Cu_3Mg_3$ composition when precipitated in Cu-rich alloys [62]. This composition lies between the stable Al_2CuMg composition and Cu-Mg clusters containing approximately 90 at. % Al [17,63]. The orientation relationship between this phase and the Al matrix satisfies the following:

$$[100]_{GPB2}//[100]_{Al},\ [010]_{GPB2}//[010]_{Al},\ [001]_{GPB2}//[001]_{Al}.$$

Studies of quenched and aged alloys and DSC analyses suggest that the S phase and GPB2 zones coexist during aging, with the S phase consuming GPB2 zones at longer aging times [17,64]. An aging experiment at 150 °C shows dense S precipitation and peak intensity of GPB2 reflections in SAD TEM after 48 h. The coexistence of clusters, GPB zones, and S-phase precipitates is presumed during these early stages of aging [17,63]. After 72 h, more S precipitates form, and the GPB2 reflections weaken. The aging response is dominated by S-phase precipitation during aging at 190 °C, which is the stable equilibrium phase up to about 450 °C, where it fully dissolves [63].

1.1.6. Other alloying elements and constituent phases

Ag is also a common alloying element present in these types of alloys. Ag serves a similar role as Mg in aiding the precipitation of the T_1 phase. While Mg can aid in strengthening the precipitation in binary Al-Cu alloys by aiding the precipitation of the θ' phase and the ternary S phases [65], Ag only works in tandem with Mg in these alloys and does not affect binary Al-Cu alloys [66]. Mg and Ag have clear roles in Al-Cu-Li-Mg-Ag alloys. Mg promotes T_1 precipitation, decreases activation energy for θ' growth, and reduces coarsening rates of the strengthening plates. Ag retards GP zone formation, stimulates T_1 precipitation, and enhances the coarsening rate of strengthening plates [66]. The addition of both, therefore, promotes T_1 nucleation, but their effects on coarsening rates are competing. It was concluded that Ag substitutes Cu in the matrix near particle/matrix interfaces to accommodate the lattice strain [66].

Aside from the effect of Ag as a solute, these alloys have also reported a quaternary Ω phase. This phase precipitates as a hexagonal-shaped platelet on the {111} matrix planes and has been reported to be monoclinic, hexagonal, orthorhombic, and tetragonal [17]. Garg and Howe suggested that the Ω is, in fact, a distorted form of the θ phase, with the most significant atomic displacement between the two structures being lower than 1 % [67].

Fe is present in these alloys as an impurity. Due to its low solubility, it does not form strengthening precipitates even at high temperatures [2]. Instead, it forms coarse constituent phases directly during casting. Coarse constituent particles are detrimental to mechanical properties such as fatigue crack growth with microcracks forming around these particles, forming a bridge for a nucleated macrocrack to spread rapidly. Fe-based constituent particles, such as Al_7Cu_2Fe, are preserved after high-temperature heat treatment, unlike constituent particles of other systems, which dissolve due to a much higher solubility of the particle-forming elements [68]. The Al_7Cu_2Fe phase additionally harms corrosion properties as corrosion propagates preferentially along boundaries connected to clusters of these particles. These particles can also contain a small amount of solute Li, further increasing their electrochemical activity and making them preferable locations for the nucleation of corrosion [69].

The quaternary Al-Cu-Mg-Li system contains a high number of complex constituent phases. These can form either through a liquid-solid interaction during casting, such as the T_2, C, and R phases, or solid-solid interaction during homogenization and high-temperature aging [70,71]. These phases have similar compositions and can potentially transform into one another [72]. Most of these phases get dissolved during high-temperature annealing, i.e., the T_2 phase is stable up to 420 °C. On the other hand, the R phase can be stable up to 560 °C, though it primarily forms in alloys with lower Cu/Mg ratios [17].

Table 1.1 lists all the previously discussed phases, their structures, designations, and lattice parameters.

Table 1.1 List of phases found in the Al-Cu-Li-Mg-Ag-Zr-Sc system [2,5,6,15,36].

Phase	Designation	Structure	a [nm]	b [nm]	c [nm]	α [°]	β [°]	γ [°]
Al_3Li	δ'	$L1_2$	0.401	0.401	0.401	90	90	90
AlLi	δ	FCC	0.637	0.637	0.637	90	90	90
Al_3Cu	GP2/ θ''	-	-	-	-	-	-	-
Al_2Cu	θ'	Tetragonal	0.404	0.404	0.580	90	90	90
Al_2Cu	θ	Tetragonal	0.607	0.607	0.487	90	90	90
Al_3Zr	β'	$L1_2$	0.408	0.408	0.408	90	90	90
Al_3Zr	β	$D0_{23}$	0.400	0.400	1.729	90	90	90
Al_3Sc	-	$L1_2$	0.410	0.410	0.410	90	90	90
Al_2CuLi	T_1	Hexagonal	0.495	0.495	0.933	120	90	90
$Al_{7.5}CuLi_4$	T_B	Cubic	0.583	0.583	0.583	90	90	90
Al_2CuMg	S	Orthorhombic	0.400	0.923	0.714	90	90	90
Al_7Cu_2Fe	-	Tetragonal	0.634	0.634	1.487	90	90	90
Al_5CuLi_3	R	Cubic	1.390	1.390	1.390	90	90	90

1.2. Casting methods

Different casting methods substantially affect the microstructure and mechanical properties of the as-cast material and the subsequent processing steps required to reach the desired mechanical properties. This influence is due to a difference in applied cooling rates and forces during the casting.

1.2.1. Direct-chill casting

Direct chill (DC) casting is a semi-continuous casting method. It is commonly used to cast large-scale ingots. These ingots are widely susceptible to macrosegregation – a presence of non-uniform chemical and phase composition over the length scale of the casting [73,74]. The concentration of alloying elements across the cross-section of the cast ingot can be out of the registered ranges for the specific alloy [73,74]. Unlike microsegregation, which occurs on a scale of individual dendrite spacings or solidified cells (10 to 100 μm), the inhomogeneities of macrosegregation occur on a scale of one centimeter to one meter. While homogenization annealing can fix microsegregation, it cannot fix macrosegregation [73,74]. However, macrosegregation can be avoided through a proper casting setup. This setup includes limiting the scale and shape of the cast product and a limitation to certain alloying elements.

Continuous or semi-continuous DC casting is among the most efficient for sheet and forged products. Common DC cast materials are billets with a round cross-section or rectangular ingots. The area of these sections is generally in the order of one squared meter [73]. Liquid metal is poured into a water-cooled mold, the bottom of which is initially closed by a starting block. This block is lowered at a constant rate once the liquid metal solidifies and forms a solid shell. The outer shell solidifies through convection into the water-cooled mold (primary cooling), while the inside remains semi-solid. The outer shell of the ingot is then cooled directly by water jets as it descends into a pit below the mold (secondary cooling) [73] (Figure 1.5). The average cooling rate of the process ranges from 0.5 $K \cdot s^{-1}$ to 10 $K \cdot s^{-1}$ for ordinary commercial DC casters [73].

Macrosegregation of multi-component alloys is a complex topic to tackle due to the inherently non-equilibrium nature of the casting process and the complicated modeling of the flow of individual components in the semi-solid state. However, modern computational methods with proper models can give at least semi-quantitative agreement with the experimental results [75]. The effect itself is caused by solute transport in the semi-solid part of the billet. This transport is controlled by buoyancy forces resulting from different thermal, concentration, density gradients, and bulk convection [74]. The most common concentration distribution of solutes in DC cast billets is radial, with a depleted zone in the center surrounded by an outwardly spreading enriched zone and another thin, depleted zone just below the surface. The surface itself is significantly enriched [74]. Solute distribution in rectangular ingots is not radial but is qualitatively similar. Thermosolutal flow tends to increase macrosegregation. Higher casting speeds and casting temperatures exacerbate this flow, increasing liquid pool depth and the thermal driving forces across the pool [74].

The resulting microstructures generally contain coarse grains (100 μm to 1 mm [73,76]). Primary phase precipitates of hypoeutectic alloys are situated along the boundaries of eutectic cells and are several (> three) micrometers wide [77-79].

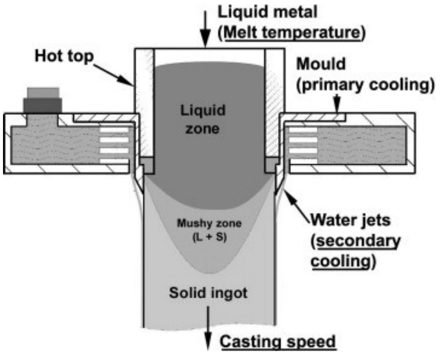

Figure 1.5: Casting setup of the DC casting method [73].

1.2.2. Twin-roll casting

Twin-roll casting (TRC) is a continuous casting method that produces strips of alloys several millimeters thick. During twin-roll casting, the molten material is poured onto a pair of water-cooled rolls, where it solidifies and is then rolled for a short period (Figure 1.6).

The scale of individual solidified cells and spacing between dendrite arms is smaller due to the faster cooling rates (~ 1000 $K \cdot s^{-1}$) employed in this method than in traditional ingot casting methods [80]. Similarly, TRC materials contain finer intermetallic particles by an order of magnitude than DC-cast counterparts [80]. TRC has been successfully applied to producing Al alloys. Still, it is mainly limited to alloys with a low freezing (solidification) range (< 30 K), such as low alloyed packaging foil stock Al-Fe-Si-based materials [81,82]. Where possible, TRC reduces the cost and energy requirements of the production of sheet products but has notable drawbacks, mainly positive centreline segregation of solutes. Segregation can be severe for specific elements and has historically limited the use of TRC in high-alloyed and hypereutectic systems [81,83].

Strip thicknesses lower than three millimeters are possible with higher casting speeds. Higher casting speeds require the caster to withstand the higher torques and roll separation forces [81]. The heat of the molten material is extracted through the surface of the strip and then into the water-cooled rolls. This extraction occurs over the total contact length in the casting and rolling zones. The nucleation of solid grains commences at the solidified surface of the strip and continues with dendritic growth towards the center.

Molten metal commonly enters the roll gap at a temperature close to the melting point and leaves the roll gap at temperatures around 250 °C [84]. Elevated strip temperatures imply the occurrence of hot-rolling and possible dynamic recrystallization. The flow stress of the solidified strip is lower than the contact pressure of the rolls, causing plastic deformation of the as-cast strip, which improves contact between the strip and the rolls [81,85]. The degree of deformation also depends on the size of the rolls, with higher deformation applied to strips produced by rolls with a smaller diameter.

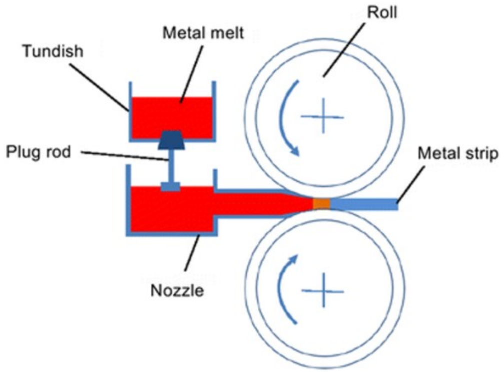

Figure 1.6 Schematic representation of a horizontal twin-roll caster.

Unlike DC casting, where the continuous casting nature lies in a simple moving mold, the as-cast structure of TRC strips arises from a combination of solidification and rolling. The grain structure of as-cast TRC strips is equiaxed or columnar [81].

The microstructure of as-cast TRC strips is generally gradient. Secondary dendrite arm spacing (SDAS) is finer along the surface and grows towards the center since it is connected to the local cooling rate, which decreases with increasing distance from the surface/roll interface. A relationship between SDAS and the parameters of solidification can be written as

$$SDAS = A \cdot (G_T \cdot R_D)^{-n}\,, \tag{1.4}$$

where A and n are material-dependent constants, and G_T is the thermal gradient at the solid/liquid interface. R_D is the velocity of the dendrite tip. The exact thermal gradient and velocity of the dendrite tip are difficult to establish, as is the exact order of observed dendrites. Therefore, a simplified equation is proposed:

$$DAS = A \cdot V^{-n}\,, \tag{1.5}$$

where V is the local solidification rate, and DAS is any observed dendrite arm spacing [86-88]. This relationship is applicable for materials solidified with cooling rates between $10^0 - 10^6$ K·s^{-1} as it requires dendritic growth of materials.

Higher casting speeds result in higher heat retention and the possibility of dynamic recrystallization [81]. Dynamically recrystallized strips are characterized by a more equiaxed grain structure in the as-cast state [89]. Grain structure can be further affected by the addition of a grain refiner. Grain refiners were found to reduce the formation of macrosegregation during casting [90,91]. While the grain refinement was mainly limited to adding Ti-C or Ti-B-based master alloys, these additions led to the formation of relatively coarse particles that serve as nucleation centers for the heterogeneous nucleation of grains. Sc is also a potent grain refiner, as discussed in previous sections, but does not lead to the formation of coarse intermetallics.

1.2.3. Rapid solidification methods and melt spinning

Rapid solidification (RS) methods are methods during which the material solidifies at rates higher than 10^4 K·s^{-1}. Such high cooling rates significantly improve the grain refinement and chemical homogeneity of the material. However, they cannot be achieved through means. Standard rapid solidification casting methods include the dispersion of the molten material into tiny droplets (atomization) or casting small amounts of the molten alloy onto a sufficiently cooled substrate (melt-spinning).

Melt-spinning may produce ribbons of amorphous or glassy alloys. The cooling rate can reach up to 10^8 K·s. The high cooling rate can prevent typical nucleation and grain growth [92]. The alloy is melted and then ejected under pressure onto a rapidly rotating water-cooled wheel (> 5000 rpm) through a thin nozzle (Figure 1.7). The cooling wheel must be made from a good heat conductor (e.g., Cu) to ensure rapid solidification. The material should be rapidly spread into a thin layer. This condition is satisfied through the injection of tiny droplets under a suitable angle and the high rotation rates of the wheel. The original experiment devised by Duwez et al. [92] tested this method with four Ag-Cu alloys of various compositions. Despite Ag-Cu being a simple eutectic system, the X-ray diffraction pattern of the produced ribbons showed the presence of only a single phase with various lattice parameters as the Cu-rich and Ag-rich phases did not have time to nucleate and grow properly, and a single metastable solid solution formed instead. A plot of lattice parameter vs. concentration showed a smooth curve connecting previously established lattice parameters for the α and β phases at the solubility limit with only a 1 % variation from Vegard's law of linearity at 50 at. % Cu [93].

Higher cooling rates are associated with higher velocity of the solidification front. They are reached by high undercooling due to high thermal transfer coefficients between the water-cooled roll and the molten alloy. Thermal transfer coefficients associated with RS methods (10^7 W·K^{-1}·m^{-2} [94]) are several orders of magnitude higher than in TRC (10^4 W·K^{-1}·m^{-2}) or ingot castings (10^2 W·K^{-1}·m^{-2}) [95]. A sufficiently high velocity of the solidification front gives rise to the so-called "diffusionless" solidification, which traps all solutes that cannot diffuse to the solidification front in time. Material solidified by pure diffusionless solidification is featureless, and any potential phases are formed during the subsequent decomposition of the supersaturated material. Thermal transfer through the newly solidified featureless region is less efficient than the transfer directly into the water-cooled roll, and the velocity of the solidification front decreases. The cellular crystallization occurs at solidification front velocities comparable to the critical velocity. The solidification front is no longer planar at this stage. The increased surface of the solidification front helps to trap impurities. Regular primary phases at grain boundaries can form during cellular crystallization. Additionally, further phases can form during the decomposition of the supersaturated matrix, similar to pure diffusionless solidification [94,96]. The thermal transfer coefficient decreases with the increasing thickness of the material, eventually causing a transition into regular dendritic growth.

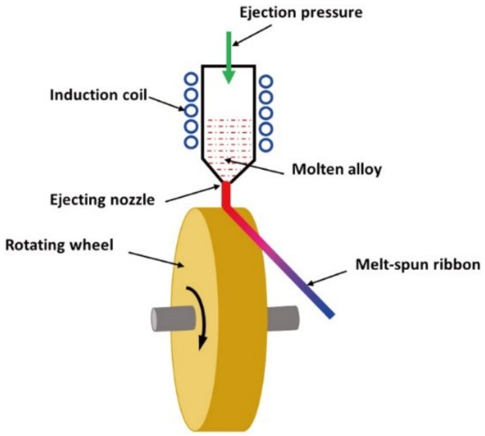

Figure 1.7: Schematic production of thin, rapidly solidified ribbons by melt spinning [97].

The final structures of RS materials depend substantially on the local solidification conditions, which may differ throughout the strip. The cooling rate for the melt-spun alloy can also be calculated using the general one-dimensional diffusion equation:

$$\frac{\partial T}{\partial t} = \alpha \frac{\partial^2 T}{\partial x^2} = \frac{k}{C\rho}\frac{\partial^2 T}{\partial x^2}\ , \tag{1.6}$$

where t and x are time and distance from the surface/roll interface, α is thermal diffusivity, k is thermal conductivity, C is specific heat capacity, and ρ is the density of the alloy. The solution to this equation can be written in the form of

$$T(x,t) = K_1 + K_2\,\mathrm{erf}\left(\frac{x}{2\sqrt{\alpha t}}\right), \tag{1.7}$$

where K_1 and K_2 are constants based on boundary conditions [98].

Solving this problem further, applying boundary conditions of the ribbon and the Cu wheel and assuming a constant cooling rate, which is justified by the very short cooling time expected for the melt-spun strips, leads to an equation for solidification time:

$$t = \frac{\delta_1^2 \pi (C_1 \rho_1)^2}{k_2 C_2 \rho_2}, \tag{1.8}$$

where indexed variables with 1 and 2 are constants for the ribbon and Cu wheel, respectively. δ_1 is the ribbon thickness. The density and heat capacity of the alloy is 2300 kg·m^{-3} and 1230 J·kg^{-1}·K^{-1}, respectively [95]. The density and heat capacity of the copper wheel is 8900 kg·m^{-3} and 384 J·kg^{-1}·K^{-1}, respectively. The thermal conductivity of the copper wheel is 400 W·m^{-1}·K^{-1} [98]. The thickness of the studied strips can vary, but areas that include the dendritic growth zone range from 30 μm to 60 μm in thickness. This results in a solidification time between 16 μs and 66 μs.

An equation for an approximate cooling rate at a certain distance x from the copper wheel can also be defined. While complex looking, it is essentially a function of ($1/\delta^2$) of the ribbon thickness.

$$V(x) = \frac{-\alpha_1 \exp\left(-\frac{C_2 k_2 \rho_2}{4\pi C_1 k_1 \rho_1}\right)\left(-T_{10} + \frac{k_1\sqrt{\alpha_2}T_{10} + k_2\sqrt{\alpha_1}T_{20}}{k_1\sqrt{\alpha_2} + k_2\sqrt{\alpha_1}}\right)}{2x^2\pi^2\left(\frac{C_1 k_1 \rho_1}{C_2 k_2 \rho_2}\right)^{\frac{3}{2}}}, \tag{1.9}$$

where T_{i0} is the initial temperature of the melt and roll, which is 1273 K and 300 K, respectively, and thermal diffusivities are 3.6·10^{-5} m^2·s^{-1} and 1.2·10^{-4} m^2·s^{-1} for the alloy and roll, respectively [98]. The thermal conductivity of the alloy is 88 W·m^{-1}·K^{-1} [95].

1.4. Al-Cu-Li-Mg-Sc-Zr based alloys

1.4.1. Al-Li-based alloys

The current generation of Li-containing Al alloys generally contains Cu as a major alloying element, and the Cu/Li ratio (in wt. %) is close to 2 to promote the strengthening of the material through the formation of the T_1 and θ' phases and suppress the formation of the δ' phase. Fe and Si are commonly present as impurities in these alloys and are considered detrimental. Dispersoid-forming elements (Zr, Sc) are added as grain refiners. Ag and Mg are added as T_1 phase precipitation promoters.

Melting and casting of Al-Li alloys provide a technological challenge due to the high reactivity of Li and its low density. Li also forms a lightweight hydride in the presence of H, which floats on the melt. The casting of Al-Li alloys requires meager impurity contents and controlled atmospheres with cover gases such as Ar or He [99]. Thermomechanical processing of standard DC cast AA2195 alloys is well defined (see schematic in Figure 1.8). They are traditionally cast as ingots, homogenized at high temperatures, and hot-formed by extrusion, rolling, or forging into sheets (rolled products below 3 mm thickness), plates (rolled products above 3 mm thickness), or extruded products. Hot forming always affects dynamic precipitation in the material. Therefore, a solution treatment step is always required since standard hot forming produces an over-aged material with incoherent, coarse precipitates. Cold working performed by stretching or rolling follows immediately after quenching from the solution treatment temperature, enhancing the subsequent age hardening.

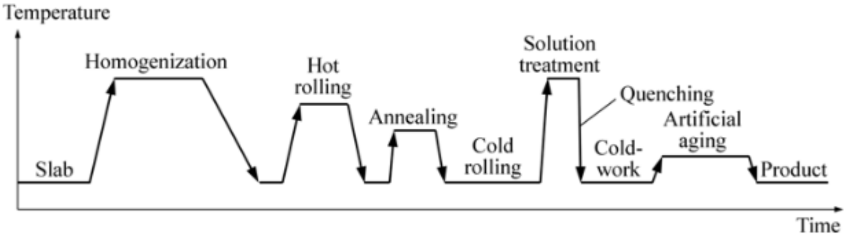

Figure 1.8 Standard processing scheme of DC cast AA2195 alloys [100].

Homogenization is performed to accelerate the diffusion of solutes, allow their redistribution, and effectively eliminate microsegregation. Homogenization at high enough temperatures also dissolves certain constituent phases, further enriching the solid solution. The formation of Al_3Zr ($Al_3(Sc,Zr)$ in Sc-containing alloys) particles is crucial for the recrystallization control, and its precipitation must be considered when designing the homogenization treatment. Numerous studies on these alloy types have concluded that a single-step homogenization at 510 °C/16 h is sufficient for Al-Cu-Li-Mg-Zr-based alloys [101-103]. However, Yang et al. [104] developed a two-stage homogenization treatment with two holding temperatures at 460 °C and 510 °C, which improved Al_3Zr precipitation by increasing its number density and refining its size.

Hot rolling of these materials is performed at temperatures around 300 °C [79], resulting in over-aging because the hot working temperatures are much higher than temperatures of standard artificial aging (below 200 °C) [99]. Necessary solution treatment is generally done at very high temperatures. The reported solution treatment temperatures and durations may vary. Solution treatment is reported at temperatures between 500 °C and 530 °C. Similarly, the solution treatment intervals generally range between 30 and 60 min [79,100,105,106]. Incomplete solution treatment decreases the yield strength after aging because of lower T_1 precipitation due to a lack of solute Cu [107]. Stable grain refining dispersoids formed during homogenization are essential to prevent the coarsening of grains during this solution treatment.

Cold working is an essential operation in Al-Li alloys immediately after the solution treatment [99]. It eliminates distortions and generates a dense dislocation network in the Al matrix. A study by Gable et al. [8] shows that the YS of an alloy in which T_1 is the primary strengthening precipitate can increase by about 50 % when aged after an 8 % pre-stretch. Even at a 4 % stretch, the homogeneity of the main strengthening T_1 phase improves at the expense of the less beneficial θ' phase [8]. Cassada et al. [31] showed that the same volume fraction of the T_1 phase precipitates in a pre-stretched material after six hours as in the material aged for 24 h without pre-stretching, with their number density being two orders of magnitude higher [8,108,109].

Higher temperatures (140 °C – 180 °C) of artificial aging are generally more desirable as they lead to shorter aging times [31,79]. Al-Li alloys typically have longer aging times (8 h – 20 h) than other non-Li-containing alloys of the 2xxx and 7xxx series [2,5,31]. Multi-step aging treatments can be tailored for specific purposes, leading to significant increases in certain properties, such as ductility, by limiting excessive grain boundary precipitation [110]. Overaging is considered detrimental in all heat-treatable alloys. In Al-Cu-Li alloys, overaging increases T_1 phase thickness [79].

1.4.2. Sc in Al-Li alloys

Previous studies of Al-Sc alloys focused mainly on grain refinement, recrystallization resistance, and mechanical properties. Mechanical properties – namely hardness and tensile properties are improved by Al_3Sc precipitates [111]. The earliest studies focused mainly on binary Al-Sc and ternary Al-Sc-Mg systems. Sc provides the highest strength and grain refinement to alloys out of all the alloying elements on an atom-by-atom basis. It offers ten times higher strengthening than Cu [112]. However, higher additions are expensive and are generally kept below ~ 0.2 wt. % in special high-strength alloys. Particles of the binary Al_3Sc phase are coherent up to 22 nm at RT and prevent recrystallization up to solidus by imposing strong Zener drag on grain boundaries [113].

Al_3Sc precipitates form by the decomposition of SSSS. Their morphology depends mainly on Sc concentration and aging conditions. Fine, coherent, and homogeneously distributed particles form at temperatures above 200 °C and below 400 °C. These particles are stable and resistant to coarsening at temperatures around 300 °C and remain 4-10 nm-sized even for long aging times [113]. Annealing above 400 °C leads to their rapid coarsening and a loss of coherency. At higher annealing temperatures and lower supersaturation, heterogeneous nucleation at dislocations and other defects occurs.

The highest reported equilibrium solubility of Sc in Al is 0.4 wt. %. However, with rapid solidifications, a supersaturated solution of Sc may form with concentrations up to 0.6 wt. %. This solid solution is less stable than the SSSS of other transition metals, namely Zr. The incubation period of decomposition is three to four orders of magnitude shorter owing to its higher diffusivity [114]. Coagulation occurs at higher concentrations, making the desirable range of Sc addition 0.1 - 0.5 wt. %.

Due to its low stability, a common practice is Sc addition in tandem with Zr. Whereas 0.5 wt. % addition was needed in alloys with pure Sc addition, only 0.2 wt. % was required in alloys with both Sc and Zr content to reach comparable results in terms of grain refinement [114]. A 1:1 ratio of Zr to Sc (in wt. %) is optimal. However, the total content of Zr and Sc each is recommended to be between 0.07 - 0.12 % wt. % to maximize strengthening and refining effects while preventing the formation of coarse binary AlZr intermetallics [115]. Predeformation before Al_3Sc precipitation stabilizes the subgrain structure of the material through heterogeneous precipitation of the dispersoid and subsequent pinning of the subgrain boundaries [114,116].

The strengthening contribution of Sc in Al alloys can come from solid solution and precipitate strengthening, though the latter is preferential since it also increases the Zener drag. Al_3Sc particles can pin dislocation cells. Additionally, Sc provides thermal stability of the matrix by increasing recrystallization temperature.

Sc does not form any binary compounds with other common strengthening elements, such as Mg or Li, and any solubility of these elements in the Al_3Sc phase is minimal. Sc can form a ternary W($Al_{8-x}Cu_{4+x}Sc$ for x between 0 and 2.15) phase with Cu. Cu content should be kept below 3 wt. % to prevent the formation of the coarse W phase entirely since it siphons both Cu and Sc from the matrix and causes deterioration of mechanical properties [112,117]. The W phase forms primarily on eutectic θ/α-Al interfaces during the solidification. While the eutectic θ can be dissolved during homogenization, the W phase cannot and remains firmly placed on eutectic boundaries [118]. However, higher solidification rates (above 10 K·s^{-1}) prevent the formation of the W phase in alloys containing as much as 6 wt. % Cu, as stated by De Pottey et al. [118]. They also reveal a potential precipitation of a nanoscale W phase during high-temperature heat treatment. The equilibrium phase diagram suggests heat treatment temperatures for Al_3Sc precipitation below 261 °C in alloys with high Cu content (Figure 1.9) [54]. Zr addition can also prevent W-phase formation during heat treatment as the Zr-rich shell of the $Al_3(Sc,Zr)$ phase traps Sc and prevents its long-range diffusion.

Fe cannot form ternary compounds with Al and Sc when present as an impurity. The Al-rich corner of this ternary system is limited to the coexistence of α-Al, $Al_{13}Fe_4$, and Al_3Sc [48].

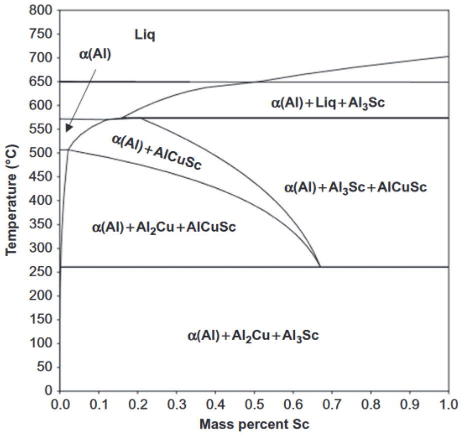

Figure 1.9 Section of the Al-Sc-Cu ternary phase diagram. Cu content is fixed at 4 wt. %. W phase is denoted as AlCuSc [54].

Sc is not reported to form any quaternary or higher-order phases with any combination of the previously mentioned alloying elements.

The concentration of Sc in the solid solution depends on the cooling rate. At 10^2 K·$s^{-1,}$ the metastable solubility is 0.6 wt. % [119]. TRC easily achieves these cooling rates, exceeding 10^3 K·s^{-1}. The combined solubility of Zr and Sc depends on the crystallization rate. However, the ternary system is more undercooled at the same crystallization conditions, increasing crystallization rate and solubility. This undercooling effect is the highest if the wt. % ratio of Zr:Sc addition is approximately 1:1. The Al-Sc-Zr solid solution may decompose during the cooling of the ingot (depending on the cooling rate) or during further thermomechanical treatment, including high-temperature homogenization. Therefore, the temperatures for these treatments should facilitate the controlled decomposition of the Al-Sc-Zr solid solution. Also, the holding times should be short to prevent the coarsening of existing or newly formed Al-Sc-Zr particles.

Other common alloying elements in heat-treatable Al alloys can influence the precipitation of Sc-containing particles. In turn, the presence of Al_3Sc particles and solute Sc can influence the precipitation of strengthening particles in these systems. Solute Mg slightly increases the α-Al lattice parameter and, as a result, the critical diameter of coherency for the Al_3Sc phase [48]. 3D microprobe investigation shows microsegregation of Mg at the Al/Al_3Sc interface [120]. Cu suppresses the tendency towards discontinuous precipitation. Conversely, Al_3Sc can precipitate on coarsened binary θ' phases at temperatures around 350 °C due to prior segregation of Sc at the θ'/α-Al interface in systems with low cooling rates. The Sc content in these enriched regions is up to 10 times higher than in the surrounding matrix, and the region is approximately 2 nm wide [121].

Li is reported not to affect Sc phase precipitation. Standard heat-treatable alloying systems (Al-Cu, Al-Li, Al-Cu-Li) are generally aged at temperatures up to 200 °C, which have little to no effect on the Sc-containing phases. The presence of the Al_3Sc phase can improve the precipitation kinetics, refinement, and the homogeneity of distribution of certain phases by heterogeneous precipitation on the Al_3Sc phase. This effect is most prevalent in Al-Li and Al-Cu-Mg alloys with a refinement of δ' and S' particles, respectively [48,122]. Increased precipitation kinetics were also observed for the θ' phase in both Sc and Sc+Zr containing alloys [54]. Suresh et al. [79] observed increased precipitation kinetics with Sc addition in an Al-Cu-Li-Mg-Zr-based alloy. Jiang et al. [123] studied an Sc addition of 0.1 wt. % into an Al-Cu-Li-Zn-Mg-Ag-based alloy. They observed an increase in length and decrease in the number density of the T_1-phase particles in the Sc-added alloy after aging at 175 °C but inverse behavior after aging at 200 °C. They explain this phenomenon through a model of "vacancy prisons." They assume that Sc atoms surround vacancies, lowering the diffusion rate for Cu and Li, thus limiting the formation of solute clusters during early aging stages. Zhang et al. [124] studied an Al-Li-Cu-Zn-Mg-based alloy with the addition of 0.2 wt. % Sc. They noted a positive effect of Sc on S' nucleation. Finally, grain refinement can improve precipitation kinetics, which leads to higher grain boundary diffusion and lower nucleation energy [125].

Al_3Sc is coherent but has a high lattice mismatch with the surrounding matrix, which retards the dislocation and grain boundary motion [126]. Al_3Sc can also form directly in the melt and serve as nucleation centers for matrix grains, which induces grain refinement of the as-cast material. Combining with Zr further increases the grain refining effect. Yin et al. [127] showed that adding 0.1 + 0.2 wt. % Zr+Sc provides stronger grain refinement than either 0.6 wt. % Sc or 0.2 wt. % Zr in Al-Mg alloys. The same effect was observed in Al-Cu-Li alloys by Novikov and Grushko [128].

The effect of Sc on recrystallization resistance was first noted in Al-Zn, Al-Mg, and Al-Zn-Mg alloys where the addition of 0.3 wt. % Sc increased the recrystallization onset temperature by over 200 °C [48].

Some early reports of the effect of Sc addition into AA2195-based alloys show that Sc slightly accelerates precipitation kinetics at 160 °C and lowers hardness during overaging [79]. Furthermore, it increases yield strength (YS) and ultimate tensile strength (UTS) but decreases the maximum elongation reached during tensile testing at room temperatures. The issue with Sc addition into DC-cast Al-Cu-Li-Mg-Zr-Sc-based alloys is the long-required holding times at high temperatures. While precipitation kinetics are somewhat improved, the dispersoids coarsen beyond the coherency limit, and the beneficial effect of grain refinement is diminished [129].

The employment of TRC for manufacturing Al-Cu-Li-Mg-Zr-Sc-based alloys could reduce this detrimental coarsening effect because the finer as-cast structure of the TRC strips requires shorter holding times at homogenization temperatures.

Recently, several attempts have been made to prepare TRC Al-Cu-Li-based alloys [87,130,131]. However, the structures of the cast strips exhibit strong centerline segregation and inhomogeneity of the alloying element distribution on a macroscopic scale due to a wide solid-liquid two-phase region. Regardless, the as-cast structures can be improved by optimizing the casting process and novel techniques, such as adding an electromagnetic field [130,131]. This addition to the TRC process can suppress turbulence and temperature fluctuations during casting, reduce temperature gradients on the front edge of the solidified shell, and induce electromagnetic stirring. All these effects help reduce segregation and secondary dendrite arm spacing (SDAS) [130,131]. While adding an electromagnetic field helps reduce the content of non-equilibrium phases after casting and microsegregation, the effect of plain TRC is already a significant improvement on these attributes over simple ingot casting [130].

However, the TRC strips lack the strengthening effect equivalent to the one imposed by the intensive rolling of ingot-cast materials. This strengthening could not be achieved through conventional methods because the strips already have a near-net shape. Conventional DC-cast AA2195 alloys can reach grain sizes as small as 10 μm through severe plastic deformation (SPD) methods such as equal channel angular pressing (ECAP). A fine-grained structure replaces the original microstructure of these alloys after four ECAP passes. The microstructure of the ECAP material is homogeneous, with a homogeneous distribution of grain misorientation. Without SPD, their grain size is around 30 μm [78,132,133]. Processed AA2195 alloys generally reach microhardness values around 190 HV and yield stresses above 500 MPa and up to 600 MPa after SPD processing. The maximal measured plastic strain is around 12 %, independent of the type of processing [78,79,106,134].

ECAP cannot be applied to TRC materials. Therefore, refinement should be achieved by SPD methods applicable to sheets, such as asymmetric rolling or constrained groove pressing (CGP).

1.4.3. Rolling

Rolling is a simple method of forming materials into sheets. Input material is fed between two rotating steel rolls whose gap is lower than its thickness. Depending on the rolling setup, rolling can be symmetric or asymmetric.

Asymmetric rolling can be achieved through several means – different roll diameters, different rotation speeds, or different friction coefficients. All these conditions lead to different speeds of the rolled sheet surfaces. The ratio between roll sizes/speeds/friction coefficients can characterize the asymmetry of the process. Different speed setups are the most common due to their greater versatility than changing entire rolls. Increasing the asymmetry leads to higher shear deformation up to a certain point [135]. The final sheet is bent due to the asymmetry of the process. In the case of asymmetric rolling with different roll speeds, high reductions lead to curvature towards the roll with a higher speed. In comparison, lower reductions cause bending towards the roll with a lower speed, as reported by Li et al. [136].

Rolling routes play an essential role during asymmetric rolling. The material can be rotated along any direction or not at all between subsequent passes. Rotation along RD and ND is reported to promote the formation of ideal shear textures [135,137] but can be challenging to produce throughout the entire strip [138]. Increasing the asymmetry ratio increases the penetration of shear strain and leads to texture softening of the rolled product. Asymmetric rolling also affects texture after recrystallization with a tendency towards texture randomization with stable existing <111>//ND shear components [135].

1.4.4. Constrained groove pressing

Initially developed by Shin et al. [139], CGP is among the methods developed for SPD of sheet metals with the intention of grain refinement. In the CGP process, the material is subjected to repetitive shear deformation by alternating pressing between two asymmetrically aligned grooved and flat dies [140]. Each complete pass consists of four stages – two in a grooving die and two in a straightening die (Figure 1.10). The upper and lower die gap is equivalent to the sample thickness. During grooving, the inclined part in the groove is subjected to pure shear deformation with a shear strain of 1, and the flat part is not deformed at all, corresponding to an effective strain of 0.58 across the strip [139,141]. The same strain is applied in the straightening operation, causing an effective strain of 1.16 after the first two CGP steps in the deformed regions [140,142]. After the first two steps, the sheet sample is rotated 180 °C around the axis perpendicular to the sheet plane. The following two steps are performed the same way, resulting in the deformation of the previously undeformed regions due to asymmetry of the forming die and, in an ideal case, a homogeneous strain distribution throughout the specimen. While CGP provides several advantages, such as the supposed homogeneity of strain, it cannot reach the total strains of other SPD methods in a single pass/cycle.

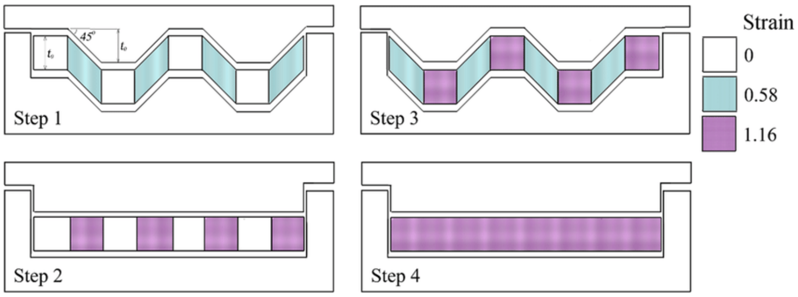

Figure 1.10: Schematic representation of the CGP four-step cycle [143].

Analysis of pure Al CGP sheets revealed elongated grains with a banded structure. The banded structure contained polygonized subgrains due to dynamic recovery during the straining. No microstructural changes were observed between a sheet after one and four complete passes [144]. Significant refinement after a first pass and only minor dynamic recovery-induced changes after further passes are typical for a wide range of SPD methods, such as ECAP or accumulative roll bonding (ARB) [140]. Several studies suggest that while dislocation density, refinement, and hardness all increase with successive passes, the rate of increase is lower with each pass, and dynamic recovery limits further growth after approximately 6-7 passes [139,140,145,146].

The effect of CGP on mechanical properties is well documented. In general, CGP specimens have higher strength compared to undeformed specimens. The general trend of strength copies the grain size evolution – the strength increases to a certain number of passes, with the increment being lower after each pass. However, this comes at the cost of lower ductility [141]. The strength of alloys increases more than that of pure metals due to dispersoid particles, which further increase the work hardening [141].

2. Stated goals

The present study aims to find a potential thermomechanical processing route for model Al-Cu-Li-Mg-Zr-Sc-based alloys using approaches of physical metallurgy in the following steps:

- Determination of the influence of the solidification rate and casting method on the as-cast microstructure of this system and optimal homogenization conditions to achieve peak mechanical properties
- Characterization of processes occurring in the cast materials during exposure to temperatures reaching the temperature of standard homogenization and solution treatment
- Subjecting the material to texture-modifying plastic deformation to achieve optimal tensile properties
- Characterization of the materials in peak-aged conditions
- Assessment of the role of Sc in the entire process

3. Experimental methods, materials, processing

3.1. Microscopy

3.1.1. Scanning electron microscopy

Scanning electron microscopes (SEM) Zeiss Auriga Compact, FEI Quanta 200F, and Thermofisher Apreo 2 were used to characterize materials on mesoscopic scales through secondary electron (SE) and backscattered electron (BSE) contrasts. The two contrasts are more sensitive to surface morphology (SE) and composition (BSE) [147]. Samples for SEM BSE and SE observations were prepared by polishing with SiC papers and subsequently with a colloidal silica suspension.

These microscopes also have energy-dispersive X-ray spectroscopy (EDS) detectors used primarily for composition mapping and electron backscatter diffraction (EBSD) cameras for statistical grain size, texture, and grain shape evaluations. EBSD evaluates the orientation of each scanned point from Kikuchi line patterns, which are formed by the diffraction of inelastically backscattered electrons. Individual grains are separated by high-angle grain boundaries (HAGBs) – the misorientation between two points in neighboring grains is higher or equal to 15 °. Samples for EBSD analysis were prepared as samples for regular SEM observations and subsequently electrochemically etched at -15 °C with a solution of 33 % HNO_3 in methanol. Thin melt spun samples were prepared for EBSD in a "slope cutting" holder in the Leica EM RES102 ion polisher.

3.1.2. Transmission electron microscopy

Two transmission electron microscopes (TEMs) were used - the TEM JEOL 2000FX and JEOL 2200FS. Both microscopes suit the standard bright field (BF) and dark field (DF) observations. Selected area electron diffraction (SAED) can be employed for phase identification and sample orientation. The JEOL 2200FS can also be switched into scanning transmission (STEM) mode. The STEM mode allows BF and high-angle annular DF (HAADF) imaging. Additionally, the microscope is equipped with a high-angle solid-state EDS detector JEOL Centurio, allowing for better elemental mapping than one received in SEM. The 2200FS TEM is also capable of high-resolution (HRTEM) imaging. Both TEMs are equipped with heating holders.

Samples for TEM are prepared in the form of 3 mm discs, which are punched from materials polished to 100 – 150 μm thickness by SiC papers. These discs are then electrolytically polished by a solution of 33 % HNO_3 in methanol at -20 °C and 16 V. If standard disc preparation was not possible (such as in the case of melt-spun materials), a thin lamella was prepared by milling from a selected area by focused Ga ion beam (FIB) milling in the Zeiss SEM.

3.2. Mechanical properties

3.2.1. Microhardness measurements

Microhardness measurements determine the average hardness value of an entire studied sample during aging. The average value was based on a minimum of 15 indentations.

Microhardness is established by pushing a diamond-tipped indentor into the studied material with a defined force for a set loading time. The indentation is then measured, and its size is used to determine the hardness value. All the presented hardness values are measured using the Vickers indentor – a simple pyramid. The relation between the indentation size and microhardness is:

$$HV = 1.8544 \frac{F}{{d_I}^2}, \tag{3.1}$$

where F is the applied force, and d_I is the average indentation diagonal [148]. Microhardness was measured using the automatic Qness Q10+ testing machine for indentation and evaluation with a 100 g load where possible. The machine measures diagonals d_1 and d_2 and uses their average for calculating microhardness (Figure 3.1). The thin melt spun samples were measured with a load of 2 g and then evaluated manually in SEM.

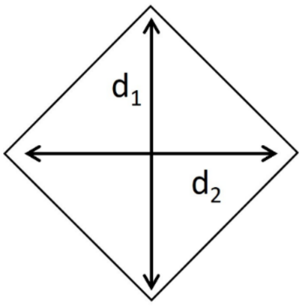

Figure 3.1 Microhardness indentation schematic.

3.2.2. Tensile tests

While hardness can be used to evaluate the development of mechanical properties during a process, it cannot assess the exact strength and ductility of the material. Tensile testing was performed to determine these mechanical properties.

Samples for tensile testing were dog-bone-shaped samples prepared by CNC cutting. The exact dimensions of the used samples are in Figure 3.2. Instron 5882 testing machine was used to perform these tests. Prepared samples were subject to uniaxial tension at a 10^{-3} s^{-1} strain rate. These tests were performed at room temperature. The Instron tensile testing machine was also used to pre-deform selected samples before aging. The deformation rate was $5 \cdot 10^{-4}$ s^{-1} to reach the desired strain, which was always 3 %. The results reported in the study are average values of three measurements.

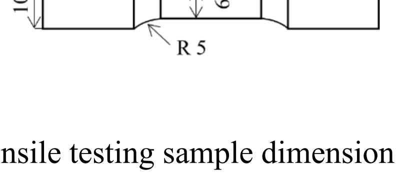

Figure 3.2 Tensile testing sample dimensions in milimeters.

3.3. Materials and processing

3.3.1. Casting

Two alloys, based on the standard AA2195 alloy, were studied in this thesis. The materials are Al-Cu-Li-Mg-Zr-based with a similar ratio of alloying elements as the standard alloy but with a reduced total concentration of alloying elements. One alloy (alloy A) also contains an addition of Sc (Table 3.1), while the other is Sc-free (alloy B). Both materials were cast using mold casting, twin-roll casting, and melt-spinning. The composition was determined from multiple optical emission spectroscopy measurements using the Bruker Q4 TASMAN spectroscope on the mold-cast and twin-roll cast materials. Input material for melt-spinning was obtained by remelting as-cast pieces of TRC strips.

The mold-cast materials (MC) were melted at 900 °C in an argon atmosphere and cast into an air-cooled graphite mold. This original ingot was 110 x 56 x 26 mm^3. The surface of the ingots was scalped after casting. The dimensions of the provided ingots are 85 x 50 x 22 mm^3.

The twin-roll cast (TRC) materials were cast using a vertical caster with steel outer shells. The strips were approximately 3 mm thick and 200 mm wide. The alloys were melted under a protective Ar atmosphere at 900 °C. Their pouring temperature was 660 °C. The casting speed for both alloys was set at 3.6 $m \cdot s^{-1}$.

The melt-spun (MS) materials were cast using boron nitride nozzles at a 0.22 mm distance from the water-cooled copper roll spinning at 1500 rpm. Both materials were preheated to 1000 °C before casting. The Sc-containing material was cast using a 10 x 0.55 mm^2 nozzle, and the Sc-free material used a 6 x 0.8 mm^2 nozzle.

The mold-cast materials have no principal directions. The remaining two materials have them and will be referred to as rolling directions (RD), transversal direction (TD), and normal direction (ND) (Figure 3.3).

Table 3.1 Compositions of the two alloys in wt. %.

	Cu	Li	Mg	Zr	Sc	Ag	Ti	V	Fe	Al	Other
Alloy A	2.61	0.71	0.27	0.1	0.17	0.29	0.01	0.01	0.09	95.32	bal.
Alloy B	2.52	0.72	0.27	0.12	-	0.33	0.02	0.02	0.09	95.99	bal.

The text refers to the individual alloy/casting method combinations as MCSc and MC for the mold-cast alloys A and B, TSc and T for the twin-roll cast alloys A and B, and MSSc and MS for melt-spun alloys A and B.

3.3.2. Processing

Thermal processing of the studied materials consists of three-stage homogenization/solution annealing at 300 °C, 450 °C, and 530 °C. These stages are performed for 30 min each for the MC and TRC materials and 5 minutes each for the MS materials due to a finer as-cast structure.

Materials intended for CGP and rolling were first annealed at 300 °C and 450 °C to facilitate the formation of Al_3Zr or $Al_3(Sc,Zr)$ precipitates. These precipitates affect dynamic recrystallization and recovery during the deformation and static processes during the final 530 °C annealing step. These deformation processes include constrained groove pressing and rolling.

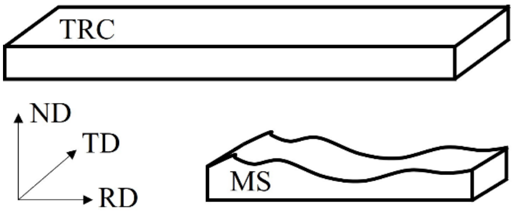

Figure 3.3 Schematic showing the principal directions in as-cast TRC and MS strips.

Rolling was done either symmetrically or asymmetrically, depending on whether both rolls had the same speed. Materials for rolling were preheated to 300 °C. Asymmetrical rolling was done with an asymmetrical ratio of four, with the top roll of the horizontal roller having four times higher revolutions per minute than the bottom roll. The total thickness reduction in either rolling was 50 %, done in four passes. Materials were flipped along the axis parallel to the rolling direction between each pass (Figure 3.4). Samples for rolling were approximately 15 cm long and 3 cm wide.

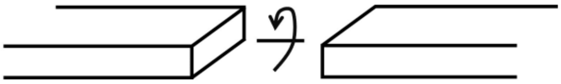

Figure 3.4 Schematic of the selected rolling route for asymmetric rolling.

CGP was done as described in part 1.4.4 by pressing the preheated material between corrugating and straightening dies. Materials for CGP were preheated at 450 °C. The constrained groove is 7 cm wide and can accommodate samples up to 5 cm long. After each straightening step, the material is rotated along the axis perpendicular to the surface. The applied force during pressing was approximately 20 kN. The duration of each pressing step from extraction from the furnace to insertion back into it is approximately one minute.

Materials after the three-stage heat treatment (further referred to as "standardized" materials/"standardization annealing") were then aged either with or without deformation. Materials studied in the T6 temper were not deformed and directly aged at 180 °C for as long as necessary or up to 100 h, depending on the experiment. Materials studied in the T8 temper were plastically deformed by 3 % directly after standardization and then aged at the same temperature.

4. Results and discussion

The bulk of the study is focused on twin-roll cast materials, which were subjected to a wide range of thermomechanical treatments to find optimal mechanical properties. The main benefit of using twin-roll cast materials is the potential of a short-term combined homogenization/solution treatment, which leads to high potential savings thanks to lower energy consumption associated with homogenization. Mold-cast and melt-spun materials provide an additional frame of reference highlighting the influence of a wide range of solidification rates during casting on the as-cast states and subsequent thermomechanical processing.

4.1.As-cast materials characterization

4.1.1. Mold-cast materials

Figure 4.1 shows grain orientation maps of a 3x3 mm^2 EBSD scanned area of the initial mold-cast materials. Grain orientation is color-coded according to the IPF triangle shown in Figure 4.1 (c). Neither material has a substantial subgrain structure in the as-cast state. Grain shapes in the MC material (Figure 4.1 (a)) are more regular than in the MCSc material. Irregularity in the MCSc material originates from grain boundary pinning by Sc-rich particle clusters (highlighted by white arrows in the inset of Figure 4.1 (b)). The average grain size of the studied materials is determined by the circular intercept method [149]:

$$GS = 1.6\frac{l}{N_i}, \tag{4.1}$$

where l is the circumference of a circle, and N_i is the number of intercepted grains by the circle. The average grain size is (156 ± 11) μm and (130 ± 17) μm for the MC and MCSc material, respectively.

The primary phase precipitates formed during casting are typically the θ(Al_2Cu) phase, the Al_7Cu_2Fe phase, or the S(Al_2CuMg) phase in addition to the W($Al_{8-x}Cu_{4+x}Sc$) phase in the MCSc material [5,17,79,118]. EDS measurements also confirm the presence of these phases (Table 4.1). Li cannot be detected by EDS (Figure 4.2), but Li-containing precipitates (Al_6CuLi_3) have also been previously identified in these types of materials [150]. Formation of the W($Al_{8-x}Cu_{4+x}Sc$) phase is a detrimental effect caused by the low solidification and cooling rates. However, DePottey et al. [118] note the segregation of Sc to the eutectic Al-Cu θ-phase during casting and formation of the W phase at cooling rates between 0.1 K·s^{-1} and 1 K·s^{-1} and a lack of this phase above 10 K·s^{-1}.

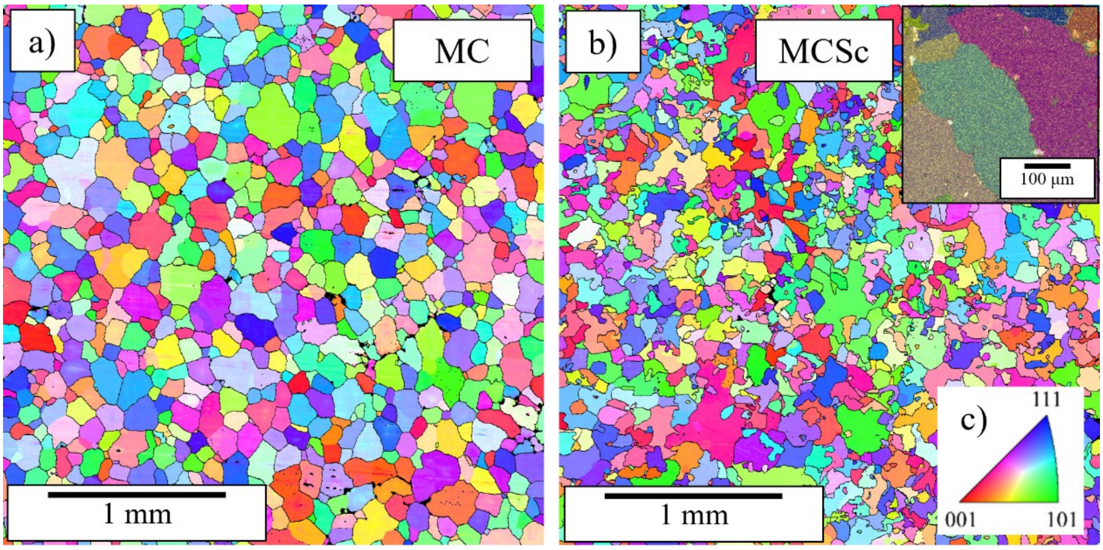

Figure 4.1 Grain orientation maps of the mold-cast materials as determined by EBSD measurements of a random 3x3 mm^2 area. Orientation map of the MC (a) and MCSc (b) material. Insets in the MCSc map show grain boundary pinning by the Sc-rich particle clusters (bright yellow clusters highlighted by white arrows) and IPF triangle with the orientation color coding (c).

Cu is the main element evaluated to study matrix concentration. Cu is crucial for strengthening during further processing while having a lower diffusion coefficient than the two other strengthening additions – Li and Mg [28]. The concentration of Cu in the matrix is the same for both materials – 0.8 wt. %. Areas of EDS measurements are highlighted in Figure 4.2 (f,q).

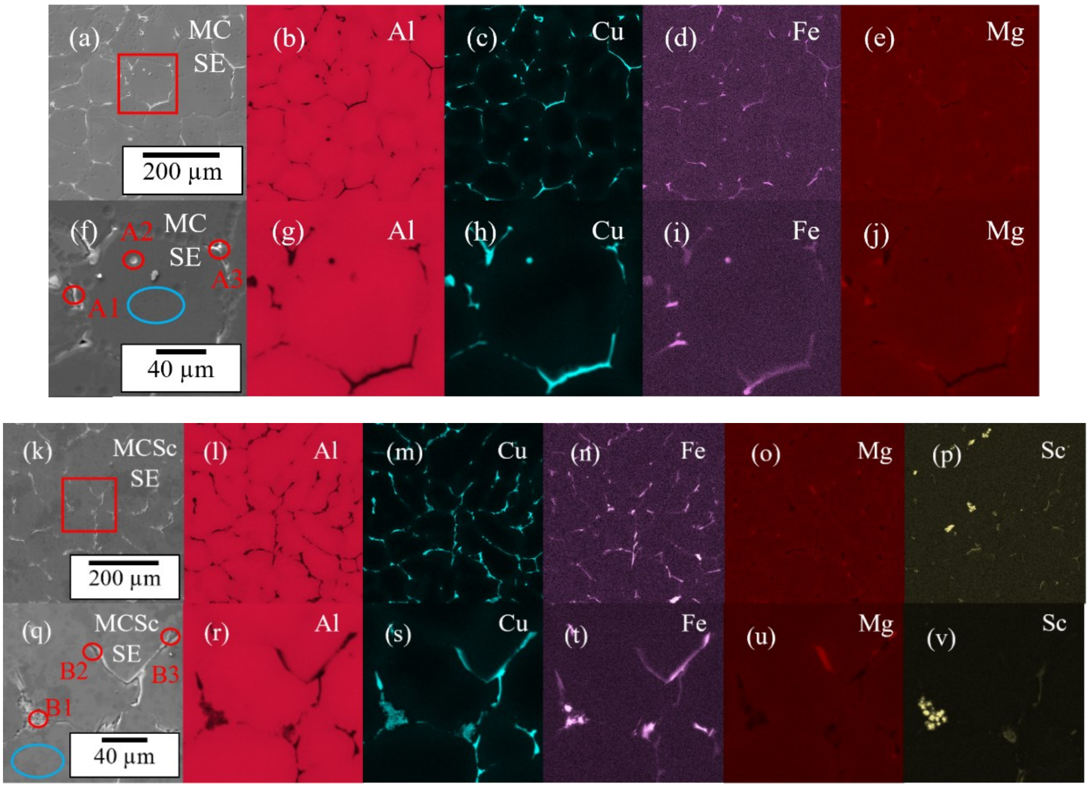

Figure 4.2 EDS mapping results of the mold-cast material. Overview of a larger area (a-e), (k-p), and higher magnification maps of selected sections (f-j), (q-v) for the MC (a-j) and MCSc (k-v) materials. SE contrast images of the mapped areas (a,f,k,q), Al maps (b,g,l,r), Cu maps (c,h,m,s), Fe maps (d,i,n,t), and Mg maps (e,j,o,u) for both materials. Sc distribution maps (p,v) for the MCSc material. Red squares highlight the selected areas for higher magnification analysis. Red circles highlight areas for particle point analyses. Blue ovals highlight the regions chosen for matrix Cu concentration measurements.

Table 4.1. EDS point analyses of particles and areas of the Al matrix highlighted in Figure 4.2 (f,q). Values in wt. %.

	Cu	Fe	Mg	Sc
A1	9.5	0.1	2.3	-
A2	31.9	1.0	1.4	-
A3	31.8	0.2	1.8	-
T matrix	0.8 ± 0.1	0.03 ± 0.01	0.9 ± 0.2	-
B1	23.6	2.7	0.9	8.5
B2	20.9	3.6	1.6	0.2
B3	20.3	0.1	4.4	0.1
TSc matrix	0.8 ± 0.1	0.04 ± 0.02	1.0 ± 0.2	0.6 ± 0.2

A proper homogenization procedure requires the dissolution of the primary phases and redistribution of the main alloying elements. Microsegregation in these materials occurs across individual eutectic cells. The average size of these cells (eutectic cell size – ECS) can be determined using the circular intercept method from lower magnification SEM images (Figure 4.3) and serves to calculate an estimate of the necessary homogenization time in these materials. Additionally, DAS is determined as a tip-to-tip distance between individual dendrites from the same images using the linear intercept method (Equation 4.1), which serves as a parameter for the characterization of solidification kinetics. DAS is lower in general due to the elongated shape of the dendrites.

Volume fractions of particles are calculated by using the intercept method and the stereographic Tomkeieff equation [151], which states the volume fraction f_V of particles as:

$$f_V = 2N_iL_i, \tag{4.2}$$

where N_i is the number of intercepted phases per unit line length, and L_i is the length of the intercepted particle segment. Intercepts are measured manually from a set of lines in an evenly spaced and randomly offset perpendicular grid. The measured DAS of the two alloys is the same within error with (60 ± 10) µm and (82 ± 12) µm for the MC and MCSc materials, respectively. Volume fractions of the primary phases evaluated by SEM (Figure 4.3) are 4.8 % and 5.1 % for the MC and MCSc materials, respectively. ECS was calculated as (103 ± 5) µm and (123 ± 8) µm respectively (Table 4.2).

The eutectic cell boundary phases are rod-shaped in the observation plane and are (34 ± 10) µm long and (3.0 ± 1.5) µm thick (Figure 4.3). The W($Al_{8-x}Cu_{4+x}Sc$) phase appears as an irregular cluster of particles. The size of these clusters is (11 ± 5) µm (Figure 4.2 (p,v)).

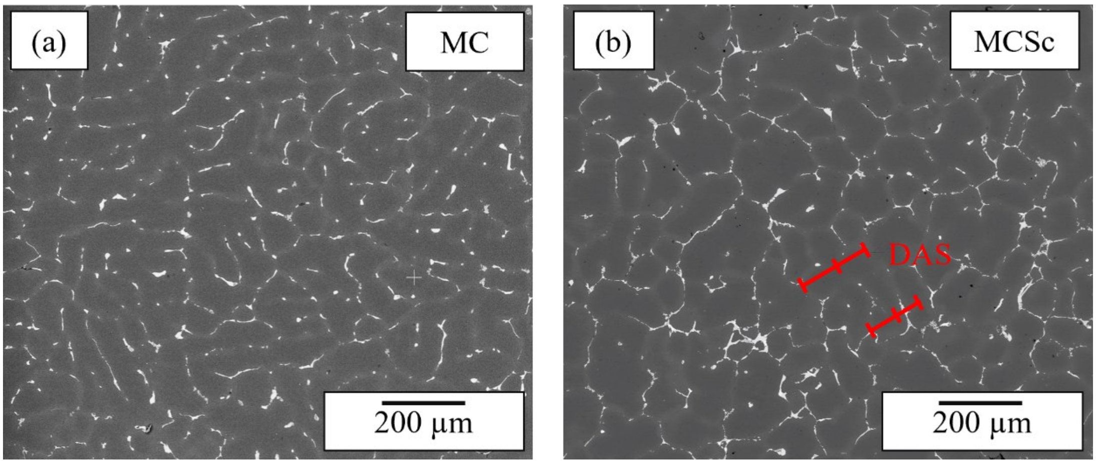

Figure 4.3 BSE contrast images of the MC (a) and MCSc (b) materials. DAS measured from these images highlighted by a red line.

Table 4.2 Summary of measured structural parameters (DAS, ECS, GS) of the as-cast states of the mold-cast materials. Sizes in µm.

	MC	MCSc
DAS	60 ± 10	82 ± 12
ECS	105 ± 3	123 ± 8
GS	156 ± 11	130 ± 17

4.1.2. Twin-roll cast materials

Grain orientation maps of 1 mm broad surface-to-surface cross sections of the twin-roll cast strips are shown in Figure 4.4. The material is evaluated from the transversal direction (TD). A single grain size average calculated by the circular intercept method could be misleading due to grain size differences throughout the strip. Therefore, the strips were evaluated using the circular intercept method in three regions – close to the surface, halfway between the surface and the center, and in the center. These regions are further referred to as Areas 1, 2 and 3. The evaluated grain sizes are summarized in Table 4.3. The average grain size of both materials increases from Area 1 to Area 2 but decreases again in Area 3 (Table 4.3).

EDS mapping reveals no presence of the W($Al_{8-x}Cu_{4+x}Sc$) phase (Figure 4.5) due to the increased cooling rates of twin-roll casting preventing its formation [118]. The TRC materials primarily contain the θ(Al_2Cu) phase and a ternary Al_7Cu_2Fe phase; increased Mg concentration suggests the presence of the S(Al_2CuMg) phase (Table 4.4) [150]. Primary phases exclusively form along boundaries of eutectic cells, creating continuous polygonal segments in the observation plane (Figure 4.6), with individual segments being (5 ± 2) μm long and (1.0 ± 0.5) μm thick. The volume fraction of phases decreases only slightly and does not significantly change between the surface and the center. The average volume fraction of primary phases is 4.4 % and 4.3 % for the T and TSc materials, respectively. The primary phase size does not differ between the two alloys.

Due to the variance in solidification rates across the strip thickness, the DAS is individually evaluated in Areas 1, 2, and 3 (Figure 4.6 – (b-d), (f-h)). The average DAS for each region is summarized in Table 4.3. The measured DAS increases by about 40 % from the surface to the center for both materials and is lower overall for the TSc material. The concentration of the main alloying elements is the same within the experimental scatter across the strip in intragranular spaces (Table 4.3).

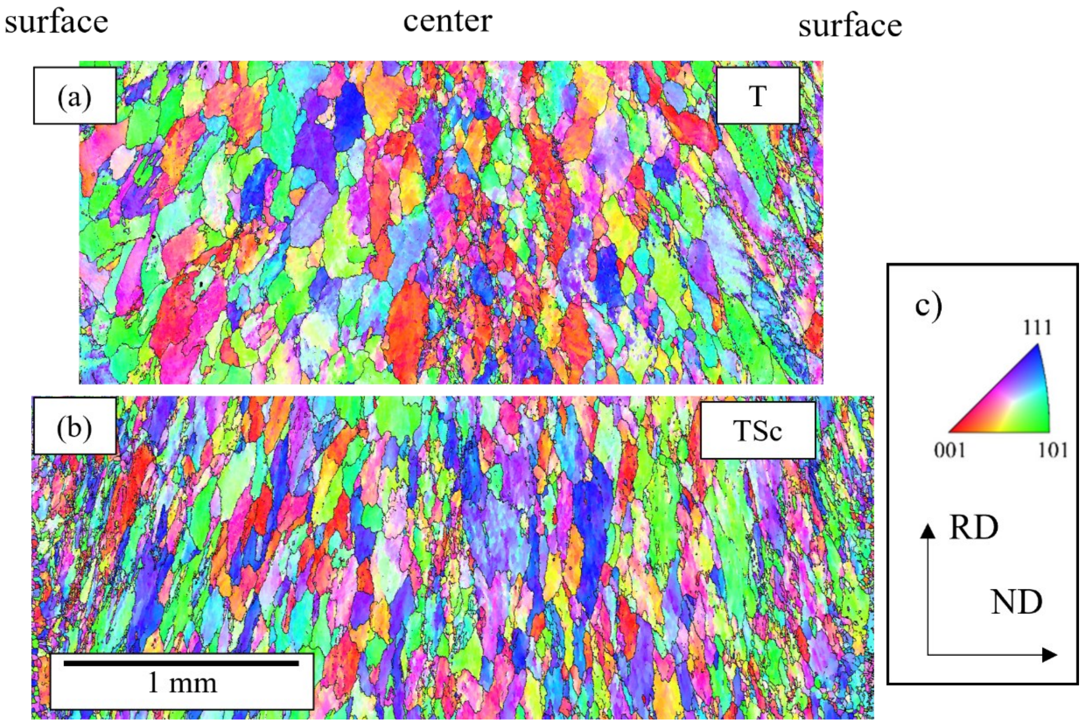

Figure 4.4 Grain orientation maps of the T (a) and TSc (b) materials - surface-to-surface cross sections. RD and ND respective to the sample and the color coding triangle (c).

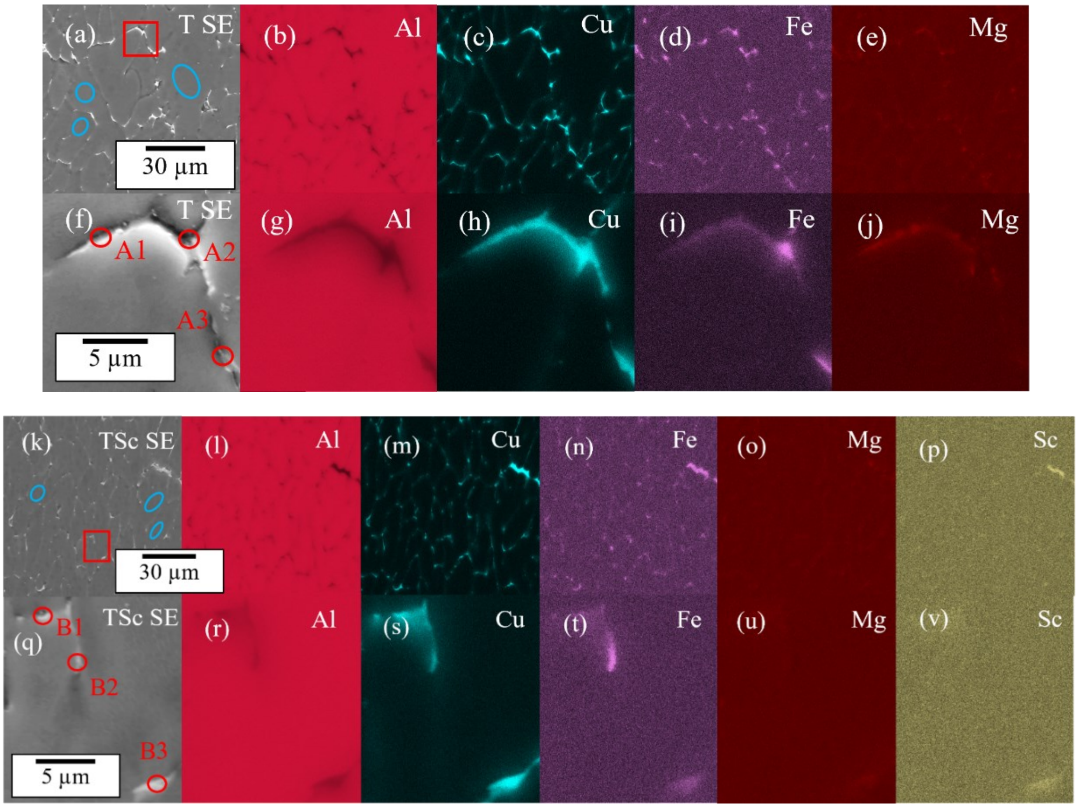

Figure 4.5 EDS mapping of the as-cast T (a-j) and TSc (k-v) materials. Lower magnification overview images (a-e, k-p) and closeups of highlighted sections (f-j,q-v). SE contrast images (a,f,k,q), Al (b,g,l,r), Cu (c,h,m,s), Fe (d,i,n,t), and Mg maps (e,j,o,u) of both materials. Sc maps in the TSc material (p, v). Blue ovals highlight areas of EDS measurements of matrix concentrations. Red ovals highlight areas of particle point analyses.

Table 4.3 Dendrite arm spacing (DAS), grain sizes (GS), and eutectic cell size (ECS) evaluated in three areas of the twin-roll cast strips

	T DAS [µm]	T GS [µm]	T ECS [µm]	TSc DAS [µm]	TSc GS [µm]	TSc ECS [µm]
Area 1	6.5 ± 0.3	64 ± 9	13 ± 4	5.7 ± 0.8	51 ± 5	10 ± 3
Area 2	7.4 ± 0.5	95 ± 7		7.8 ± 0.9	80 ± 20	
Area 3	9.4 ± 0.8	58 ± 4		8.6 ± 0.6	56 ± 2	

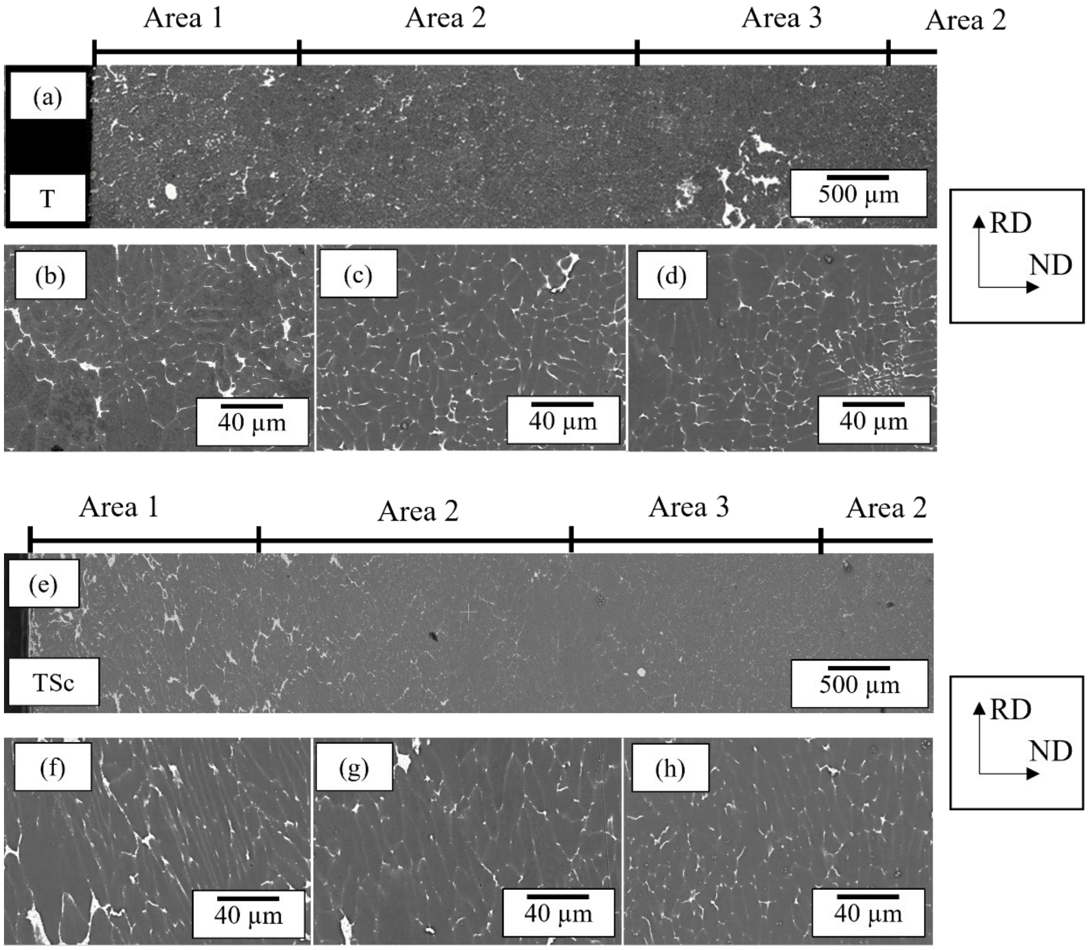

Figure 4.6 BSE contrast SEM images of T (a-d) and TSc (e-h) material microstructure. Surface-to-center overviews (a,e) and close-ups of Area 1 (b,f), Area 2 (c,g), and Area 3 (d,h) of both materials. RD and ND are indicated (black square).

Table 4.4 EDS analyses of the selected primary phase precipitates in the TRC materials and matrix concentrations in the studied areas (Figure 4.5). Concentrations in wt. %.

	Cu	Fe	Mg	Sc
A1	18.4	0.6	2.7	-
A2	27.1	2.2	2.1	-
A3	17.4	1.3	1.6	-
T (Area 1)	1.1 ± 0.2	0.04 ± 0.01	1.0 ± 0.3	-
T (Area 2)	1.0 ± 0.2	0.03 ± 0.02	1.0 ± 0.2	-
T (Area 3)	1.0 ± 0.1	0.05 ± 0.02	0.9 ± 0.3	-
B1	11.6	0.5	1.4	0.5
B2	8.5	1.7	1.1	0.4
B3	17.6	0.4	1.8	0.4
TSc (Area 1)	1.2 ± 0.2	0.06 ± 0.03	0.9 ± 0.2	0.7 ± 0.2
TSc (Area 2)	1.1 ± 0.2	0.03 ± 0.01	1.2 ± 0.3	0.6 ± 0.1
TSc (Area 3)	1.1 ± 0.1	0.04 ± 0.02	0.8 ± 0.1	0.7 ± 0.3

4.1.3. Melt-spun materials

The contact side of the melt-spun strips grows tiny grains on the surface, followed by columnar grains perpendicular to the surface of the roll (Figure 4.7, Zone 2). Due to the instability of the casting process, the resulting strip thickness varies between 15 µm and 60 µm. Equiaxed grains (Zone 3) form at a certain distance from the surface. The circular intercept method is employed in the columnar and equiaxed areas to calculate grain sizes, as listed in Table 4.5.

The local solidification regime determines primary phase particle distribution. A macroscopic featureless region (Zone 1), as described in the introduction (Gusakova et al. [94,96]), is not clearly defined in the studied melt-spun strips (Figure 4.8 (b,f)). The columnar areas (Zone 2) contain spherical precipitates inside the individual grains. Close to the contact surface, these phases have a (50 ± 7) nm diameter, while close to the columnar/equiaxed threshold, they have a diameter of (150 ± 40) nm. The volume fraction of primary phases changes significantly from the surface/roll interface towards the equiaxed part of the strips. The surface region contains only a 1.7 % volume fraction of primary phases, increasing to 2.8 % in the columnar area and 4.1 % in the equiaxed part of the strip. The measured volume fractions of primary phases are the same for both alloys.

EDS mapping performed in STEM of areas close to the surface of the strip reveals the presence of two types of phases – more rounded Cu-rich phases, likely the stable θ phase, and rod-like Cu and Fe-containing phases, likely the Al_7Cu_2Fe phase (Figure 4.9). No significant Sc segregation is observed in the MSSc material. DAS can only be established in the equiaxed region since it is the only part of the material formed by dendritic growth (Table 4.5) [94,96].

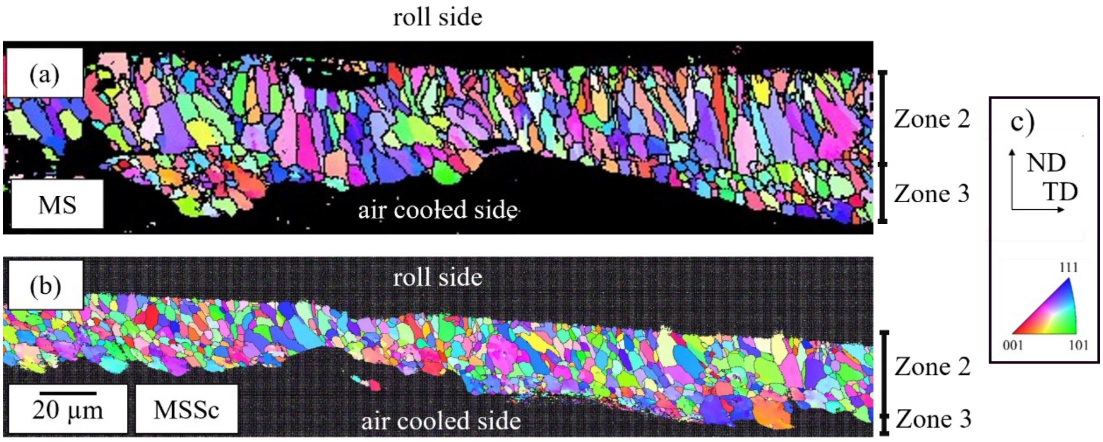

Figure 4.7 IPF maps of the MS (a) and MSSc (b) materials cross sections from the surface/roll interface (top) to the air-cooled side of the strip (bottom) analyzed from the rolling direction (RD). Zone 1 is not evident in EBSD measurements. Zones 2 and 3 are highlighted in the materials. Orientation of the strip and the color-coding triangle (c).

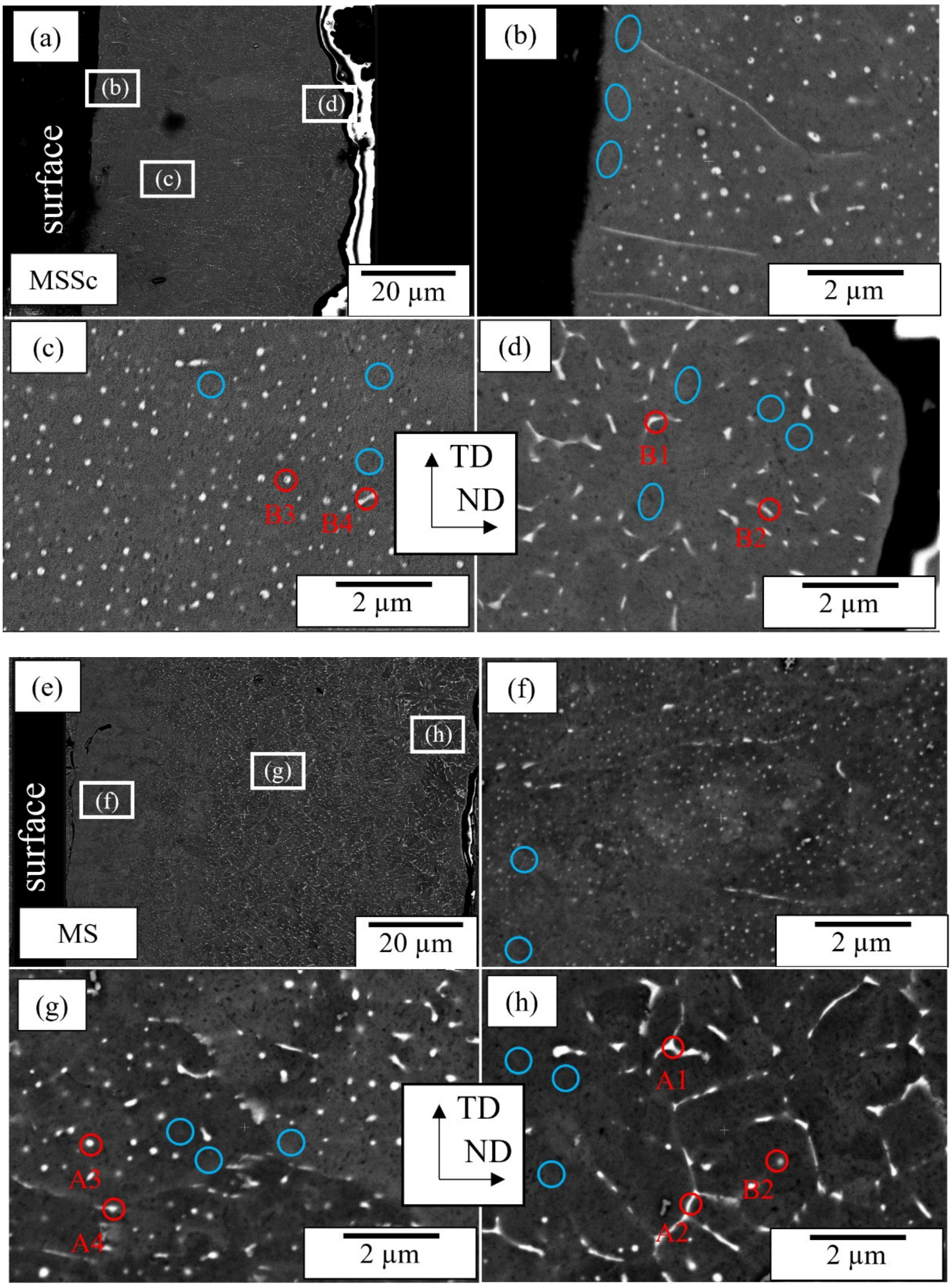

Figure 4.8 BSE contrast SEM micrographs of the MS (a-d) and MSSc (e-h) materials. Overview images taken from the RD (a,e) and closeup areas of individual zones highlighted by white rectangles (b-d), (f-h). Closeups of Zone 1 (b,f), Zone 2 (c,g), and Zone 3 (d,h). Blue circles indicate areas of Cu concentration measurements. Red circles highlight particles in which EDS concentration measurements were performed.

Matrix concentration in the melt-spun materials is higher than in the previous casting types but varies across the melt-spun strips. Both materials show comparable matrix concentrations in the evaluated regions. EDS analyses of selected particles and matrix concentrations in the highlighted zones are summarized in Table 4.6. The particles analyzed are boundary particles in the equiaxed region (particles A1, A2, B1, B2 in Figure 4.8 (d, h)), a spherical particle in the columnar region (particles A3, B3 in Figure 4.8 (c, g)), a boundary particle in the columnar region (particles A4, B4 in Figure 4.8 (c, g)) and two particles close to the surface/roll interface (A5, A6, B5, B6 in Figure 4.9 (a, f)). EDS analyses performed in SEM and STEM show increased Fe content in the primary phases, implying the presence of Al_7Cu_2Fe precipitates. Mg content in the selected phases is not higher than in the matrix in either SEM or STEM. STEM and SEM EDS analyses could not be directly compared because the information depth of the SEM beam is higher than the particle size. Therefore, the SEM point EDS spectra are substantially affected by the surrounding Al matrix.

Table 4.5 Summary of DAS, ECS, and grain sizes in Zone 2 (columnar) and Zone 3 (equiaxed).

area	MS DAS [μm]	MS GS [μm]	MS ECS [μm]	MSSc DAS [μm]	MSSc GS [μm]	MSSc ECS [μm]
columnar	-	5.8 ± 1.0	-	-	4.5 ± 0.3	-
equiaxed	0.6 ± 0.2	4.8 ± 0.9	0.8 ± 0.1	0.6 ± 0.1	4.5 ± 0.4	1.0 ± 0.1

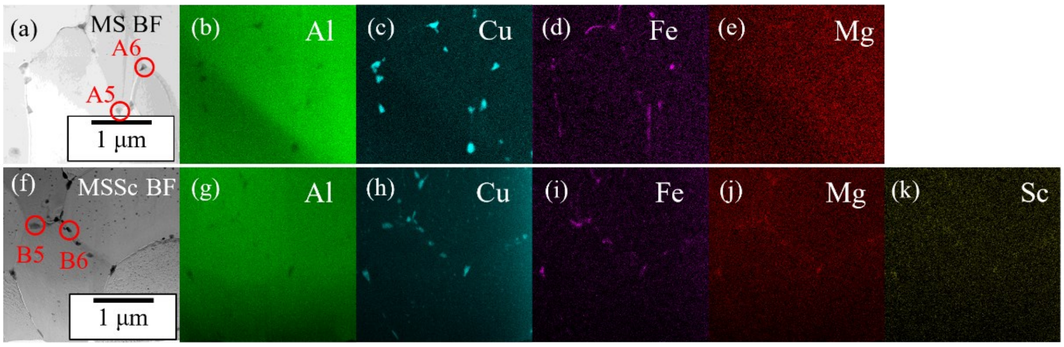

Figure 4.9 EDS mapping of the MS (a-e) and MSSc (f-k) materials. STEM BF micrographs of the mapped areas (a, f), corresponding Al (b,g), Cu (c,h), Fe (d,i), and Mg (e,j) maps of both materials. Sc map of the MSSc material (k).

Table 4.6 EDS analyses of selected particles (red circles in Figure 4.8, Figure 4.9) and average concentrations in the matrix (blue circles in Figure 4.8, Figure 4.9). Concentrations in wt. %.

			Cu	Fe	Mg
MS	Matrix	Zone 1	1.4 ± 0.1	0.3 ± 0.2	0.8 ± 0.1
		Zone 2	2.1 ± 0.3	0.6 ± 0.2	1.1 ± 0.1
		Zone 3	2.5 ± 0.3	0.5 ± 0.1	1.2 ± 0.2
	Particle	A1	11.1	1.2	1.0
		A2	9.8	1.0	1.3
		A3	8.3	0.6	1.0
		A4	6.0	1.0	1.0
		A5	44.0	2.5	0.1
		A6	56.9	0.4	0.0
MSSc	Matrix	Zone 1	1.2 ± 0.2	0.3 ± 0.1	1.0 ± 0.1
		Zone 2	2.2 ± 0.2	0.7 ± 0.2	1.0 ± 0.3
		Zone 3	2.6 ± 0.3	0.4 ± 0.1	0.9 ± 0.1
	Particle	B1	12.9	0.9	1.2
		B2	14.0	0.7	1.1
		B3	19.0	1.4	1.1
		B4	16.5	3.4	1.1
		B5	59.2	0.8	0.0
		B6	34.7	5.0	0.0

4.1.4. As-cast states summary - the influence of solidification rate

Both alloys have structures consistent with the commonly reported behavior of materials with varying solidification rates. The microstructure of the studied materials gets progressively more refined with increasing solidification rates. The essential properties of all the studied materials, including particle widths *w*, are summarized in Table 4.7.

Table 4.7 Structural parameters of all the materials.

		w [μm]	f [%]	DAS [μm]	ECS [μm]	matrix Cu concentration [wt. %]
MC		3.2 ± 1.4	4.7 ± 0.4	60 ± 10	103 ± 5	0.8 ± 0.2
MCSc		2.9 ± 1.6	5.2 ± 0.3	82 ± 12	125 ± 8	0.8 ± 0.2
T	Zone 1	1.1 ± 0.5	4.4 ± 0.3	6.5 ± 0.3	13 ± 4	1.1 ± 0.2
	Zone 2			7.4 ± 0.5		
	Zone 3			9.4 ± 0.8		
TSc	Zone 1	1.0 ± 0.4	4.2 ± 0.7	5.7 ± 0.8	10 ± 3	1.2 ± 0.2
	Zone 2			7.8 ± 0.9		
	Zone 3			8.6 ± 0.6		
MS	Zone 1	0.05 ± 0.01	1.8 ± 0.4	-	-	2.5 ± 0.3
	Zone 2	0.11 ± 0.03	3.1 ± 0.4			2.1 ± 0.3
	Zone 3	0.13 ± 0.05	4.0 ± 0.5	0.6 ± 0.2	0.8 ± 0.1	1.4 ± 0.1
MSSc	Zone 1	0.04 ± 0.01	1.6 ± 0.3	-	-	2.6 ± 0.3
	Zone 2	0.11 ± 0.02	2.6 ± 0.5			2.2 ± 0.2
	Zone 3	0.16 ± 0.06	4.2 ± 0.4	0.6 ± 0.1	1.0 ± 0.1	1.2 ± 0.2

Solidification rates

Solidification rates associated with different casting methods were calculated from dendrite spacing where possible. The values of n and A (Equation 1.5) were calculated within the limits established in an Al-Cu-based alloy dendrite spacing review by Eskin et al. [86], who limit the value of n to 0.33 (Equation 1.5) and determined new A coefficients for alloys with 2.12 (A=84) and 3.24 (A=101) wt. % Cu. Based on their coefficients, we will use their fixed value of n and an interpolated value of $A = 93$. These values ignore the influence of Zr and Sc on DAS. While these additions have a strong influence over grain structure (Xu et al. [152] an order of magnitude difference of grain size in Al-Mg-Si-based alloys), their influence on SDAS is significantly lower (Xu et al. [152] around 25 % decrease of DAS, Prach et al. [153] less than 20 % in an Al-Mg-Si-Mn-based alloy). A summary of the DAS of individual casting method/alloy/area combinations and the corresponding calculated solidification rates V are summarized in Table 4.8.

Twin-roll cast and melt-spun materials have a profile of varying solidification rates through the as-cast materials. The observed DAS and calculated solidification rates for the twin-roll cast materials show results similar to studies by Grydin et al. [95] of Al-based alloys manufactured on the same twin-roll caster. Based on solidification lengths (distance between the last fully melted and the first fully solidified part of the strip) in the caster, the solidification rate was estimated at 4500 $\mathrm{K \cdot s^{-1}}$ at the surface and 2500 $\mathrm{K \cdot s^{-1}}$ in the center. However, Grydin modeled the process for higher casting speed and rolls covered with Cu shells. They have better heat conductivity (330 $\mathrm{W \cdot m^{-1} \cdot K^{-1}}$ [95]) than steel shells (20-60 $\mathrm{W \cdot m^{-1} \cdot K^{-1}}$ [154]). The differences in heat-conductivity of the shells explain the discrepancy between the calculated absolute values of solidification rates for our materials and the model estimated by Grydin.

Table 4.8 Solidification rates *V* for the individual materials and relevant Areas/Zones calculated from Equation 1.5.

Material	DAS [μm]	V [$K \cdot s^{-1}$]
MC	60 ± 10	(3.5 ± 0.4)
MCSc	82 ± 12	(1.5 ± 0.2)
T (Area 1)	6.5 ± 0.3	(3.1 ± 0.2).10^3
T (Area 2)	7.4 ± 0.5	(1.8 ± 0.2).10^3
T (Area 3)	9.4 ± 0.8	(1.0 ± 0.1).10^3
TSc (Area 1)	5.7 ± 0.8	(4.7 ± 0.6).10^3
TSc (Area 2)	7.8 ± 0.9	(2.1 ± 0.2).10^3
TSc (Area 3)	8.6 ± 0.6	(1.5 ± 0.1).10^3
MS (Zone 3)	0.6 ± 0.2	(4.3 ± 1.3).10^6
MSSc (Zone 3)	0.6 ± 0.1	(5.4 ± 0.7).10^6

The solidification rate profile in the melt-spun strips cannot be determined from DAS measurements alone due to a lack of dendritic solidification in Zone 2. Therefore, calculations according to Equation 1.9 are employed. The spread of solidification rates in the melt-spun materials is much higher than the one throughout the twin-roll cast strip, changing by two orders of magnitude from the surface to the thickest parts of the ribbon. Zone 2/Zone 3 transition thicknesses correspond to approximately 10^7 $K \cdot s^{-1}$ solidification rate (Figure 4.10).

An obvious issue with this model is that the solidification rate approaches infinity at the surface/roll interface. However, it provides reasonable results for thicknesses of tens of micrometers. We can compare the DAS model results with diffusion-based calculations by measuring the thickness at which the DAS measurement was performed in the equiaxed region (Table 4.9). Those results are visualized in Figure 4.10, and a good agreement is shown between the results of the two approaches.

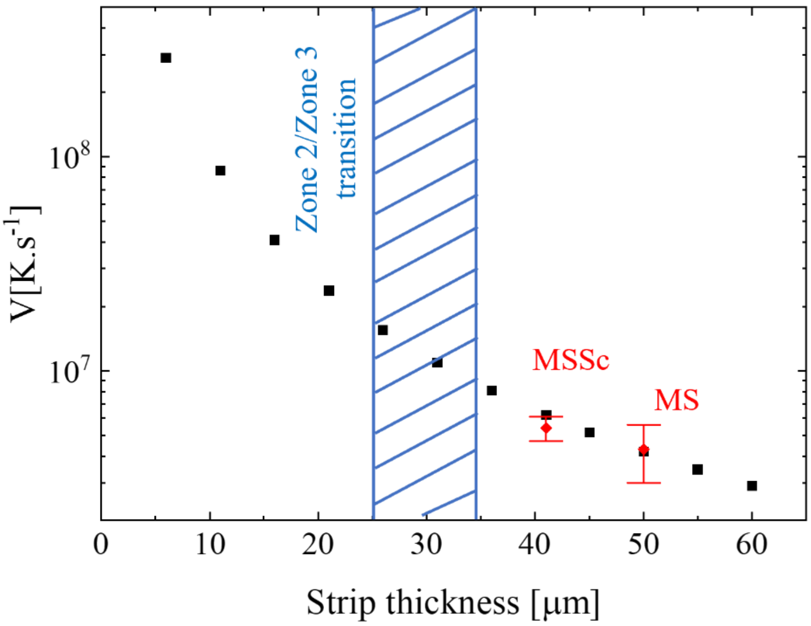

Figure 4.10 Local solidification rate from Equation 1.9 versus thickness of a melt-spun strip. The observed thicknesses of Zone 2/Zone 3 transition are highlighted in blue. The DAS-based solidification rate for Zone 3 of both MS and MSSc strip emphasized by a red color.

Table 4.9 Comparison of solidification rates calculated by the general power rule (Equation 1.5) and based on the one-dimensional thermal diffusion equation (Equation 1.9).

Material	DAS measurement thickness [µm]	DAS-based V [K·s^{-1}]	Diffusion based V [K·s^{-1}]
MS	50	$(4.3 \pm 1.3)x10^6$	$4.2x10^6$
MSSc	41	$(5.4 \pm 0.7)x10^6$	$6.2x10^6$

Grain structures

Heat is extracted evenly from all sides of the mold-cast ingot during cooling. In addition, no external forces are applied to the ingot during the solidification and cooling process, leading to an equiaxed structure. As-cast structures observed in our materials agree with those observed by Hekmat-Adrakhan et al. regarding primary phase size, grain sizes, and DAS [77].

TRC materials are partially rolled [81]. The rolling effect is more prevalent closer to the surface of the cast strip, leading to the formation of a gradient microstructure with elongated or columnar grains at the surface depending on the efficacy of heat transfer and applied forces and more equiaxed grains in the center [95,155].

Columnar grains in the melt-spun materials result from cellular crystallization and unidirectional heat transfer between the spinning roll and the solidified ribbon. Columnar grains are a feature of such a cooling mechanism regardless of the solidification rate. Flemings [156] states that such a mechanism is possible with a sufficiently high G_T/R_D ratio (Equation 1.4) thermal gradient at the solid/liquid interface and velocity of the dendrite tip/solidification interface). A high G/R ratio is reached by adding heat at one end and extracting it from the other.

The shift to equiaxed growth occurs with lower crystallization speed as more heat is extracted from the melt-spun ribbon/air interface further from the water-cooled roll at higher thicknesses, thus decreasing the G_T/R_D ratio. Additionally, the specific alloy composition affects the size of the columnar zone and the transition to equiaxed grains. EBSD results (Figure 4.7) show that the transition to columnar growth occurs consistently at comparable thicknesses for the studied alloys – around 30 µm. Since diffusionless solidification is associated with a high velocity of the solidification front, we can estimate this velocity based on the solidification time in Equation 1.8 for ribbon thickness between 25 and 35 µm. The corresponding solidification time is between 23 and 13 µs, and the solidification velocity is between 1.5 and 2.0 m·s^{-1} (Figure 4.11).

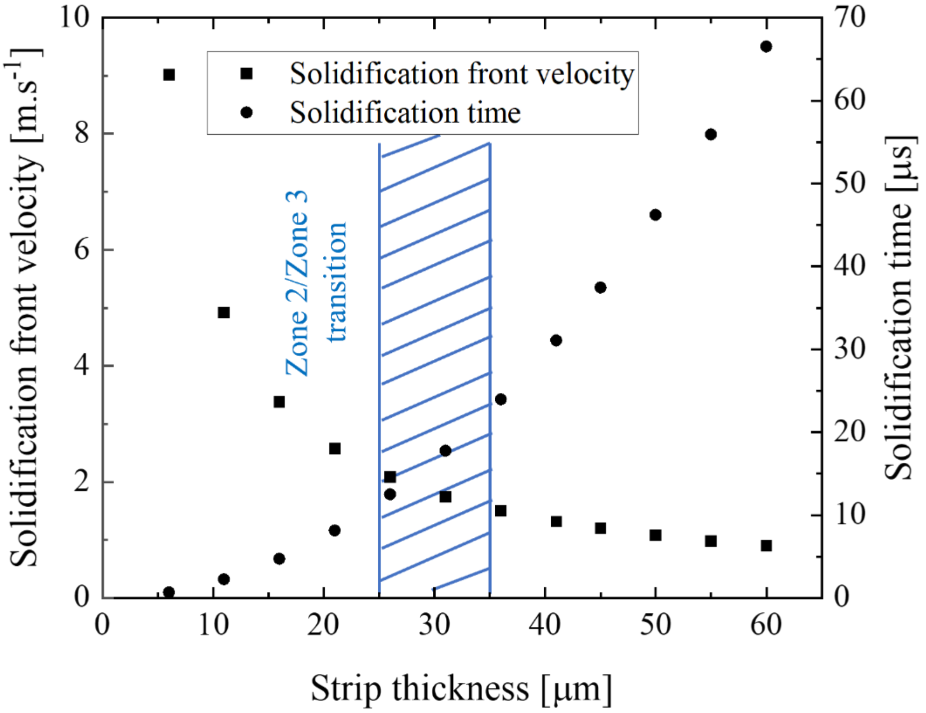

Figure 4.11 Local solidification front velocity and solidification time versus the thickness of a melt-spun strip. Thicknesses of Zone 2/Zone 3 transition highlighted in blue.

Primary phases, Cu concentration

Primary phase particles show substantial refinement with increasing solidification rate during casting, with particle size (characterized by the thickness of particles) decreasing three times between mold-cast and TRC materials and decreasing by an additional order of magnitude between the TRC and melt-spun materials. Sizes of primary precipitates in the mold-cast alloys are comparable to those observed in standard AA2195 DC-cast alloys by Hekmat-Ardakan et al. [77]. Similarly, early works on Al-Cu-Li-based TRC alloys by Li et al. [87] show comparable (around one micrometer) particle sizes and qualitatively similar primary phase distributions. Melt-spun materials contain coarser boundary phases and finer spherical precipitates inside the grains. The size of the boundary precipitates increases only slightly throughout the strip with (100 ± 30) nm width close to the surface/roll interface, to (140 ± 40) nm in the columnar and equiaxed parts of the strips.

On the other hand, the spherical precipitate size increases from (50 ± 7) nm at the surface/roll interface to (150 ± 40) nm in the columnar region – a size comparable to the boundary phases. The spherical phases are evenly distributed through the as-cast columnar grains. No spherical precipitates are inside grains in the equiaxed areas due to the dendritic growth segregating alloying elements to the eutectic cell boundaries and a low resulting driving force for precipitation inside the cells. Particle sizes across the different materials and their volume fractions are summarized in Table 4.7. Average values for both alloys are used for the plot in Figure 4.12 due to the difference between them being lower than the experimental scatter. The spherical particle diameter is used to characterize zones 1 and 2 of the melt-spun strips (Figure 4.8 (b,c,f,g)) to study the variance of primary phase size with the high cooling rates in these zones.

Studies on rapidly solidified Al-Cu-Li-Mg-Zr-based materials imply that the boundary phases are the same structure as those with lower solidification and cooling rates [79,157,158]. EDS analyses imply the presence of the binary θ(Al_2Cu) phase in the case of both the boundary phases and the spherical precipitates. Increased Fe content compared to the surrounding matrix implies the formation of the Al_7Cu_2Fe phase. The presence of the Al_7Cu_2Fe phase is also confirmed in particles B4, B6, and A5 (Figure 4.8 (a,e), Figure 4.9 (a)). The higher Fe content in the TEM analyses directly results from the lower contribution of the surrounding matrix, which has a low Fe concentration. Mg content in the analyzed phases never exceeds the average values for the surrounding matrix, which implies a lack of formation of Mg-containing primary phases.

The relationship between the cooling rate of the alloys and Cu concentration in the matrix is highly nonlinear. The MC alloys have Cu concentrations in the matrix around 0.8 wt. % for both alloys, which is still substantially higher than the equilibrium solubility limit - 0.35 wt. % for Cu in Al [159] Such concentrations are relatively common even in standard direct-chill cast materials, as evidenced by Wang et al. [157], who observed around a third of the Cu content in the supersaturated matrix. The Cu concentration does not substantially increase by increasing the cooling rate to the levels of TRC with around 1.0 wt.% in both TRC materials. This concentration is comparable to the results obtained by Li et al. [87]. Dendritic regions of the melt-spun alloys contain slightly higher concentrations of Cu – 1.2 wt. % and 1.4 wt. % for the MS and MSSc materials, respectively. Gianogolio et al. [160] report similar Cu concentration changes in their study of atomized particles formed with solidification rates between 10^2 K·s^{-1} and 10^5 K·s^{-1}. They measured a variance in Cu concentration from 1.1 wt. % to 1.4 wt. % in an alloy containing 2.4 wt. % Cu.

Increasing the solidification rate beyond 10^7 K·s^{-1} introduces a shift in the solidification mode, causing a sharp increase in the matrix solute concentration (Figure 4.12). Due to this sharp change, the dendritic solidification regime results, like the DAS and grain size relations, cannot extrapolate solidification rates to the columnar and featureless regions of the melt-spun strips.

Power laws similar to those in Equation 1.5 can be defined for the remaining studied parameters. These power laws are defined as:

$$X = C_x V^{-j_x} \tag{4.3}$$

C_x and j_x are material-dependent constants for each studied parameter x, where x is *w*, *f*, or Cu concentration. The determined constants are summarized in Table 4.10.

A graph characterizing particle parameters – width and volume fractions, and Cu concentration in the matrix is shown in Figure 4.12. A single average value of Cu concentration is used for the plot for both alloys and the three studied TRC areas due to the difference between individual values being lower than the measurement scatter. The solidification rate for zones 1 and 2 of the melt-spun alloys are set as $3\cdot10^8$ K·s^{-1} and $2\cdot10^7$ K·s$^{-1,}$ in agreement with the plot in Figure 4.10. For the comparison, particle sizes and Cu concentrations from selected works are shown in the same graph. Particle sizes and volume fractions follow the power law within the experimental scatter for the entire range of cooling rates. Cu concentrations of Gianoglio et al. [160] are consistently higher by approximately 0.2 wt. % but rise with increasing solidification rates at a similar rate.

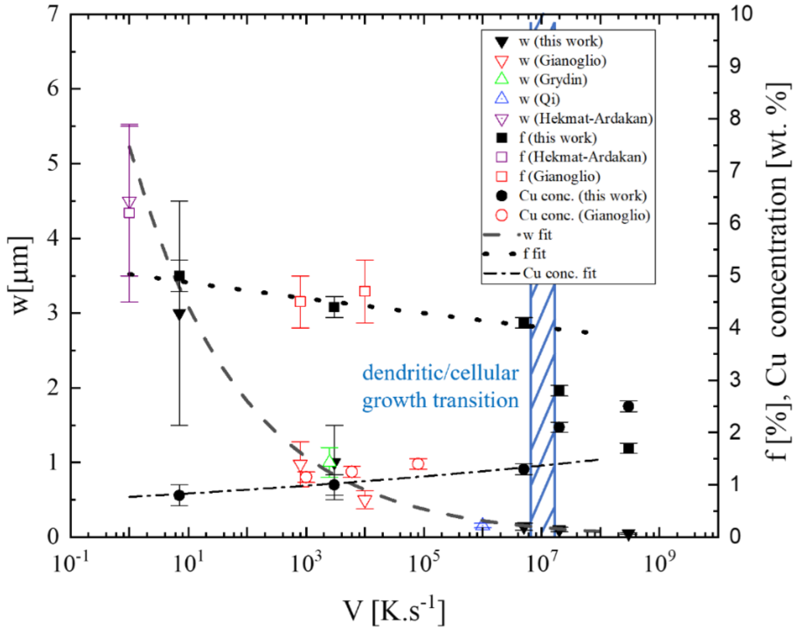

Figure 4.12 Variance of particle size, Cu solute concentration, and primary phase volume fraction with cooling rate (full symbols). Fitting of points measured in this work by a general power law (Equation 4.3). Data extracted from the literature (empty symbols). Solidification rates corresponding to the transition between dendritic and cellular growth highlighted in blue.

Table 4.10 Constants C_x and j_x from Equation 4.3 for the microstructural parameters – particle width w, particle volume fraction f, and Cu concentration.

x	C_X	j_X
w	5.2	0.23
f_V	5.0	0.014
Cu conc.	0.8	0.036

Cu concentration and volume fraction of primary phase particles have an opposite trend with a sharp change in the columnar part of the melt-spun strips. A change in volume fraction is related to a change in Cu concentration in the matrix. The stochiometric θ phase contains 1/3 Cu, meaning that 1/3 of the measured volume fractions of primary phases comprises Cu atoms. This estimate works under two assumptions – all primary phase particles are θ(Al_2Cu) phases, and differences between unit cell volumes of θ and the Al matrix are neglected. However, this rough estimate results in as much as 1.6 at. % of Cu, while both materials contain only 1.1 at. % Cu in total. Sarreal and Abbaschian [161] showed that the θ phase could contain less than 0.5 of the stochiometric Cu content, which resolves the discrepancy between the measured volume fraction of the θ(Al_2Cu) phase and Cu matrix concentration.

4.1.5. As-cast states summary – homogenization

The size of eutectic cells is pivotal for homogenization and solution treatment. The most straightforward estimate for homogenization can be done by calculating diffusion length [2]:

$$L = 2\sqrt{Dt}\,. \tag{4.4}$$

L is the diffusion length, D is the diffusion coefficient, and t is time.

Diffusion calculations are further improved in a study by Zhang et al. [162]. They suggest a relation between homogenization temperature T, homogenization holding time t, and the cell size (ECS):

$$\frac{1}{T} = \frac{R}{Q}\ln\left(\frac{4\pi D_0 t}{4.6 ECS^2}\right), \tag{4.5}$$

where R is the gas constant (8.314 $J \cdot K^{-1} \cdot mol^{-1}$), and Q is the diffusion activation energy (136.8 $kJ \cdot mol^{-1}$ for Cu [130]). D_0 is the diffusion constant in the general temperature-dependent Arrhenius equation for diffusion. Cu has the lowest diffusion coefficient (D_0[Cu] = 0.084 $cm^2 \cdot s^{-1}$ [130]) of the main strengthening particle-forming elements in the alloy (Cu, Mg, Li). Therefore, we assume that the homogenization of Cu also ensures the homogenization of the other elements.

Rewriting the homogenization equation for holding time t, we obtain

$$t = \frac{4.6ECS^2}{4\pi D_0}\exp\left(\frac{Q}{RT}\right). \tag{4.6}$$

Homogenization time is directly proportional to the second power of DAS. Lowering eutectic cell size by an order of magnitude implies the possibility of a reduction of holding time by two orders of magnitude. Crucial for an intended combined homogenization/solution treatment of the twin-roll cast and melt-spun materials is the homogenization of already soluted Cu and other elements and the transformation and dissolution of preexisting primary phases. The homogenization holding times calculated through Equation 4.6 and corresponding diffusion lengths (Equation 4.4) are summarized in Table 4.11. Figure 4.13 shows the relation between homogenization holding time, the maximal possible ECS at 530 °C, and diffusion lengths for demonstrating a considerable role of slight variation of homogenization temperature.

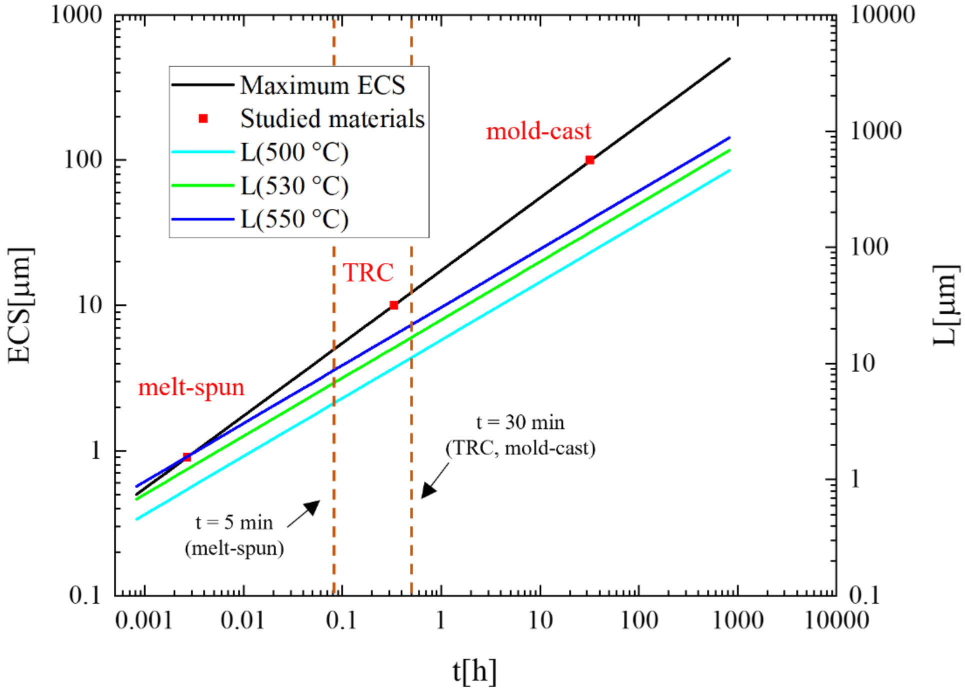

Figure 4.13 Relation between homogenization time and the maximal corresponding ECS (Equation 4.5). Three casting methods highlighted in red. Diffusion lengths (Equation 4.4) for different temperatures. Homogenization holding times used in the study highlighted by dashed lines.

Table 4.11 Calculated homogenization intervals and corresponding diffusion lengths at 530 °C.

Casting method	mold-casting	twin-roll casting	melt-spinning
t	32 h	25 min	10 s
L [µm]	136	15	1.4

4.2. In-situ electron microscopy experiments

In-situ annealing experiments were performed to map the kinetics of processes occurring during the treatment of the materials at elevated temperatures. The experiments comprise in-situ annealing in TEM to directly observe structural changes in a temperature interval between room temperature and 550 °C with a stepwise effective heating rate (50 °C/20 min). The distributions of solutes in the initial and final states were mapped by EDS analysis (TEM in TRC and melt-spun materials, SEM in mold-cast materials).

4.2.1. Mold-cast materials

The size of the eutectic cells in the mold-cast materials is large and cannot be viewed at standard TEM magnifications. For this reason, a low-magnification STEM mode was employed for the in-situ experiment combined with a BSE detector. Since EDS mapping is not possible in this regime (high intensity, high temperature), the EDS maps of the initial state (Figure 4.14) were taken in standard SEM on the TEM sample used for in-situ TEM heating. The area selected for EDS mapping contains mostly Al_2Cu phases and several Al_7Cu_2Fe phases. Variance in Cu contrast can be observed in the MCSc around boundaries of eutectic cells, implying a Cu-rich zone approximately 10 µm wide (Figure 4.14 (g), white arrows). Red rectangles highlight the areas of EDS analyses in Figure 4.15.

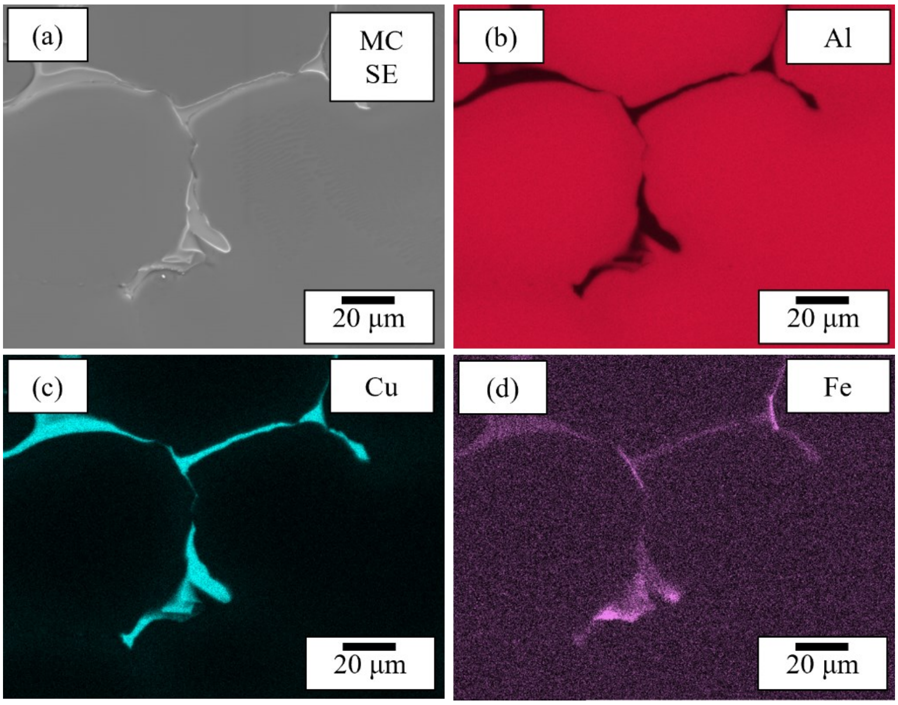

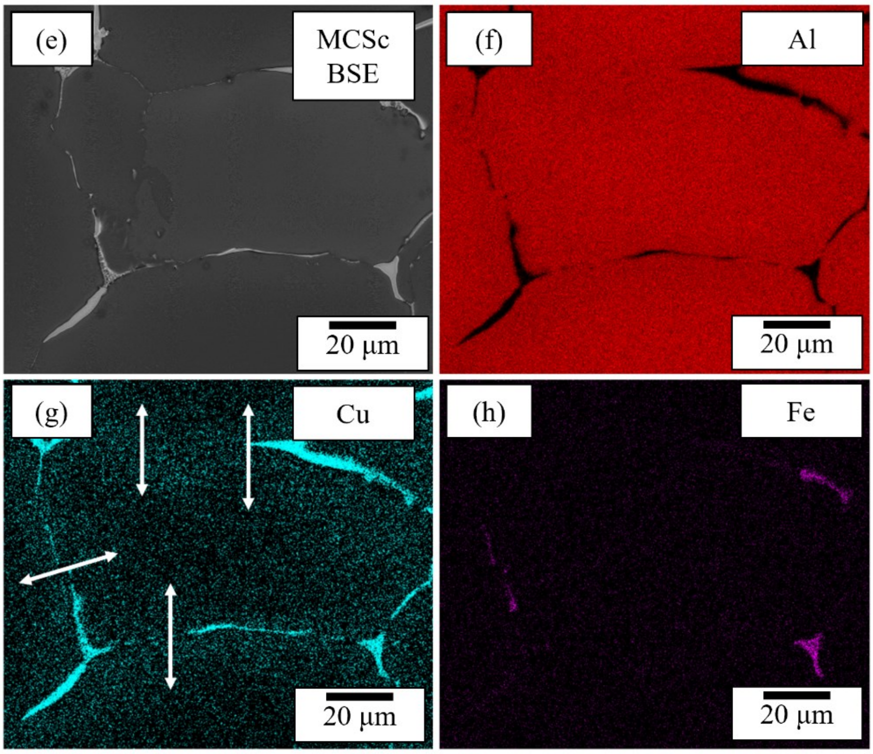

Figure 4.14 EDS maps of sections of the areas selected for in-situ STEM heating of the mold-cast materials. BSE and SE contrast images in SEM (a,e) and corresponding Al (b,f), Cu (c,g), and Fe (d,h) maps. White arrows (g) highlighting the Cu segregation close to eutectic cell boundaries.

First detectable microstructural changes occur in both materials at 500 °C (yellow ovals in Figure 4.15 (c), (g)). A more intensive dissolution of primary phase particles occurs above this temperature (Figure 4.15 (d), (h)).

The specimen was then cooled in-situ in the TEM with the cooling rate approaching 200 K·min^{-1}. However, this cooling rate does not assure full preservation of the final structure observed in the in-situ experiment (Figure 4.15 (d), (h)), and reprecipitation of new Cu-rich particles in the vicinity of the eutectic cell boundaries occurs. The width of this area clearly shows that Cu is not redistributed uniformly across the whole cell during the relatively short period of 30 min above 500 °C. Only Fe-rich Al_7Cu_2Fe particles remain after the annealing experiment at the eutectic cell boundaries (Figure 4.16).

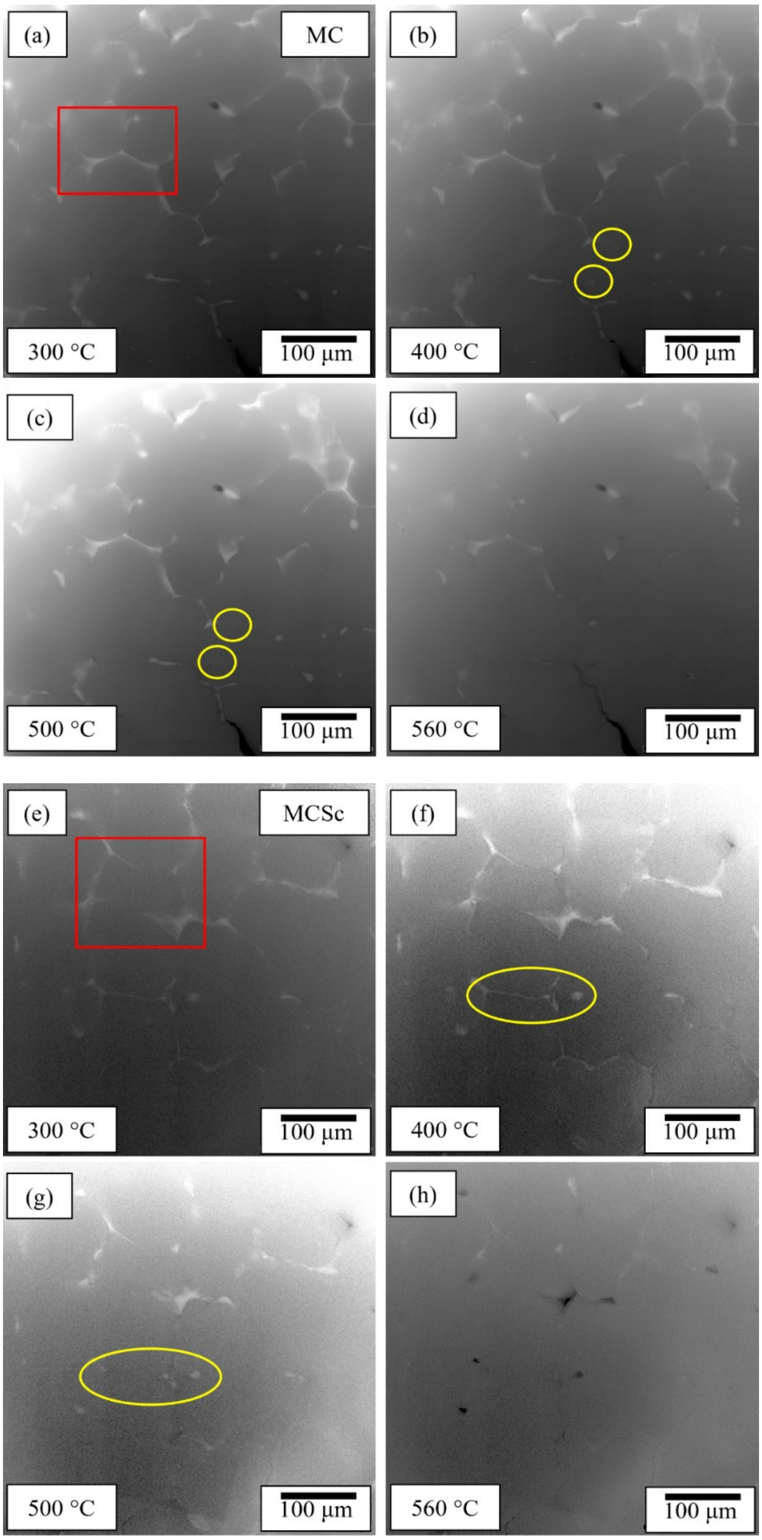

Figure 4.15 BSE contrast STEM images of the microstructural evolution of primary phase precipitates during in-situ annealing of the MC (a-d) and MCSc (e-h) materials. Annealing in a stepwise 50 °C/20 min regime. Area for EDS mapping highlighted in red. Areas of initial phase changes highlighted in yellow.

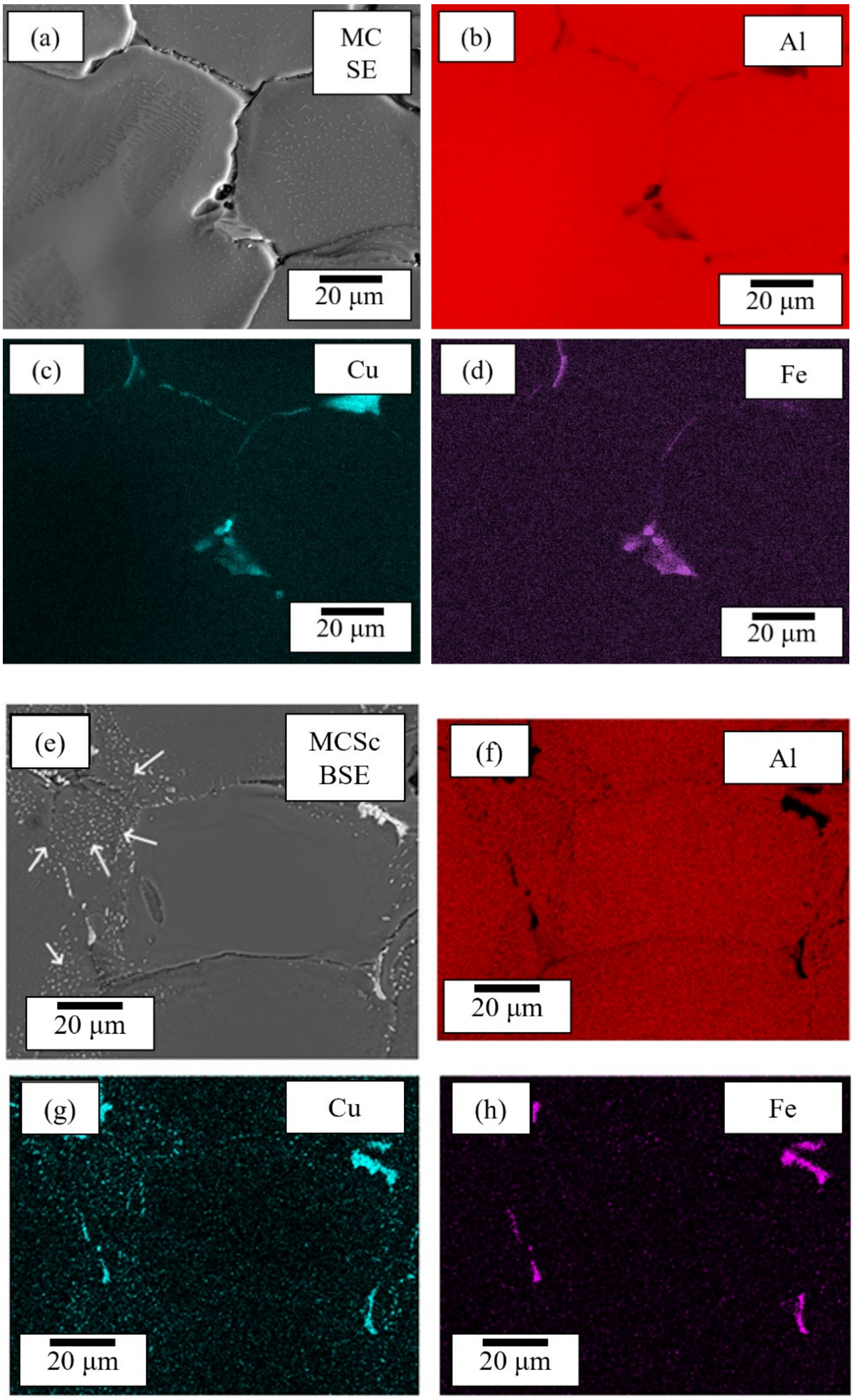

Figure 4.16 EDS mapping of the areas selected for in-situ STEM annealing after the experiment and in-situ cooling. BSE and SE micrographs of the analyzed area (a,e) and EDS maps of Al (b,f), Cu (c,g), and Fe (d,h) of the same area. White arrows highlighting the reprecipitation near eutectic cell boundaries (e).

4.2.2. Twin-roll cast materials

The size of eutectic cells is significantly smaller in the TRC materials, and the clear Cu gradient observed in the initial state of the MCSc material is not present (Figure

4.17). Modulated contrast in the DF STEM images and the Al EDS maps is an artifact reflecting thickness modifications due to inhomogeneous electrolytic polishing of the specimen near the primary phase particles. The boundary primary particles are the Al_2Cu, Al_7Cu_2Fe, and the Al_2CuMg phase in areas with increased Mg contrast in the EDS maps (Figure 4.17 (e),(j)).

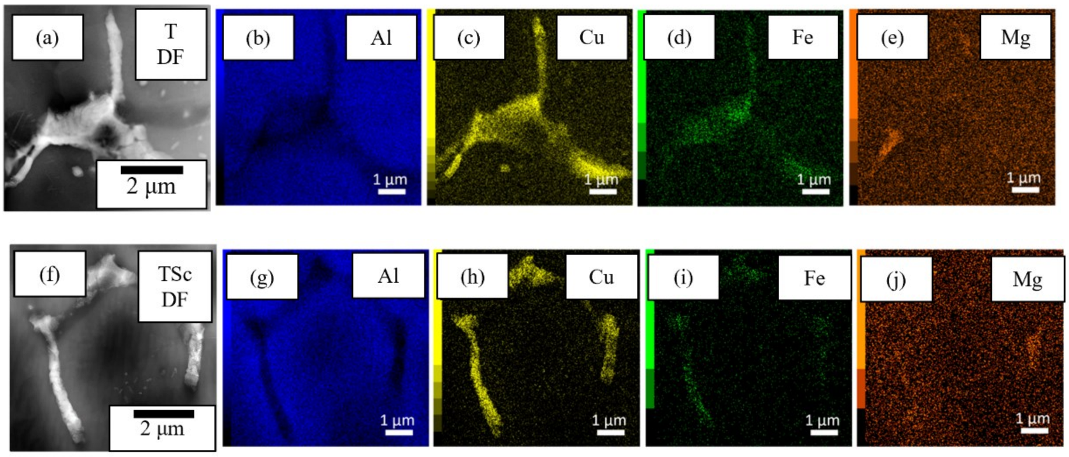

Figure 4.17 STEM EDS analysis of the TRC materials in areas selected for the in-situ annealing experiments. HAADF STEM micrograph of the observed areas (a,f). Corresponding Al (b,g), Cu (c,h), Fe (d,i), and Mg (e,j) maps.

The in-situ heating experiments confirm the precipitation of coarse nanoscale particles common for this system [106,134] in the originally particle-free matrix already at 300 °C (Figure 4.18 (b),(h)). Segmentation of the primary phases occurs at 400 °C together with the ripening of matrix precipitates into rounded particles (Figure 4.18 (c), (i)). A part of modified primary phases and all matrix particles dissolve above 450 °C (Figure 4.18 (d), (j)). The remaining primary phases do not dissolve even at the highest annealing temperatures, and only their further spheroidization occurs (Figure 4.18 (e), (k), (f), (l)). EDS analysis confirms that all remaining particles are the complex Al_7Cu_2Fe phase (Figure 4.19). The coarse Cu-rich particle in Figure 4.19 (f), (h) (highlighted by a red arrow) is the Al_2Cu, which dissolves above 500 °C (Figure 4.18 (l)). The homogeneous reprecipitation of Cu-rich particles inside the original eutectic cells (Figure 4.19 (a), (f)) confirms a successful homogenization during the in-situ experiment.

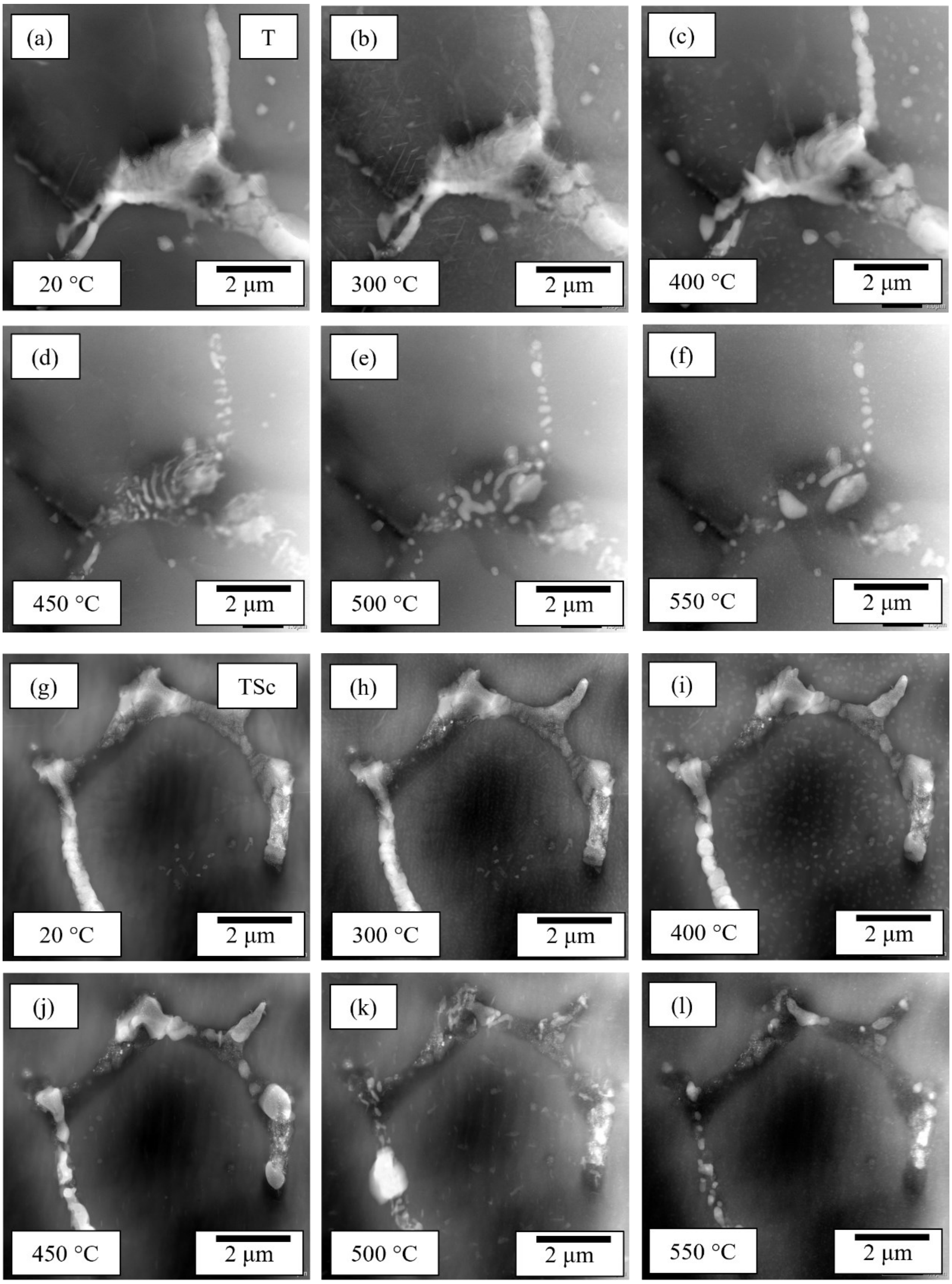

Figure 4.18 Phase distribution evolution in eutectic cells during stepwise (50 °C/20 min) annealing. HAADF STEM micrographs of the T (a-f) and TSc (g-l) materials.

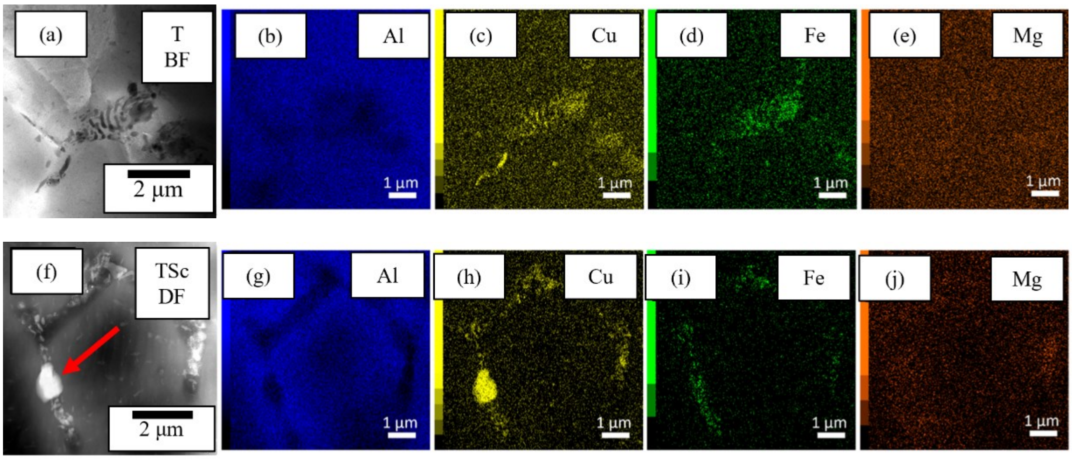

Figure 4.19 EDS mapping of the areas from Figure 4.18. HAADF micrograph of the analyzed regions (a,f). Corresponding element distribution maps: Al (b,g), Cu (c,h), Fe (d,i), Mg (e,j) after cooling from 560 °C (a-e) and 500 °C (f-j). Red arrow highlighting the Cu-rich particle (f).

4.2.3. Melt-spun materials

The melt-spun materials contain complex spherical Al_7Cu_2Fe precipitates in grain interiors and rod-shaped Al_2Cu and Al_7Cu_2Fe at cell boundaries (Figure 4.20). The melt-spun specimens are prone to accidental damage. Therefore, EDS analyses are performed in different areas than the in-situ experiments. Precipitation of nanoscale precipitates, their coarsening, and the final dissolution of newly formed matrix particles occurs below 450 °C (Figure 4.21 (b-d), (h-j)). The matrix primary phase particles and boundary phases grow and coagulate on grain boundaries below 450 °C. The majority of them dissolve at the highest annealing temperatures, leaving only a dispersion of coarse Fe and Cu-rich (mostly Al_7Cu_2Fe) particles (Figure 4.21 (f), (l); Figure 4.22). Reprecipitation occurs in the in-situ cooled specimen (Figure 4.22 (a,d)). Similarly to the TRC materials, it occurs evenly across the grains.

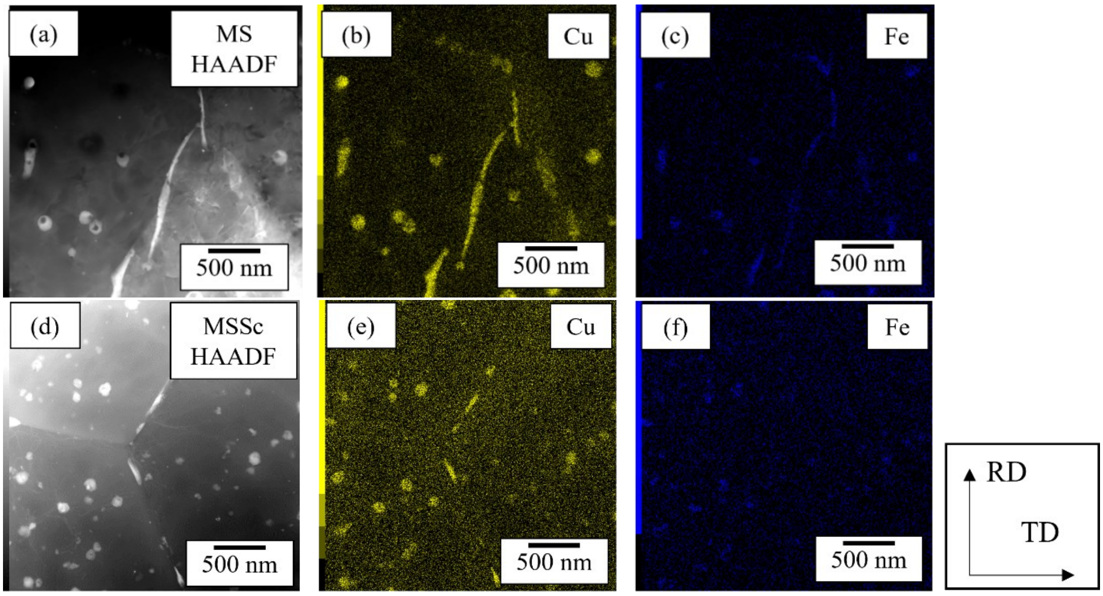

Figure 4.20 EDS analysis of areas in the melt-spun materials specimen before in-situ annealing. HAADF micrographs of the analyzed sections (a,d) and corresponding Cu (b,e) and Fe (c,f) maps.

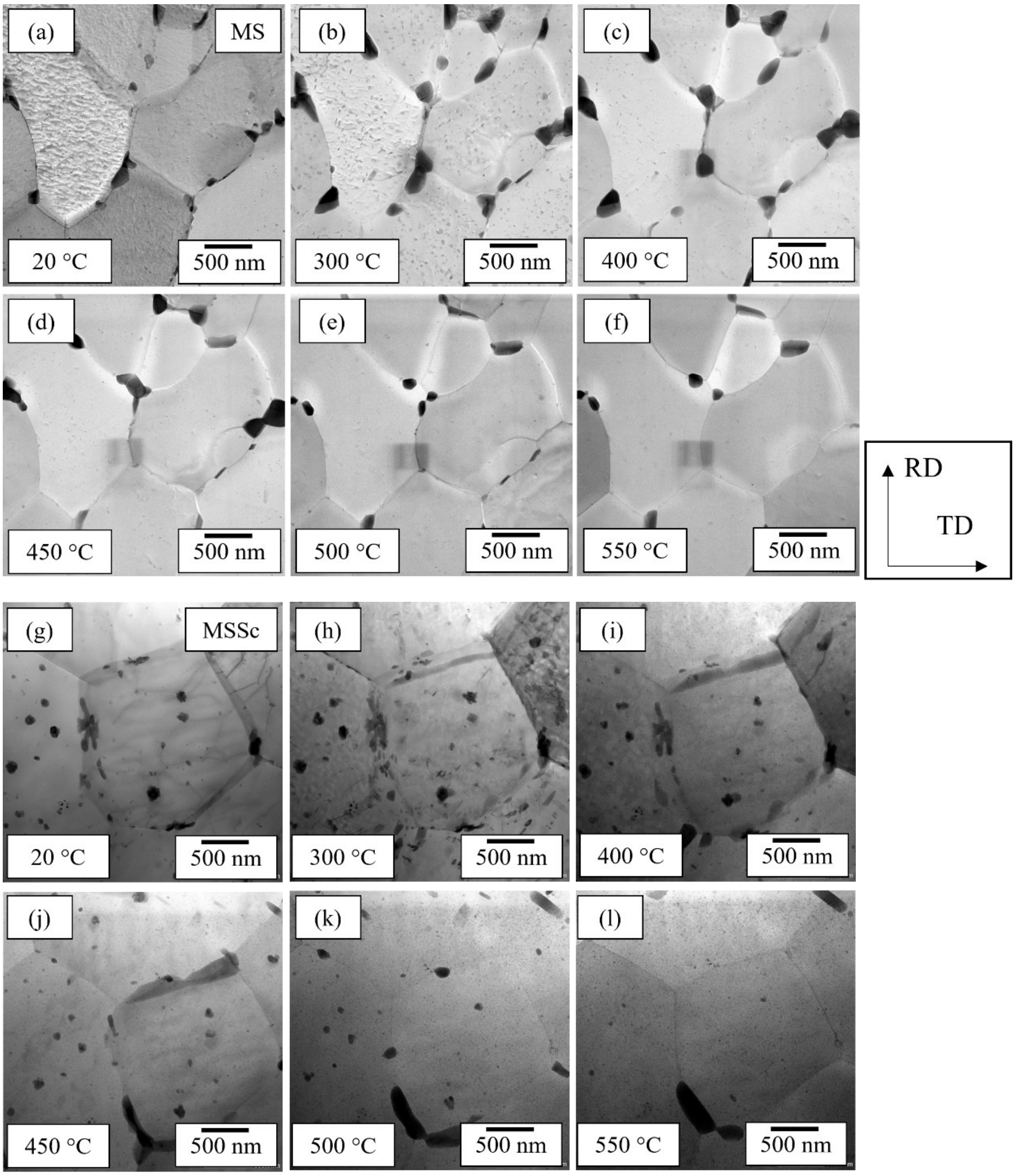

Figure 4.21 Evolution of primary phase particles in the MS (a-e) and MSSc materials (g-l) during in-situ annealing with the step-wise annealing regime 50 °C/20 min. STEM BF images.

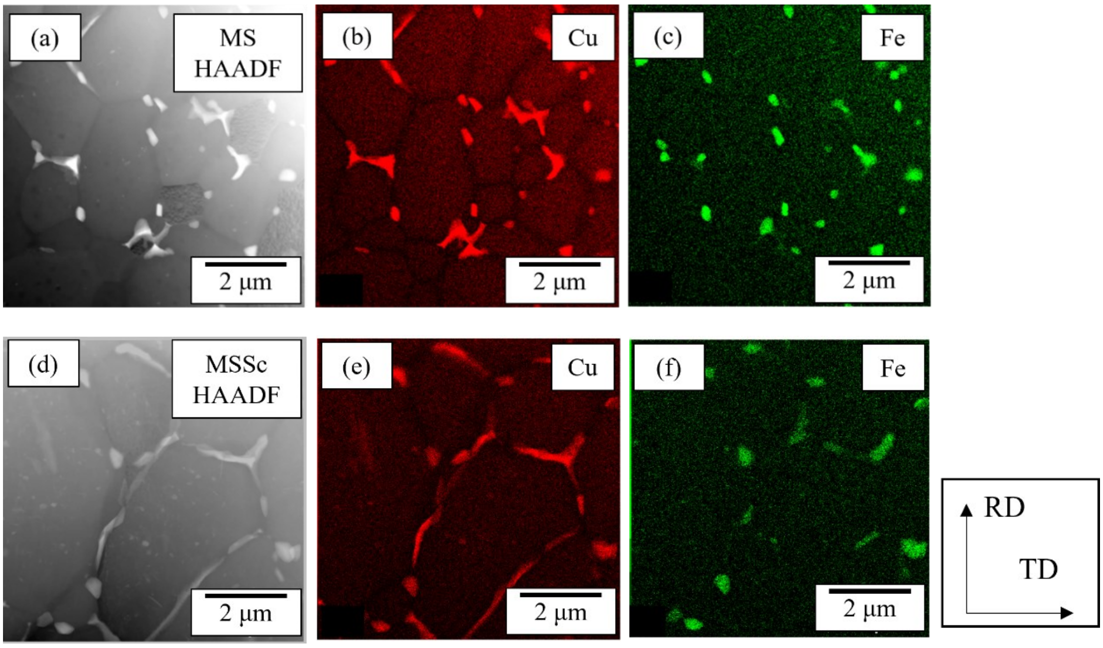

Figure 4.22 EDS analysis of the melt-spun materials after in-situ heating to 560 °C and cooling to room temperature. HAADF micrographs of the analyzed areas (a,d) and corresponding Cu (b,e) and Fe (c,f) maps.

4.3. Standardized states

A combined heat treatment consisting of three annealing steps at 300 °C, 450 °C, and 530 °C followed by quenching into water at room temperature is proposed. The two lower temperatures reflect the conditions for precipitation of grain refining Al$_3$(Sc,Zr) dispersoids optimized in previous studies on Al-Mg-based alloys [163]. The final annealing step serves as a combined homogenization/solution treatment optimized for TRC materials to limit the adverse effects of coarse particles and maximize the solute content of the main alloying elements. The holding time of each step is limited to 30 min (5 min in melt-spun materials) to limit surface Li depletion and Al$_3$(Sc,Zr) coarsening.

The formation of standard Al-Cu-Li-Mg-Zr-based materials from large-scale ingots includes several rolling steps, extrusion, or forging. This processing induces grain refinement, subgrain structure formation, and texture changes. SPD steps are inserted between the 450 °C/30 min and 530 °C/30 min annealing steps to facilitate similar refinement in the mold-cast and twin-roll cast materials. Two methods are implemented. The first is symmetrical or asymmetrical rolling, and the second is CGP. These methods differ in modes of deformation from pure shear (CGP) to rolling with partial shearing (AR) and pure rolling (SR). Some samples were standardized without a deformation step to establish the role of the individual deformation methods.

Apart from primary phase dissolution and homogenization of alloying elements, the high-temperature combined homogenization/solution treatment during the final annealing step can induce recovery, recrystallization, or grain growth. The final grain size, morphology, homogeneity of their size distribution, and texture strongly impact the mechanical properties after the final processing.

4.3.1. Formation of strengthening Al_3Zr and $Al_3(Sc,Zr)$ dispersoids

TEM observations confirm the presence of Al_3Zr (red circles in Figure 4.23 (a-c)) and $Al_3(Sc,Zr)$ (Figure 4.23 (d-f)) dispersoids in the standardized materials. Differences in contrast across the individual $Al_3(Sc,Zr)$ precipitates indicate a successful formation of the core-shell structure [56] (Figure 4.23 (e,f)). The ternary precipitates are coarser than the binary Al_3Zr phases, but their size is still below the coherency limit (Table 4.12) [120]. Sizes of the individual types of precipitates are consistent across the materials. The core-shell structure was also confirmed by EDS (Figure 4.24).

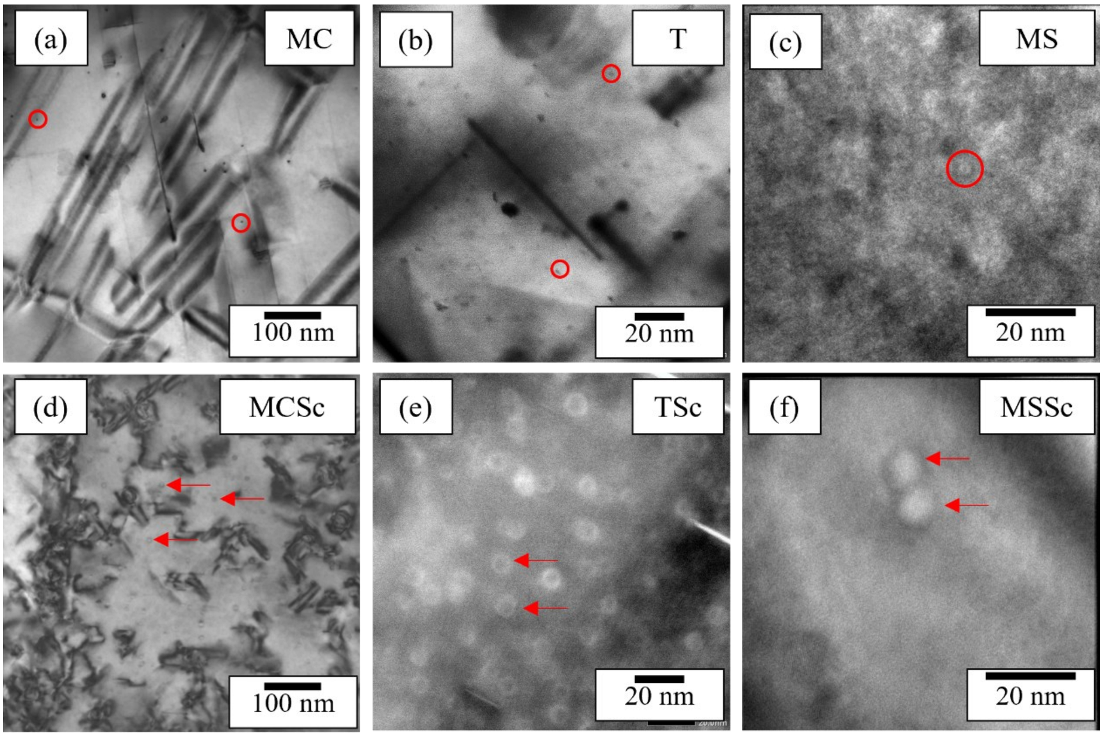

Figure 4.23 BF TEM (a,c,d,f), BF STEM (b), and HAADF STEM (e) micrographs of the nanoscale grain refining precipitates in the standardized MC (a), T (b), MS (c), MCSc (d), TSc (e), and MSSc (f) materials. Red circles indicate the locations of the Al_3Zr precipitates, and red arrows highlight the locations of $Al_3(Sc,Zr)$ dispersoids.

Table 4.12 Diameters of the grain refining dispersoids.

Material	Al_3Sc/$Al_3(Sc,Zr)$ size [nm]
MC	2.3 ± 0.5
MCSc	9 ± 1
T	2.4 ± 0.7
TSc	9 ± 1
MS	2.0 ± 0.4
MSSc	10 ± 2

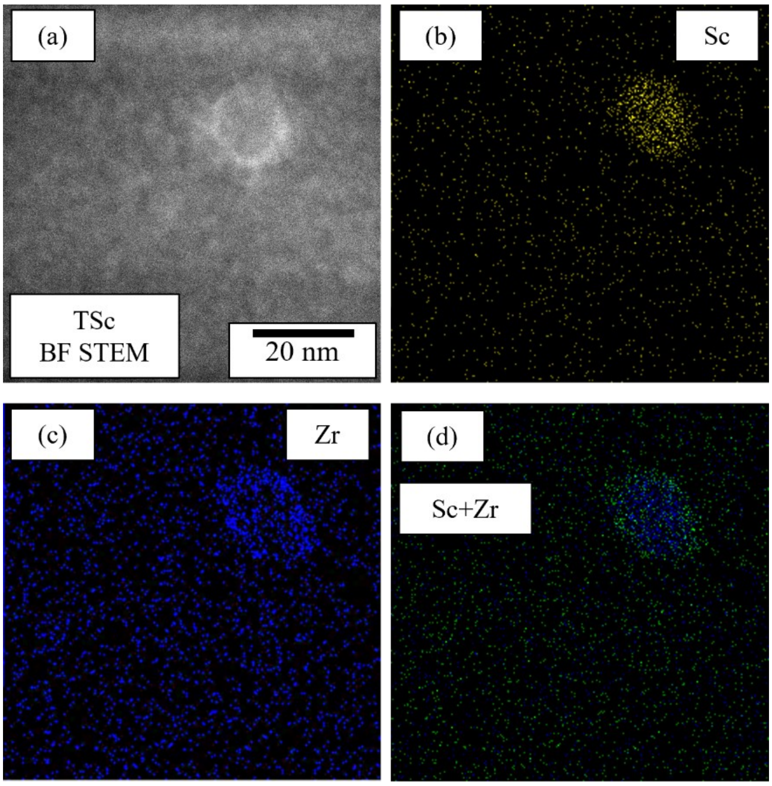

Figure 4.24 EDS elemental mapping of an $Al_3(Sc,Zr)$ phase in a standardized TSc material. BF STEM micrograph of the particle (a), Sc (b), and Zr (c) concentration maps. Overlay image of Sc + Zr (d).

4.3.2. Distribution of alloying elements in standardized materials

As predicted by the diffusion models, optimal homogenization is not achieved in the mold-cast material due to the short exposition to homogenization temperatures. The BSE contrast (red lines in Figure 4.25 (a)) and EDS Cu mapping (Figure 4.26 (c),(h), Table 4.13) indicate the presence of Cu-rich primary phases on cell boundaries and only partial diffusion of Cu further into the cell interiors. The Cu concentration in the centers of eutectic cells remains low (Table 4.14).

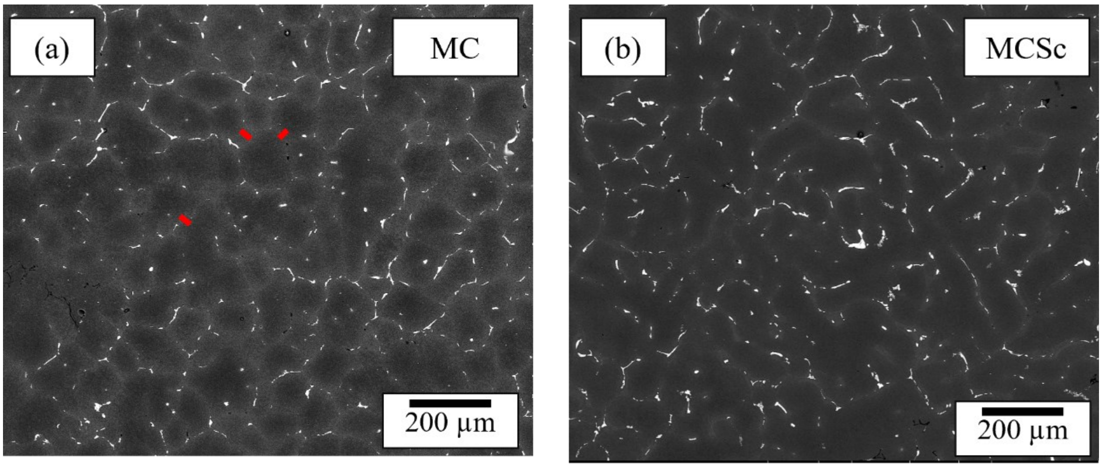

Figure 4.25 BSE contrast micrographs of the standardized MC (a) and MCSc (b) materials. Red lines highlighting high Cu content areas.

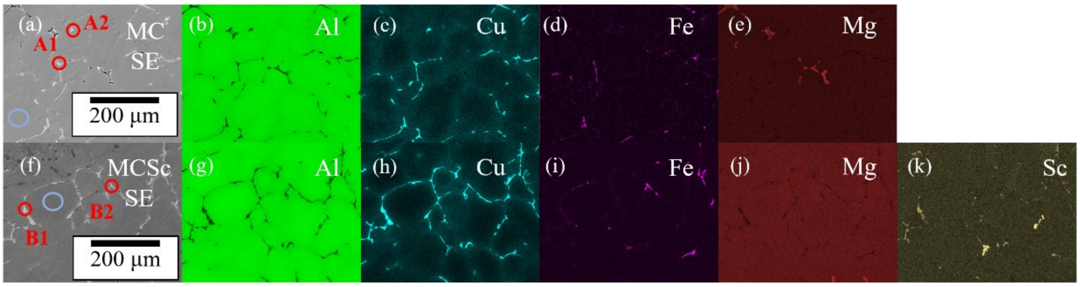

Figure 4.26 EDS mapping of the standardized MC (a-e) and MCSc (f-k) materials. SE contrast micrographs of the selected areas (a,f), Al maps (b,g), Cu maps (c,h), Fe maps (e,j), and Mg maps (e,j) for both materials. Sc map (k) for the MCSc materials. Selected particles for point analyses of particles (A1, A2, B1, B2). Blue ovals highlighting matrix concentrations of alloying elements.

Table 4.13 EDS analyses in areas highlighted in Figure 4.26 in wt. %.

	Cu	Fe	Mg	Sc
A1	31.4	0.6	1.4	-
A2	19.5	0.2	1.2	-
MC matrix	1.1	0.1	1.0	-
B1	45.8	0.1	1.5	1.6
B2	16.2	7.2	1.2	0.2
MCSc matrix	1.1	0.1	0.9	0.5

Table 4.14 Primary phase volume fractions and matrix Cu concentrations.

Material	f_V [%]	Cu concentration [wt. %]
MC	3.2 ± 0.4	0.8 ± 0.1
MCSc	3.5 ± 0.3	0.9 ± 0.2

Particles of primary phases in twin-roll cast materials mostly dissolve (Figure 4.27), and the remaining particles are spheroidized complex Al_7Cu_2Fe phases (Figure 4.28). The majority of Cu and all Mg are homogeneously distributed across the eutectic cells, as predicted by diffusion models (Table 4.15), except for Zone 2 (Figure 4.27 (b),(d), Figure 4.28 (a),(f)), which might contain central segregation in the as-cast state. Nevertheless, central segregation can be suppressed by optimization of TRC conditions. Sc contrast is a parasitic background effect. Point analyses do not confirm any increased concentration of Sc in the particles compared to concentrations in the surrounding matrix (Table 4.16).

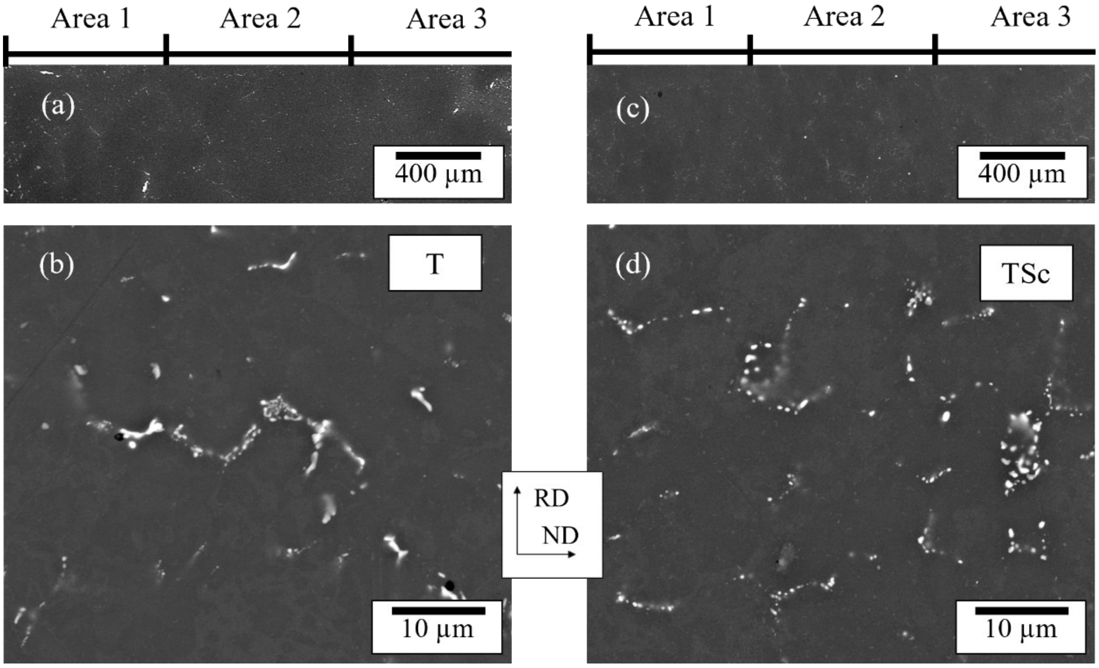

Figure 4.27 BSE contrast micrographs of the standardized T (a,b) and TSc (c,d) materials. Overview images of the three studied Areas (a,c) and higher magnification images from Area 2 (b,d).

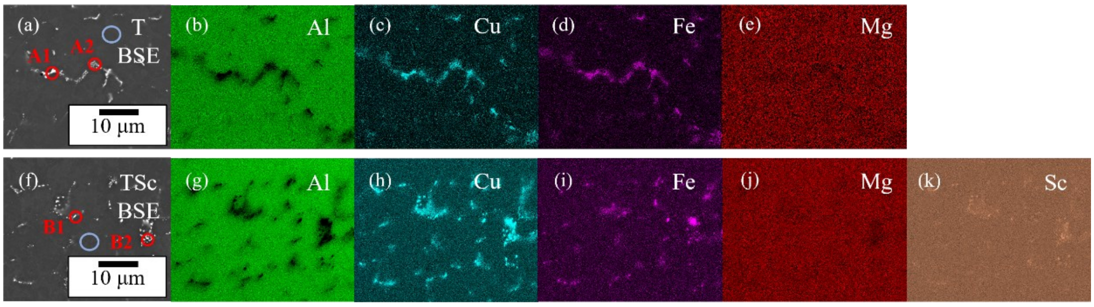

Figure 4.28 EDS mapping of standardized T (a-e) and TSc (f-k) materials. BSE contrast micrographs of the mapped areas (a,f). Al (b,g), Cu (c,h), Fe (d,i), and Mg maps (e,j) of both alloys. Sc map (k) of the TSc material. Mapping performed in Area 2 of the TRC strips. Selected particles for point analyses (A1,A2,B1,B2) in red circles. Blue ovals highlighting areas of matrix concentration measurements.

Table 4.15 Transformed primary phase volume fractions and matrix Cu concentrations extracted from Figure 4.27.

Material	f_V [%]	Cu concentration [wt. %]
T	2.3 ± 0.2	1.5 ± 0.1
TSc	2.2 ± 0.3	1.6 ± 0.1

Table 4.16 EDS point analyses from areas and particles highlighted in Figure 4.28. Concentrations in wt. %.

	Cu	Fe	Mg	Sc
A1	7.5	2.3	0.9	-
A2	5.2	1.7	1	-
T matrix	1.4	0.1	1	-
B1	3.8	0.3	0.9	0.3
B2	4.7	1.5	0.8	0.2
TSc matrix	1.5	0.1	1.1	0.3

The remaining transformed primary phase particles in melt-spun materials are primarily Al_7Cu_2Fe in accordance with the in-situ heating experiments and EDS analyses. These phases are distributed mainly at grain boundaries (Figure 4.29). Detailed EDS analysis (Figure 4.30) showed additional coarse pure Cu particles. These are likely present as an artifact of an interaction of the strips with the Cu roll during casting or contamination of the melting crucible. Initially, easily distinguishable boundaries between the Zones were no longer apparent. Matrix Cu concentration increases in Zone 3 compared to the as-cast material. Matrix Cu concentration is the same within the error across the thickness of the strip after standardization (Table 4.17).

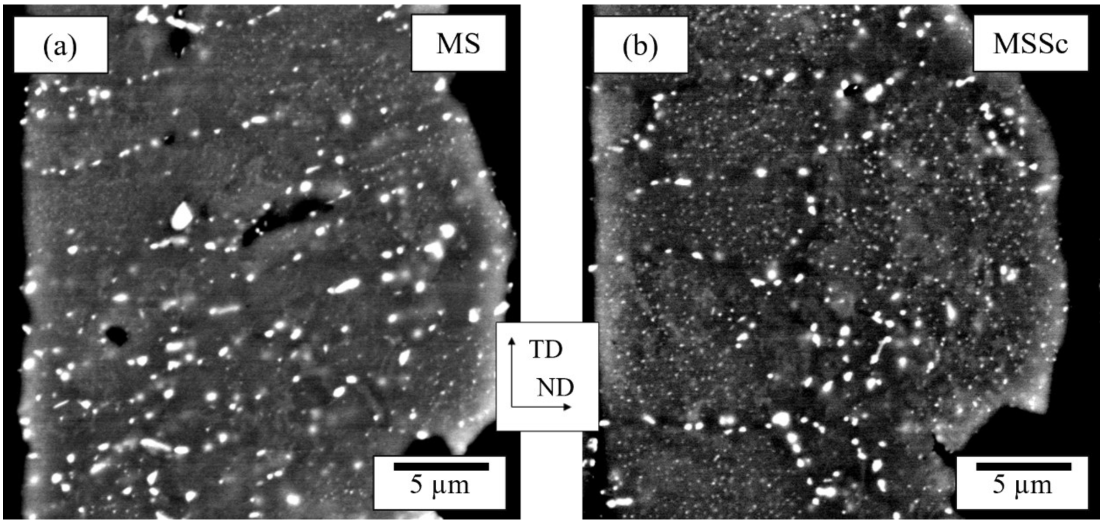

Figure 4.29 BSE contrast micrographs of the standardized MS (a) and MSSc (b) materials.

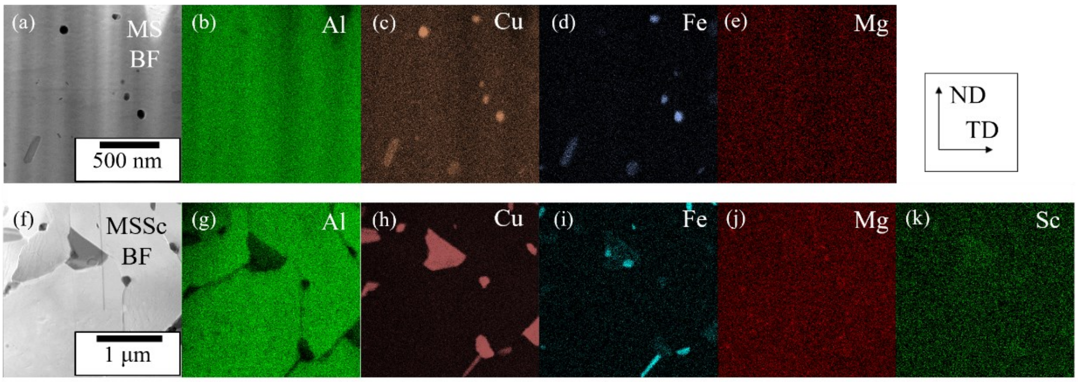

Figure 4.30 EDS mapping of standardized MS (a-e) and MSSc (f-k) materials. BF (a,f), Al (b,g), Cu (c,h), Fe (d,i), and Mg (e,j) maps of both alloys. Sc distribution map (k) in the MSSc material.

Table 4.17 Transformed primary phase particle volume fractions and matrix Cu concentrations in different Zones of standardized melt-spun strips extracted from Figure 4.29.

Material	f_V [%]	Cu concentration [wt. %]
MS (Zone 1)	1.9 ± 0.3	2.2 ± 0.2
MS (Zone 2)		2.0 ± 0.2
MS (Zone 3)		2.1 ± 0.1
MSSc (Zone 1)	2.0 ± 0.5	2.0 ± 0.1
MSSc (Zone 2)		2.1 ± 0.2
MSSc (Zone 3)		2.0 ± 0.1

4.3.3. Grain distributions in mold-cast materials

Standardization does not significantly impact the grain size and morphology in both mold-cast alloys (Figure 4.31, Table 4.18). The structure of both alloys is stable because the material already contains large grain, and there is no additional stored deformation energy.

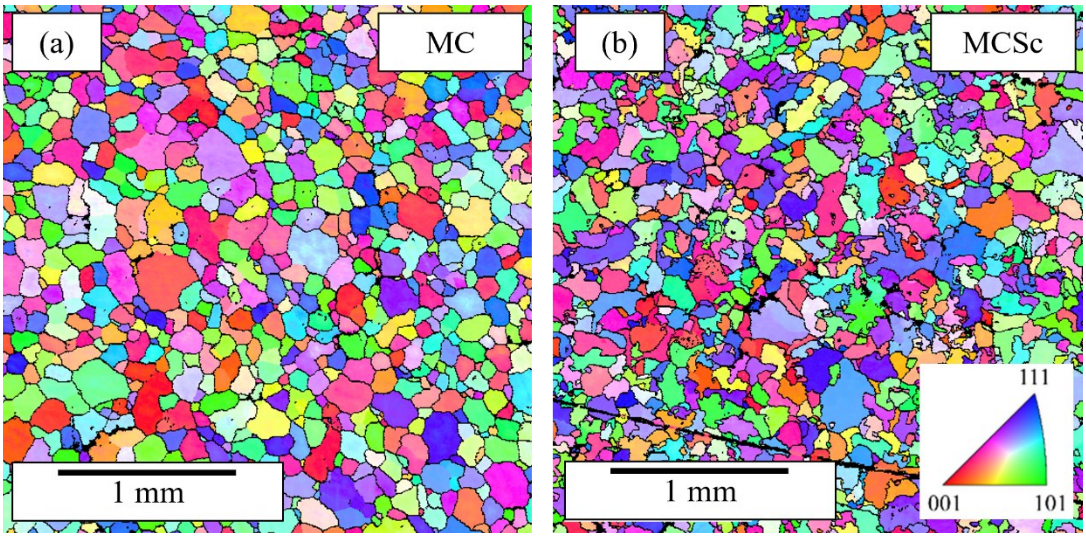

Figure 4.31 Grain orientation maps of standardized MC (a) and MCSc (b) materials. Color coding IPF triangle in the inset.

Due to the low formability of the mold-cast material, only a single CGP pass was successfully performed. No signs of dynamic recrystallization were observed, and only partial dynamic recovery occurred in both alloys (Figure 4.32 (a,c)). The MC material fully recrystallizes, while strengthening dispersoids suppress recrystallization in the MCSc material after heating at 530 °C (Figure 4.32 (b,d)). No grain coarsening was observed (Table 4.18).

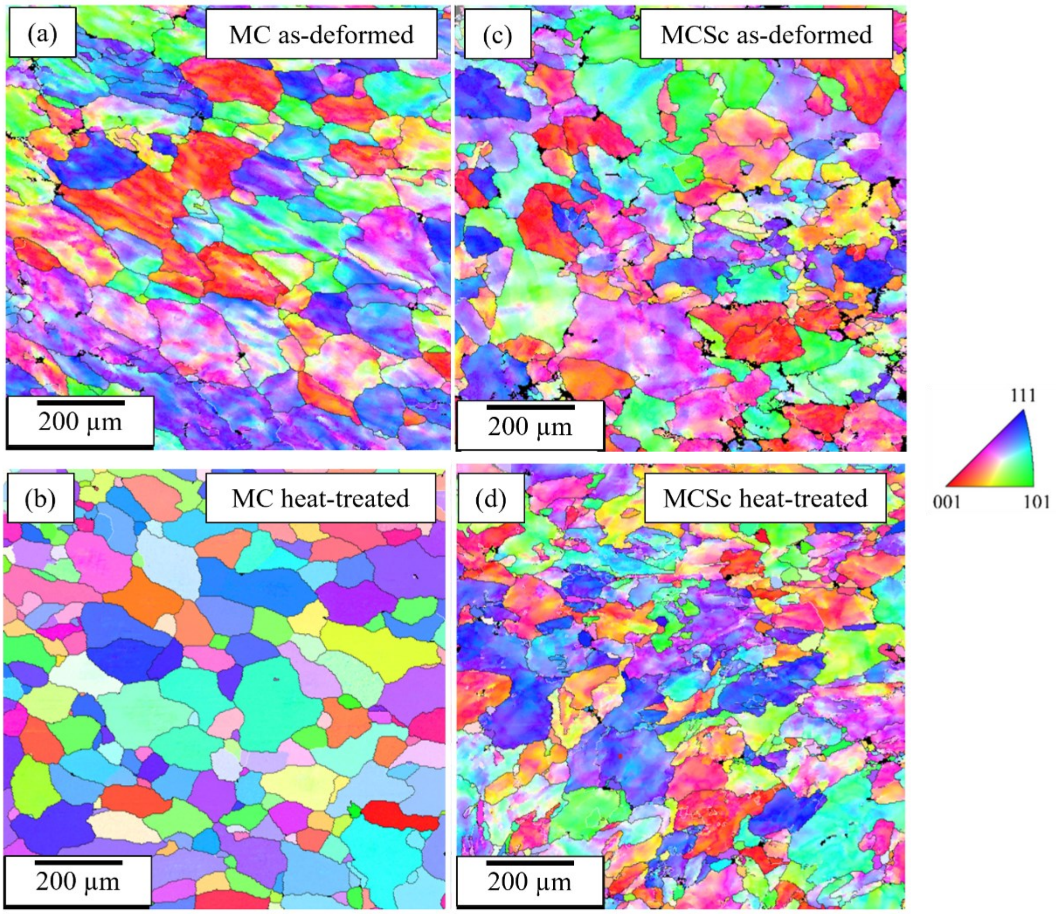

Figure 4.32 Grain orientation maps of the MC (a,b) and MCSc (c,d) materials directly after a single CGP pass (a, c) and subsequent heat treatment at 530 °C (b,d).

Table 4.18 Grain sizes of the mold-cast materials at various stages of processing. Grain sizes in μm.

Material	As-cast	Standardized without CGP	After CGP	Standardized with CGP
MC	160 ± 10	160 ± 10	150 ± 10	140 ± 20
MCSc	130 ± 20	130 ± 10	150 ± 20	140 ± 10

4.3.4. Grain distributions and textures in TRC materials.

The elevated standardization temperatures significantly influence the grain structures of both TRC materials. The structure is stable in the TSc material, but the increased temperatures result in significant grain growth, coarsening, and an inhomogeneous distribution of grain sizes in the T material (Figure 4.33, Table 4.19).

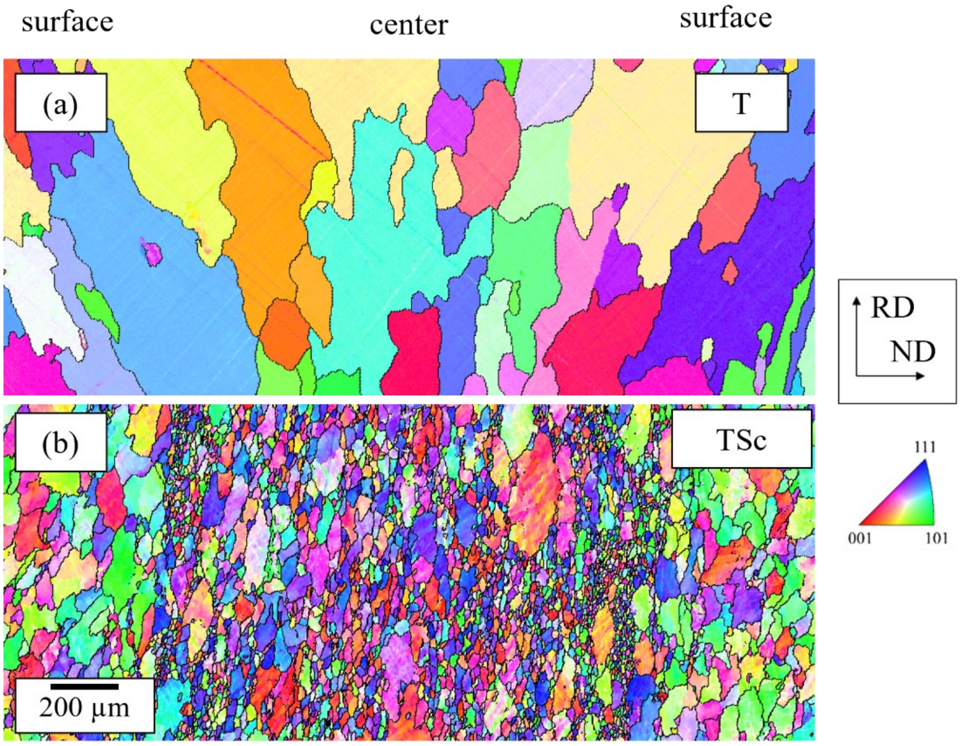

Figure 4.33 Grain orientation maps of 1 mm wide surface-to-surface sections of standardized T (a) and TSc (b) material.

The twin-roll cast materials were subjected to three CGP passes, symmetrical and asymmetrical rolling.

Rolled TRC materials exhibit heavily deformed structures with flat grains after both symmetrical (SR) and asymmetrical (AR) rolling (Figure 4.34). The T material fully recrystallizes regardless of the rolling regime. There is no variance in the size of the recrystallized grains across the thickness of the strips. The recrystallized grain size is lower than the original grain size of the T strip in the as-cast state and an order of magnitude lower than in the strip standardized without deformation (Table 4.19). The TSc strips do not recrystallize except for narrow sections on the strip surfaces.

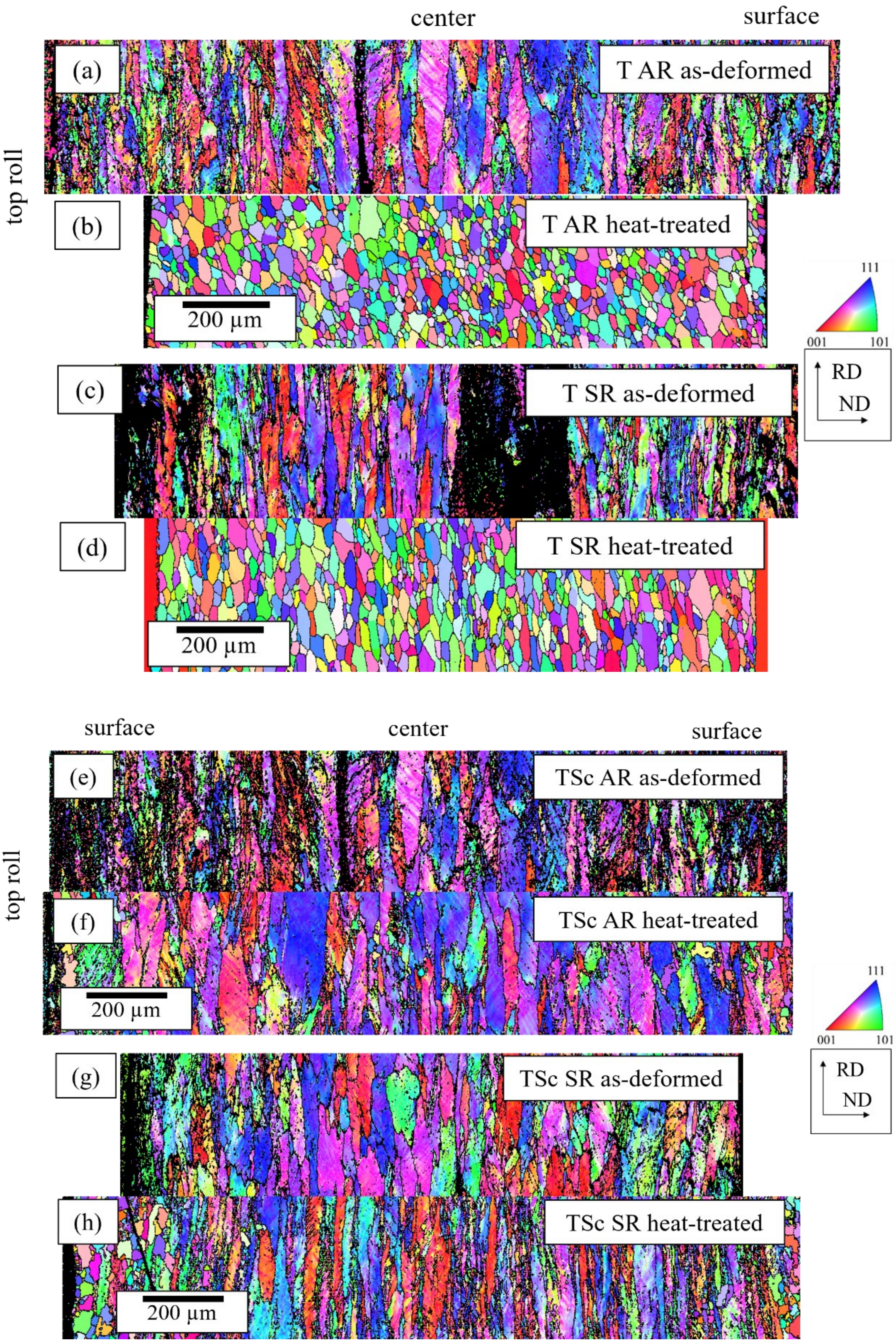

Figure 4.34 Grain orientation maps of 300 μm wide surface-to-surface sections of the T AR (a,b), T SR (c,d), TSc AR (e,f), and TSc SR (g,h) materials directly after rolling (a,c,e,g) and subsequent heat-treatment at 530 °C for 30 min (b,d,f,h). The faster spinning top roll in the AR setup indicated in the T AR and TSc AR materials.

Twin-roll cast materials subjected to CGP were deformed at higher temperatures (450 °C) to facilitate higher formability and produce compact strips even after three full CGP passes. Samples of the T material deformed at this temperature exhibit abnormal grain growth. The final standardization step only induced partial recovery, and no recrystallization or further grain growth was observed (Figure 4.35 (a,b)). No grain refinement occurs during the CGP of the TSc material (Table 4.19). However, the grains are equiaxed, and their size is homogeneous throughout the whole thickness of the strip due to the shear nature of the deformation during CGP (Figure 4.35 (c),(d)). Recovery and recrystallization are suppressed during the final standardization step.

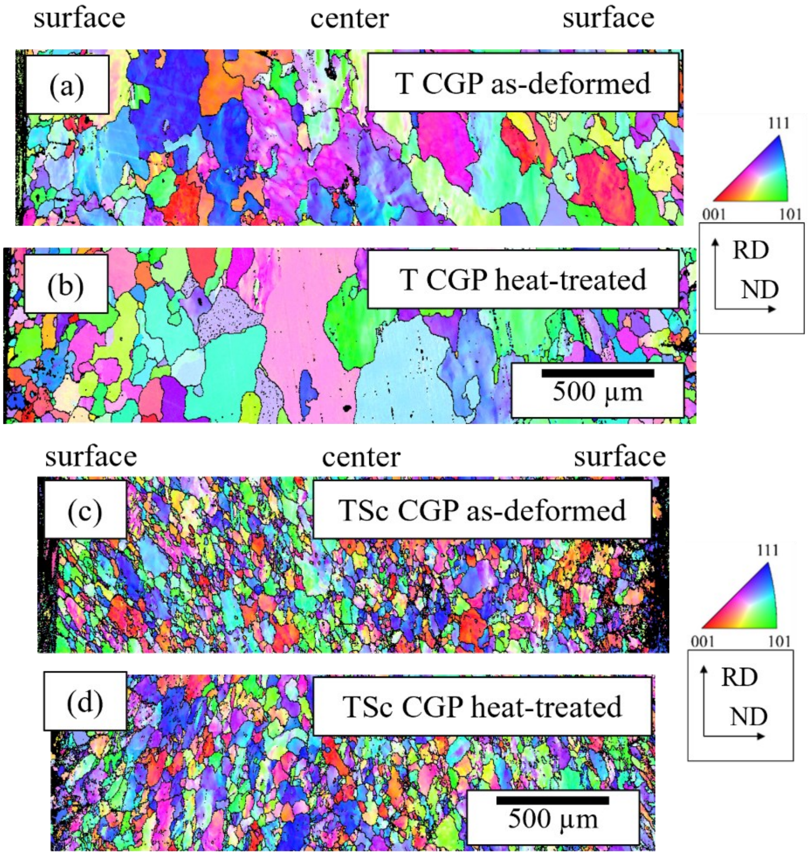

Figure 4.35 Grain orientation maps of 800 µm wide surface-to-surface cross sections of the T (a,b) and TSc (c,d) materials after 3 CGP passes at 450 °C (a,c) and subsequent heat-treatment at 530 °C for 30 min (b,d).

Table 4.19 Grain sizes in TRC materials at various stages of processing. Grain sizes in μm.

Material	As-cast	Standardized without deformation	After deformation	Standardized with deformation
T	110 ± 10	220 ± 10	-	-
T SR	-	-	74 ± 13	35 ± 3
T AR	-	-	74 ± 18	38 ± 3
T 3CGP	-	-	180 ± 50	240 ± 20
TSc	90 ± 13	73 ± 16	-	-
TSc SR	-	-	77 ± 6	67 ± 8
TSc AR	-	-	77 ± 10	83 ± 8
TSc 3CGP	-	-	74 ± 11	88 ± 6

The texture of the twin-roll cast materials depends on the applied mechanical processing and composition (Al_3Zr/$Al_3(Sc,Zr)$ dispersoids), which affects recrystallization. Partially recrystallized or unrecrystallized grains are generally associated with higher fracture toughness and crack growth resistance, leading to higher ductility [79]. Figure 4.36 shows inverse pole figures related to the normal direction of the materials. The as-cast alloy B has a noticeable <100> component, strengthening during standardization. Rolling (SR and AR) of the alloy induces a <101> component, which is suppressed by recrystallization during standardization, and <100> becomes the primary component. CGP of the alloy induces <111> and <201> components, but the <111> component is suppressed during standardization. The as-cast alloy A has a weaker texture than alloy B, but the <100> component is strengthened during standardization. The <101> component induced by rolling (SR and AR) is retained due to a lack of recrystallization during standardization in this alloy. Similarly, the <111> component is induced by CGP in this alloy. The component is retained during standardization, and an additional <201> component is formed.

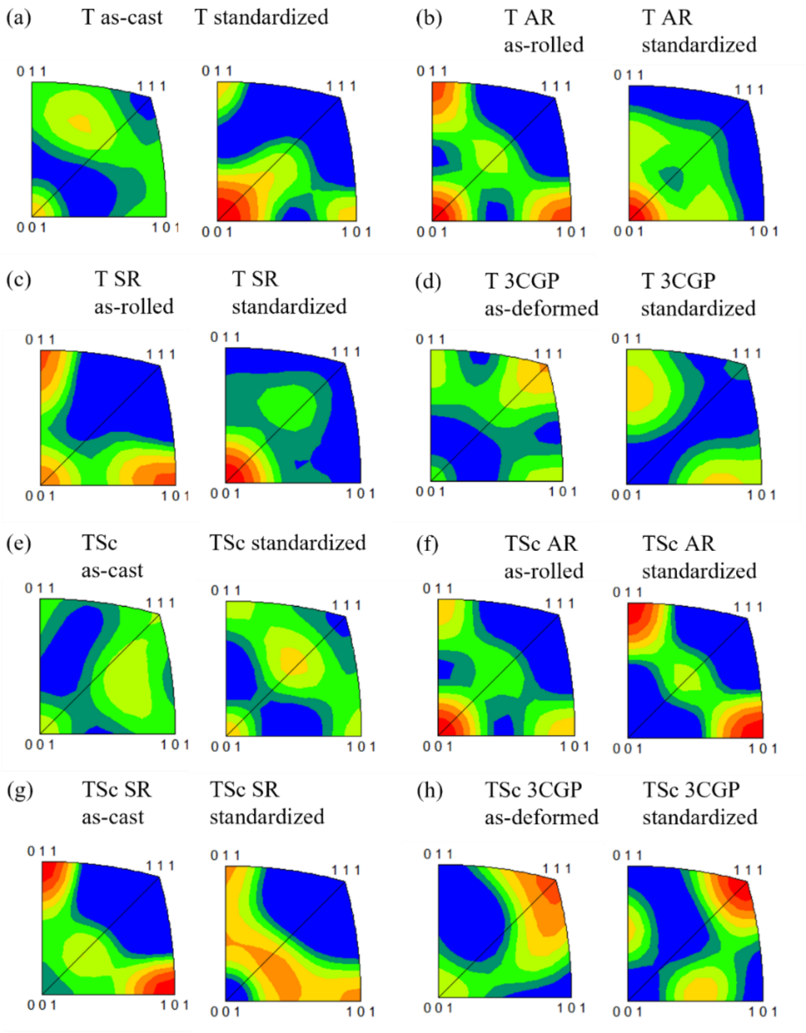

Figure 4.36 Inverse pole figures of the T (a) and TSc (e) materials in the as-cast states and after standardization. Inverse pole figures of the remaining thermomechanical processing variants after deformation and subsequent standardization: T AR (b), T SR (c), T 3CGP (d), TSc AR (f), TSc SR (g), and TSc 3CGP (h) materials. Textures related to the normal direction of the strips.

4.3.5. Grain distribution in melt-spun strips

The shape and inhomogeneity of the melt-spun strips do not allow any deformation during the standardization process. Therefore, the effect of standardization on as-prepared melt-spun materials is demonstrated.

Columnar regions of the melt-spun strips remain mostly stable during the short-term standardization (Figure 4.37). In contrast, the originally equiaxed part (Zone 3) of the MS strip significantly grows (Figure 4.37 (a), indicated by a white arrow). Globular segments protruding from the MSSc strip (Zone 3) were originally equiaxed and remained stable after standardization (Figure 4.37 (b), highlighted in white). The average grain sizes of the melt-spun strips are the same as those observed in the as-cast states (Table 4.20).

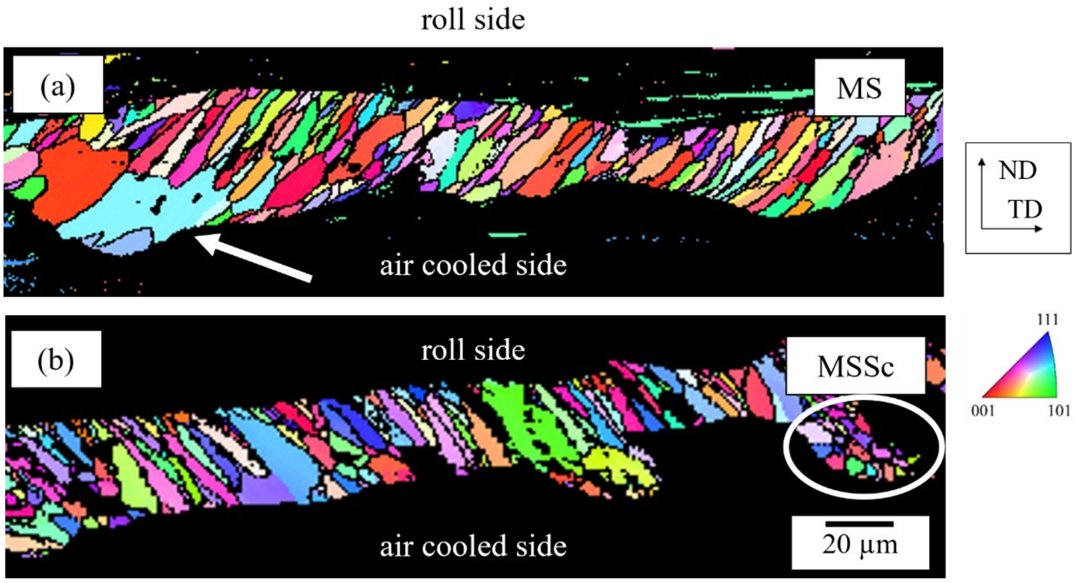

Figure 4.37 Grain orientation maps of the MS (a) and MSSc (b) materials after short-term standardization. White oval highlights the equiaxed protrusion, white arrow highlights the coarsening in the original Zone 3 of the MS strip.

Table 4.20 Grain sizes comparison in melt-spun strips before and after standardization. Grain sizes in µm.

Material	As-cast	Standardized
MS	8.7 ± 1.6	11 ± 3
MSSc	7.3 ± 0.7	12 ± 3

4.3.6. Standardization summary and the influence of grain refining dispersoids

Mold-cast materials show a decrease in the volume fraction of primary phases, but the surplus elements released by the transformation and dissolution of primary phases spread across a zone approximately 20 µm wide. This width is significantly smaller than the average ECS for the mold-cast materials (Table 4.7). Additionally, this observation agrees with the estimate of diffusion length performed in part 4.1.5 (Table 4.11), confirming the necessity of significantly longer homogenization holding times required for those materials.

Evolutions of alloying element distributions in twin-roll cast materials and Zones 2 and 3 of the melt-spun materials are similar during standardization. Fragmentation of continuous grain boundary phases into individual particles, decrease in the total volume fraction of primary phases, and increase in matrix Cu concentration occur. The persistent particles are the complex Al_7Cu_2Fe phases in both alloys.

Grain sizes of the standardized materials are determined by the mechanical treatment before the final standardization step and the size of the nanoscale Al_3Zr or $Al_3(Sc,Zr)$ dispersoids. Zener drag imposed by the dispersoids inhibiting grain boundary motion during recrystallization can be calculated as:

$$P_Z = \frac{3 f_V \gamma}{2r}, \tag{4.7}$$

where f_V is the dispersoid volume fraction, r is the dispersoid diameter, and γ is the grain boundary energy [3,164].

The diameter of the $Al_3(Sc,Zr)$ phases is, on average, 4-5 times larger than the diameter of the Al_3Zr phase (Table 4.12), but the total concentration of Sc+Zr in alloy A (0.27 wt. %) is higher than the concentration of Zr in alloy B (0.12 wt. %) and implies a higher volume fraction. An estimate based on equilibrium concentrations at 450 °C (0.01 at. % Zr, 0.02 at. % Sc [165,166]) suggests four times (0.4 % of $Al_3(Sc,Zr)$, 0.1 % Al_3Zr) the total volume fraction of the ternary precipitate resulting essentially in the same Zener drag. However, precipitation kinetics may play a role during the short annealing times employed in the standardization. The precipitation kinetics of Al_3Zr [167] and Al_3Sc [166] estimate up to 80 % of Sc in dispersoids and up to 30 % of the total Zr precipitated after the treatment at 450 °C. This estimate yields a 0.28 % volume fraction of $Al_3(Sc,Zr)$ and 0.03 % volume fraction of Al_3Zr as - 9.5 times the ratio and, therefore, more than twice the Zener drag imposed by the ternary particles. The higher Zener drag significantly increases the recrystallization temperature. Ding et al. [168] showed in their study of Al-Mg-Mn-Zr-based alloys with varying Sc content that 0.15 wt. % Sc addition yields an increase of the initial recrystallization temperature by approximately 100 °C and the finishing temperature beyond the melting point of the alloy.

4.4.Aged materials

All the studied alloy/casting method/treatment combinations were aged without pre-stretching (T6 temper) or with a 3 % pre-stretch (T8 temper), except for the melt-spun strips (only T6 temper).

4.4.1. T6 temper

All materials were aged for up to 100 h at 180 °C. The microhardness of the aged materials was measured at selected semilogarithmic intervals. All materials except melt-spun strips were measured with a 100 g load. During the on-edge testing, a 2 g load was selected for the melt-spun strips to ensure a small indentation size. The indents in melt-spun strips were too small for automated evaluation. Instead, manual evaluation in SEM was done.

Microhardness evolutions of all materials are qualitatively similar (Figure 4.38). The microhardness of the materials is initially constant. Microhardness increases after one hour of annealing, reaching a maximum after 20 h. The increase is relatively linear in alloy A (Figure 4.38 (b)). At the same time, the shape of the evolution is sigmoidal in alloy B, with a sharper microhardness increase above 10 h of annealing (Figure 4.38 (a)). Initial microhardness values (0.1 to 1 h range) are consistently higher for alloy A, but the peak values are around 130 HV regardless of the Sc addition. The high experimental scatter of values indicates structural inhomogeneities in the materials.

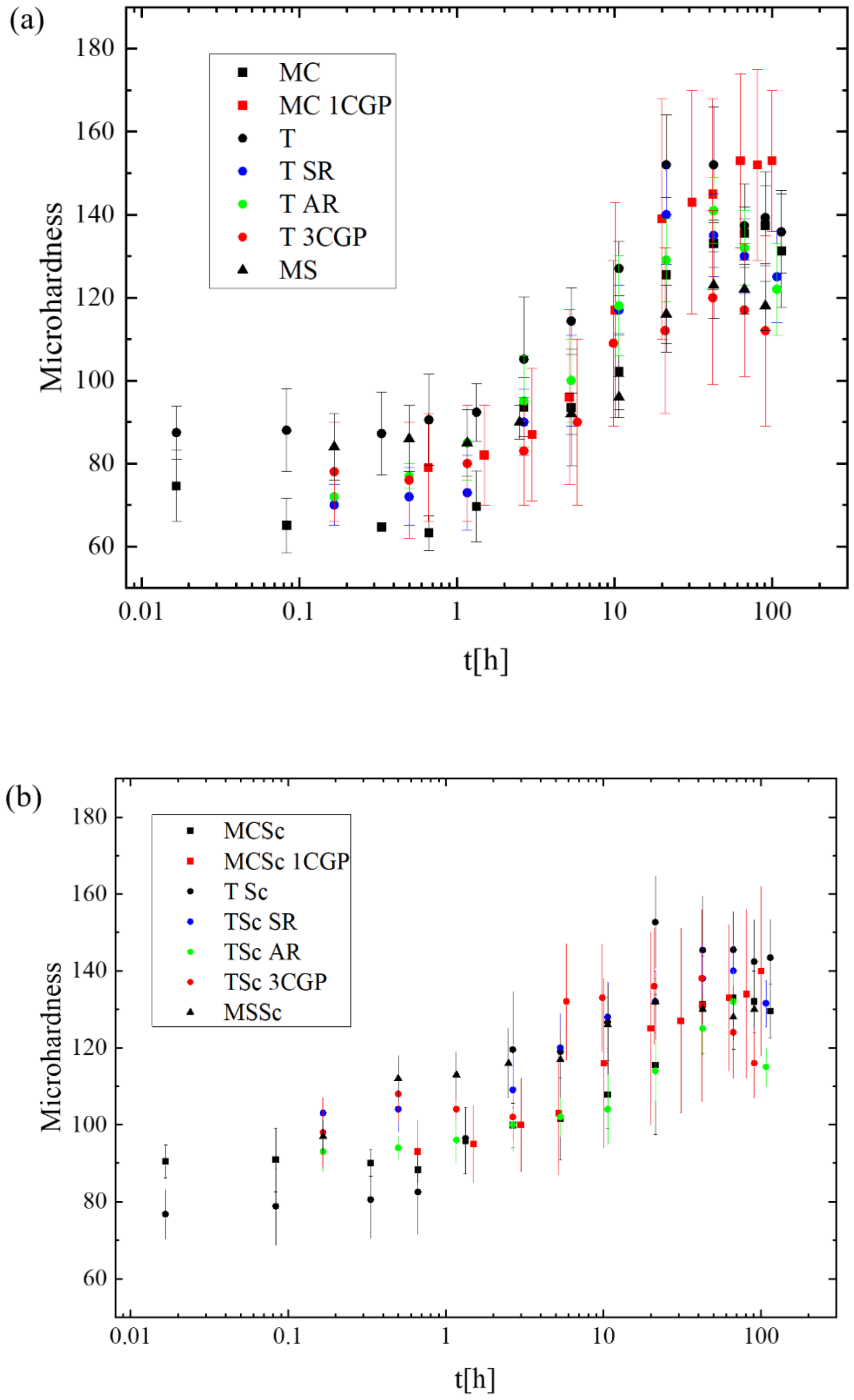

Figure 4.38 Microhardness evolutions of materials aged at 180 °C without pre-deformation. Materials of alloy B (a) and alloy A (b).

Materials aged for 40 h were selected as the "peak-aged" materials in the T6 temper and used for additional analysis in TEM/STEM. The T_1 (Al_2CuLi) phase and θ' (Al_2Cu) phase are the main strengthening precipitates formed during aging (Figure 4.39). θ' forms three unique variants of plates in $\{100\}_{Al}$ matrix planes. The T_1 phase precipitates in 4 variants of plates on $\{111\}_{Al}$ planes. Diffraction patterns of the strengthening precipitates appear as superstructural reflections due to the fixed orientation relationships between the phases and the matrix (Figure 4.40) [169].

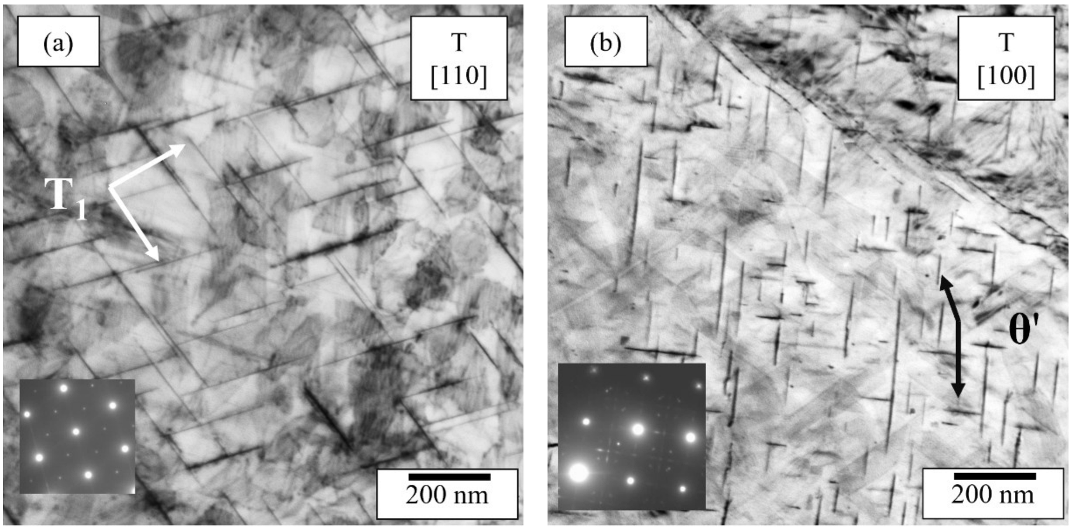

Figure 4.39 BF TEM micrographs of T_1 precipitates observed from the $[110]_{Al}$ direction (a) and θ′ precipitates observed from the $[100]_{Al}$ direction (b) in a T6 tempered T material. Selected area diffraction patterns (insets in both materials).

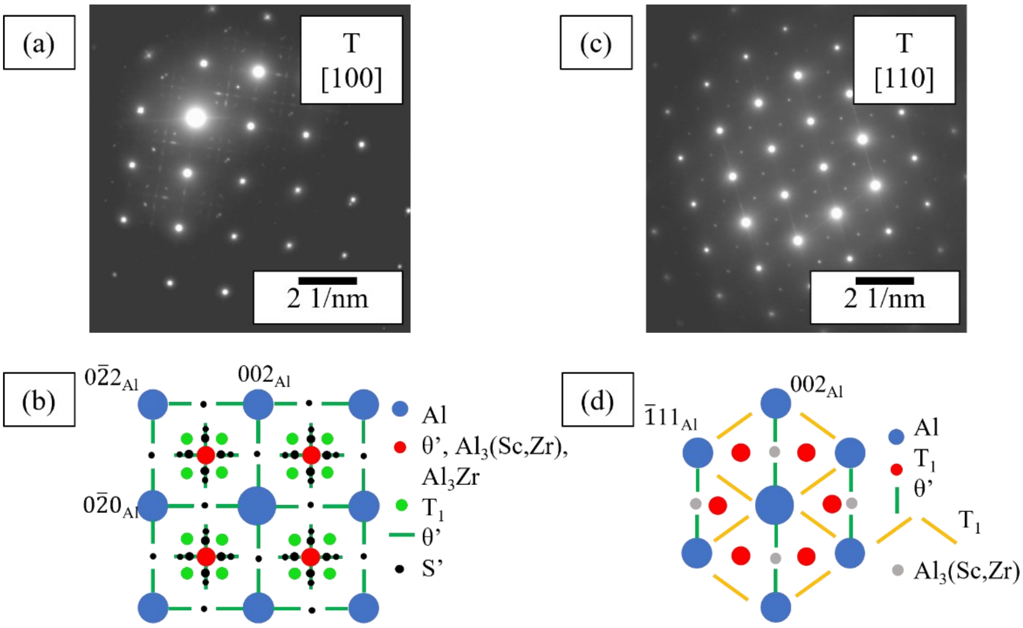

Figure 4.40 Single grain selected area diffraction patterns of the T6 tempered T materials in the $[100]_{Al}$ (a) and $[110]_{Al}$ (c) zones. Schematic representations of the patterns with reflections from the strengthening particles and grain refining dispersoids (b,d).

The strengthening of materials reached during aging primarily depends on strengthening particles. Their volume fractions, size, and distribution are strongly affected by (sub)grain boundaries. Boundary precipitation is preferred. The distribution of strengthening particles in the grain interiors is homogeneous, as documented in Figure 4.41 (a), (b). The formation of coarse boundary particles siphons alloying elements from the surrounding matrix, resulting in the formation of precipitate-free zones (PFZ) in their vicinity and an inhomogeneous distribution of particles (Figure 4.41 (c-n)).

On the other hand, only the coarse-grained MCSc contains a homogeneous distribution of precipitates (Figure 4.42 (a),(b)), while the other materials of alloy A always contain a dense network of subgrain boundaries resulting in a pronounced (sub)grain boundary precipitation, formation of broad PFZs, and an inhomogeneous distribution of strengthening particles (Figure 4.42 (c-n)).

Table 4.21 summarizes the diameters of the two main strengthening precipitates in the T6 temper. Their sizes range from 50 nm to 400 nm. The width of the PFZs is highly local, often approaching 200 nm.

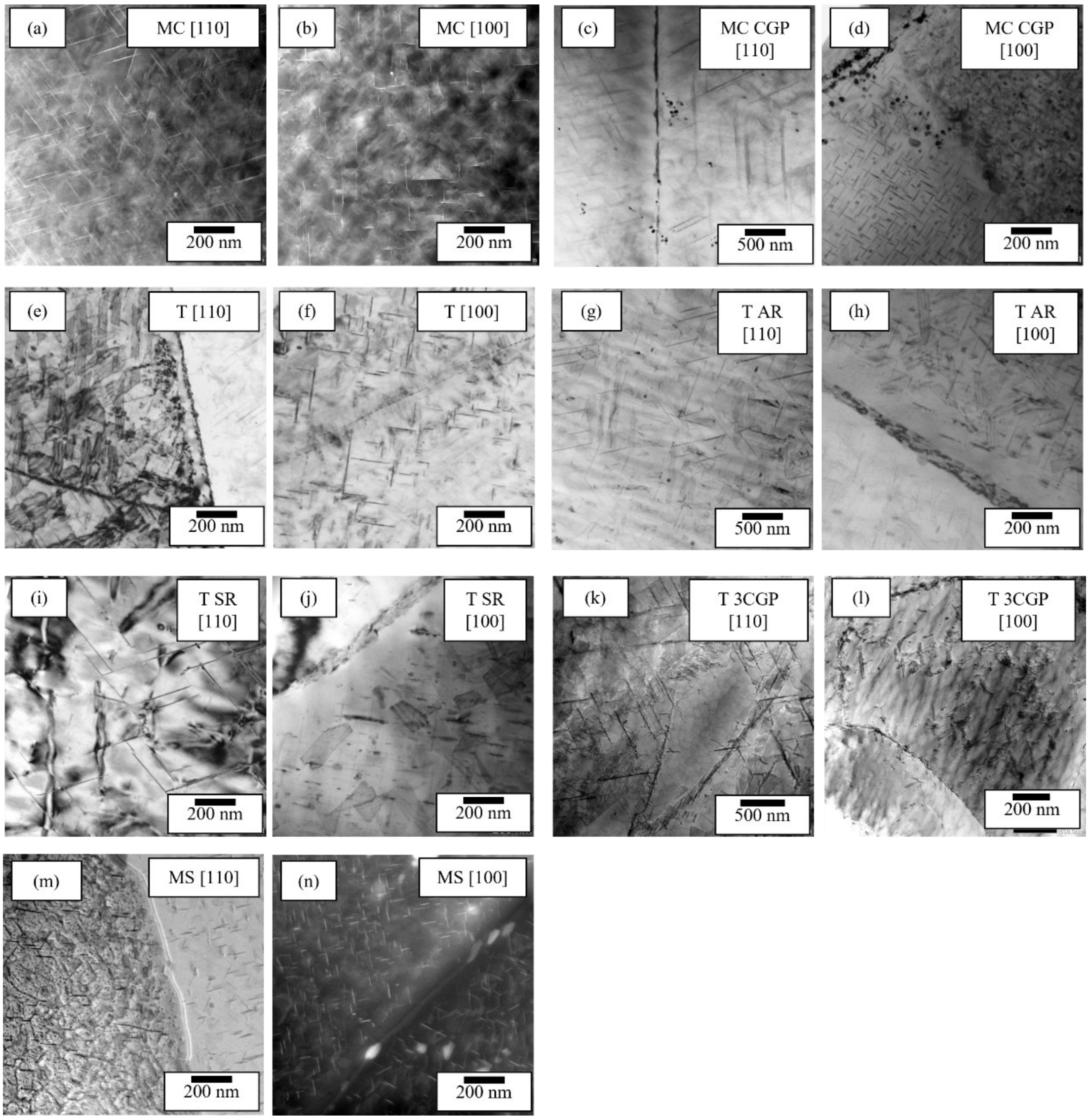

Figure 4.41 BF TEM (c-j), BF STEM (k-m), and HAADF STEM (a,b,n) micrographs of T6 tempered materials from alloy B aged at 180 °C for 40 h.

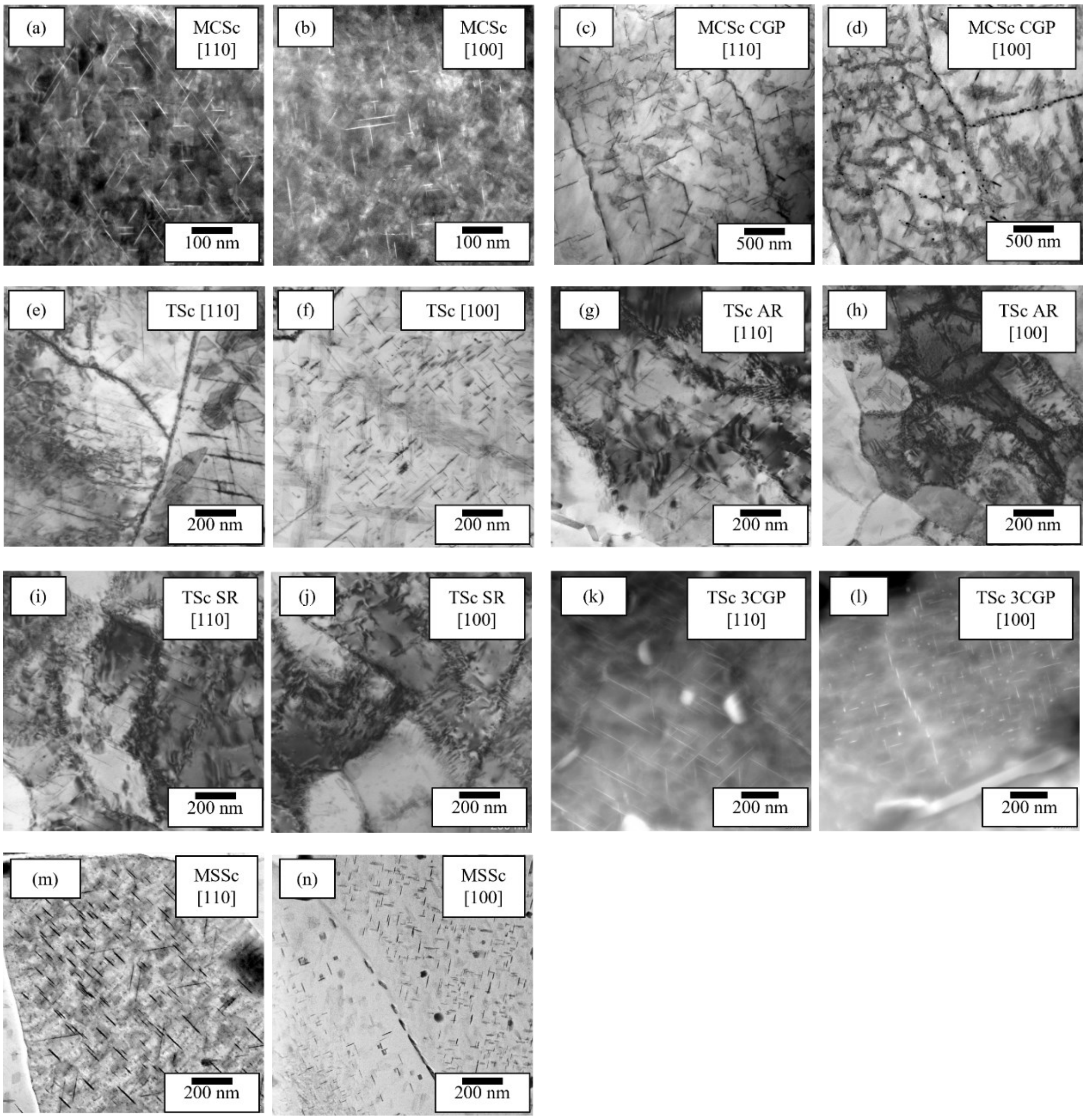

Figure 4.42 BF TEM (c-j), BF STEM (m,n), and HAADF STEM (a,b,k,l) micrographs of T6 tempered materials of alloy A aged at 180 °C for 40 h.

Table 4.21 Sizes of the two primary strengthening precipitates in materials in the T6 temper.

	MC	MCCGP	T	TSR	TAR	T3CGP	MS
$d_{\theta'}$ [nm]	110 ± 20	73 ± 33	76 ± 13	100 ± 40	110 ± 30	100 ± 20	54 ± 13
d_{T1} [nm]	340 ± 80	360 ± 100	270 ± 60	260 ± 50	280 ± 60	400 ± 170	97 ± 28
	MCSc	MCSc CGP	TSc	TSc SR	TSc AR	TSc 3CGP	MSSc
$d_{\theta'}$ [nm]	100 ± 30	100 ± 10	140 ± 30	56 ± 21	48 ± 18	49 ± 21	67 ± 18
d_{T1} [nm]	370 ± 100	190 ± 70	230 ± 60	120 ± 40	110 ± 40	180 ± 60	80 ± 27

Room tensile tests performed on T6 tempered TRC materials have the same yield strength (YS) within the experimental error. Both rolling and CGP positively influence maximum attained elongation, which increases by an order of magnitude compared to the undeformed T and TSc materials, which reach elongations below

1 % before fracture. The ultimate tensile strength (UTS) is almost the same as YS within the experimental error except for specimens processed by CGP (Figure 4.43).

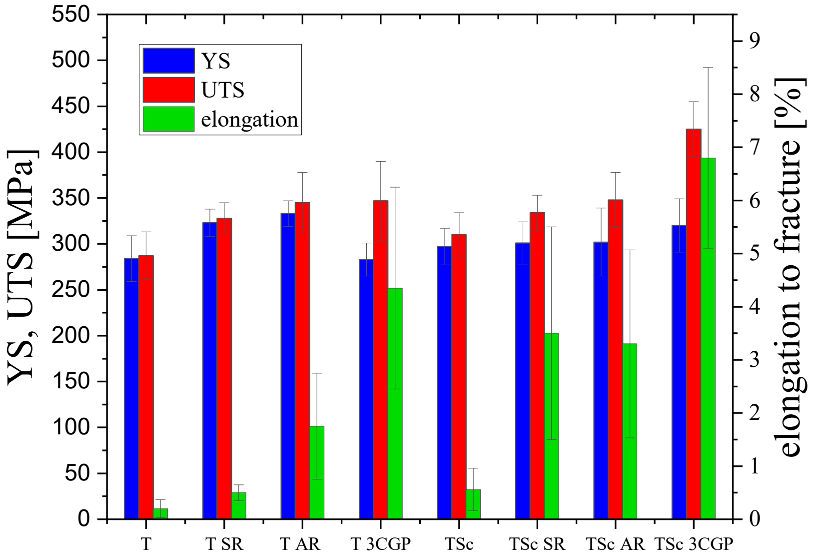

Figure 4.43 Tensile properties of the TRC materials in the T6 temper. Yield strength (blue), ultimate tensile strength (red), and elongation to fracture (green).

4.4.2. T8 temper

The precipitation kinetics of pre-stretched materials is faster, and the peak-aged state is reached after 10 h of annealing (Figure 4.44). No significant differences between the aging kinetics of alloys A and B were observed. The initial hardness values in materials with Sc addition are higher, but the peak-aged values are the same within the experimental scatter.

Materials aged for 10 h were selected for further TEM/STEM observations. Twin-roll cast and processed materials were tested in tension after aging for 10 h.

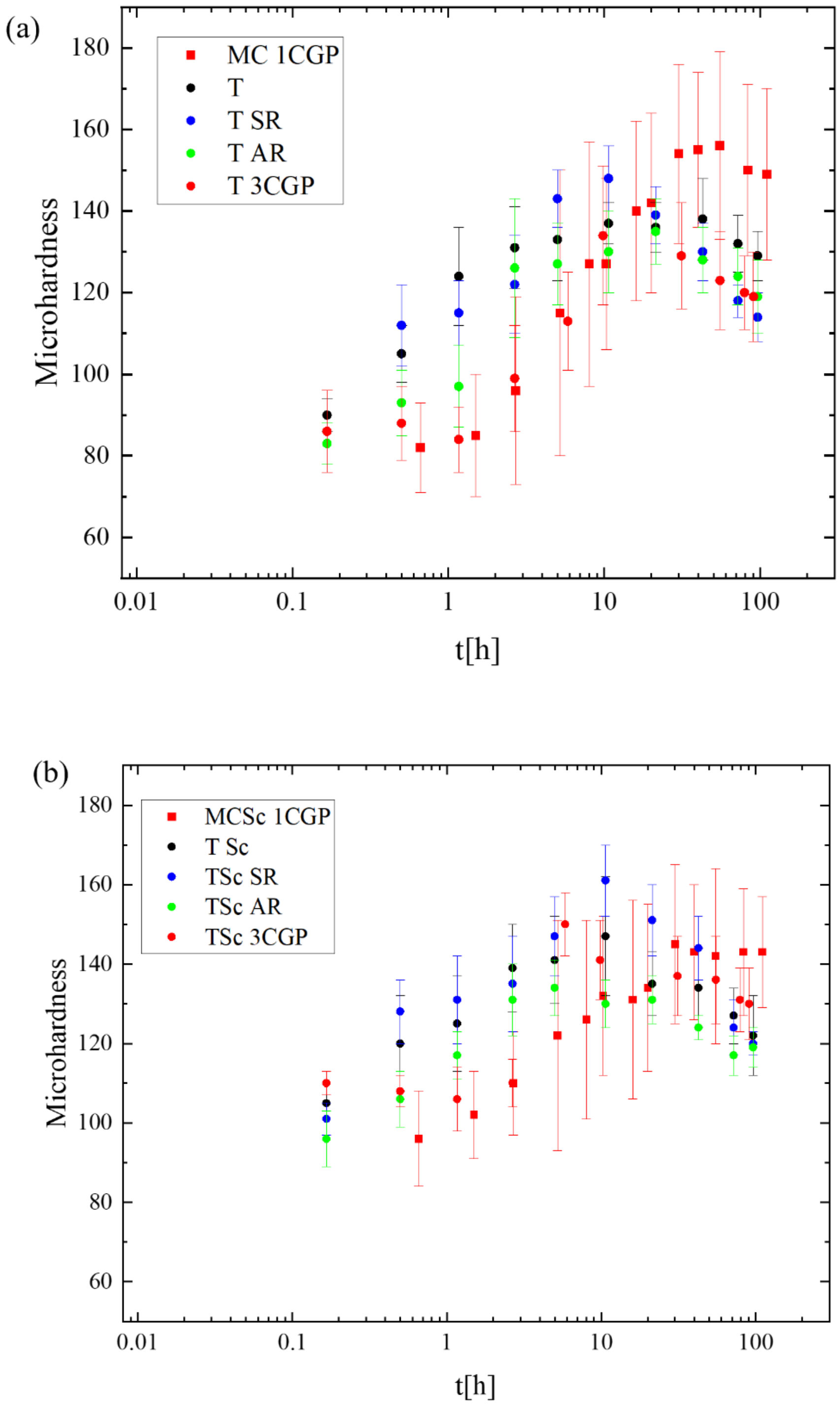

Figure 4.44 Microhardness evolutions during aging at 180 °C of the materials aged after pre-stretching. Materials of alloy B (a) and alloy A (b).

Materials after T8 temper exhibit substantial refinement of strengthening particles, reduction of PFZs, and limitation of grain boundary precipitation (Figure 4.45, Figure 4.46). The main strengthening phase is T_1, and the formation of θ' is suppressed. The length of the primary strengthening precipitates is summarized in Table 4.22. The width of the PFZs decreases by approximately 50 %.

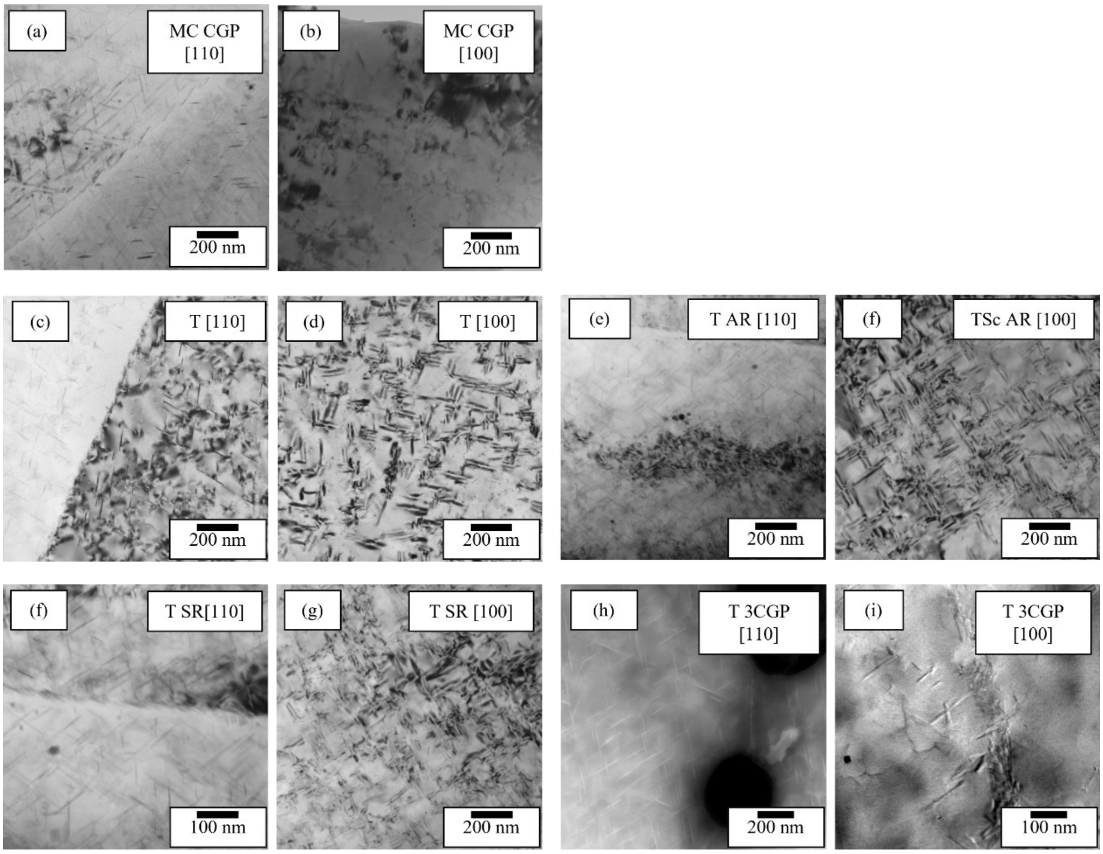

Figure 4.45 BF TEM (a-g), BF STEM (i), and HAADF STEM micrographs (h) of pre-stretched alloy B after 10 h of aging at 180 °C.

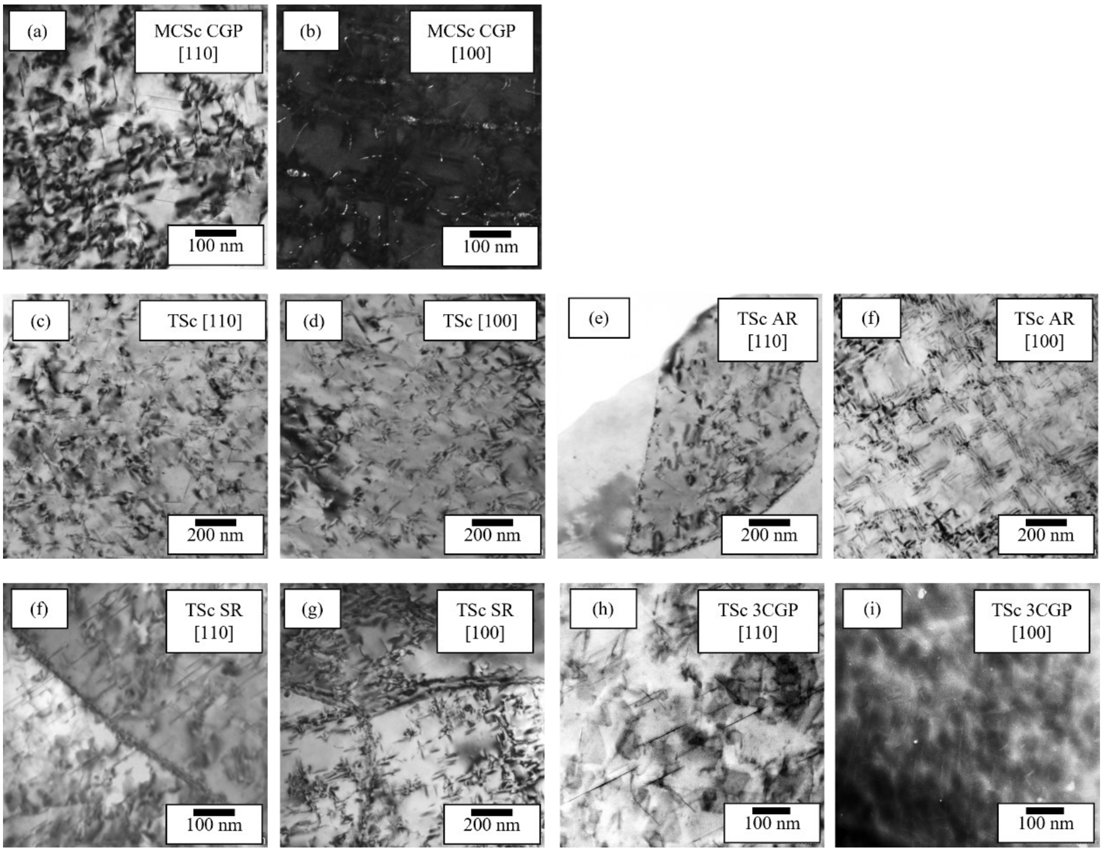

Figure 4.46 BF TEM (a, c-g), DF TEM (b), BF STEM (h) HAADF STEM (i) micrographs of strengthening particles in pre-stretched alloy A after 10 h aging at 180 °C.

Table 4.22 Sizes of the T_1 and θ' precipitates in the materials aged for 10 h after pre-stretching.

	MC CGP	T	T SR	T AR	T3CGP
$d_{\theta'}$ [nm]	73 ± 46	44 ± 16	46 ± 12	39 ± 11	42 ± 17
d_{T1} [nm]	150 ± 40	130 ± 30	190 ± 40	160 ± 50	130 ± 50
	MCSc CGP	TSc	TSc SR	TSc AR	TSc 3CGP
$d_{\theta'}$ [nm]	44 ± 28	50 ± 15	53 ± 16	57 ±11	73 ± 20
d_{T1} [nm]	70 ± 20	95 ± 23	82 ± 19	76 ± 25	80 ± 30

All the TRC materials in the T8 temper have the same YS within error (Figure 4.47). The YS is consistently higher than the YS of the materials in the T6 temper by approximately 30 – 50 MPa. The TSc 3CGP has the highest UTS of 450 MPa and elongation to fracture of 13 %.

In the following sections, we will try to estimate the individual contributions to the total strengthening of the TRC materials and find the main mechanism controlling their ductility.

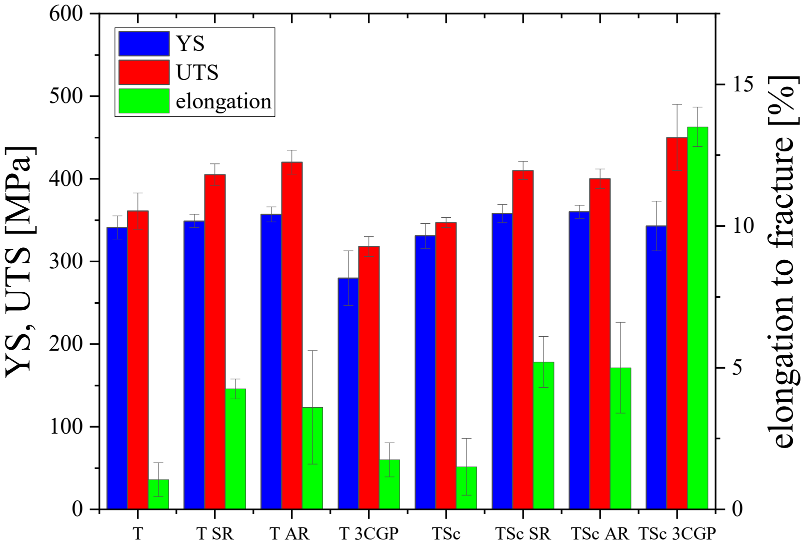

Figure 4.47 Tensile properties of the TRC materials in the T8 temper. Yield strength (blue), ultimate tensile strength (red), and elongation to fracture (green).

4.4.3. Strengthening contributions

The final strength of the material can be estimated as a simple sum of individual contributions from the different strengthening mechanisms [170].

$$\sigma_{total} = \sigma_{Al} + \sigma_{const.} + \sigma_{OR} + \sigma_{HP} + \sigma_{solute} \tag{4.8}$$

σ_{total} is the sum of all the contributions, σ_{Al} is the contribution of pure Al, $\sigma_{const.}$ is the strengthening of the remaining constituents, σ_{OR} is the Orowan strengthening contribution of the Al_3Zr or $Al_3(Sc,Zr)$ phases, the T_1 phase and the θ' phase, σ_{HP} is the Hall-Petch contribution to strengthening from grain structures, and σ_{solute} is the solid solution contribution.

The UTS and the individual contributions can be directly related to measured microhardness (HV) through a simple formula [171]:

$$HV = 0.3\sigma. \tag{4.9}$$

Zhao et al. [172] estimate the contribution of AlCuFe-based coarse boundary intermetallics to the total materials strength at approximately 1.25 MPa per 1 % of their volume fraction. Therefore, the primary phase strengthening is considered negligible in our estimation.

The contribution of the grain refining Al_3Zr and $Al_3(Sc,Zr)$ dispersoids can be calculated using a modified Orowan strengthening equation reported by Liu et al. [165]:

$$\sigma_{OR} = 0.4MGb\ln\left(\frac{d}{b}\right) * \frac{1}{\left(\sqrt{\left(\frac{3\pi}{4f_V}\right)} - 1.64\right)0.5d\pi\sqrt{1-\upsilon}}, \tag{4.10}$$

d is precipitate diameter, f is their volume fraction, G is shear modulus (25.4 GPa for Al), b is the Burgers vector (0.286 nm), υ is the Poisson ratio (0.33), M is the Taylor factor (~ 3.06 in FCC materials). Using this equation, the values for the two alloys from Table 4.12 and the volume fractions discussed in part 4.3.6, we calculate the contributions as (31 ± 9) MPa for the Al_3Zr particles and (45 ± 13) MPa for the $Al_3(Sc,Zr)$ particles.

The presence of the grain refining particles influences the final grain size of the material and, implicitly, the Hall-Petch contribution to strengthening, which can be calculated as:

$$\sigma_{HP} = k_{GS}.GS^{-\frac{1}{2}}, \tag{4.11}$$

where k_{GS} is a constant (0.04 MPa.m$^{-1/2}$ for Al alloys), and GS is the grain size [173]. Using the measured values from Table 4.18, Table 4.19, and Table 4.20, we obtained values for Hall-Petch strengthening, summarized in Table 4.23. The values range from 2.7 to 12 MPa. While the variation of strengthening contributions is large, the total strengthening contribution is low compared to the total strength of the tested materials.

Table 4.23 Hall-Petch contributions to the total strength.

	MC	MC CGP	T	T rolled	T 3CGP	MS
σ_{HP} [MPa]	3.0 ± 0.1	3.4 ± 0.5	2.7 ± 0.1	6.7 ± 0.6	2.6 ± 0.2	12 ± 3
	MCSc	MCSc CGP	TSc	TSc rolled	TSc 3CGP	MSSc
σ_{HP} [MPa]	3.5 ± 0.3	3.4 ± 0.3	4.6 ± 1.0	4.5 ± 0.5	4.3 ± 0.3	12 ± 3

Hall-Petch strengthening and strengthening by the grain refining trialuminides are the primary contributors to strength/microhardness directly after standardization. Depending on the material, the difference between the sum of these contributions between the two alloys is around 16 MPa (~ 5 HV), which the experiment could not distinguish (see Figure 4.38, Figure 4.44).

Contribution to the strengthening of the T_1 and θ' precipitates depends on the size and volume fraction of the individual precipitates. The volume fraction (f_V) and number fraction (f_N) of a specific type of particle can be calculated as:

$$f_V = \frac{N_p V_p}{V_S};\ f_N = \frac{N_p}{V_S}, \tag{4.12}$$

where N_p is the number of particles in an observed area, V_p is the average volume of a single particle, and V_S is the volume of the observed zone. A constant sample thickness is considered. Then, the volume V_S is calculated as the observed area multiplied by the sample thickness t_s, which can be determined by convergent beam electron diffraction (CBED).

Both main strengthening precipitates are theoretically disc-shaped. The measured size in TEM depends on the local thickness of the sample. The real size of the precipitates can be calculated as:

$$d = d_m \frac{(d_m + t_s)}{\left(\frac{\pi}{4} d_m + t_s\right)}, \tag{4.13}$$

where d_m is the measured precipitate size [174]. If the entire disc contributes to the total volume fraction of the specific precipitate (upper limit estimate), the final volume fraction of precipitates can be calculated as

$$f_{VT} = 2\frac{t_s d t_p N_p}{V_s}\ ; f_{V\theta} = 1.5\frac{t_s d t_p N_p}{V_s}, \tag{4.14}$$

where factors of 2 and 1.5 are added to include the remaining families of the T_1 and θ' phase families, which are not observed on edge, respectively. The same factor is added for the number of particles in the number fraction calculation in Equation 4.12.

T_1 phase precipitates can have discrete thicknesses corresponding to the number of neighboring Cu bilayers forming the precipitate (Figure 4.48). As such, the T_1 precipitates can be 0.51, 1.4, 2.4, or 3.4 nm thick in the case of 1, 2, 3, or 4 Cu bilayers, respectively [175].

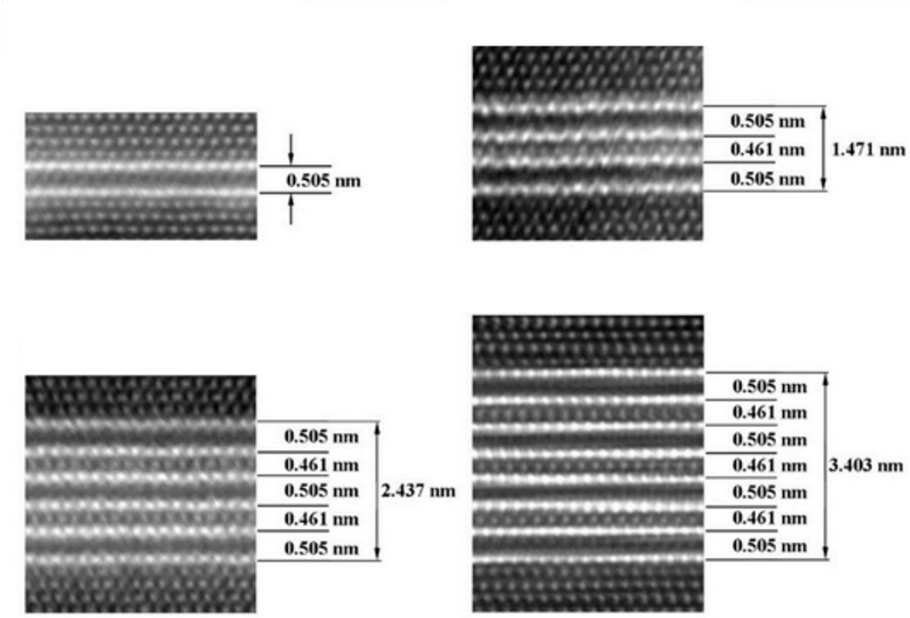

Figure 4.48 HRTEM images of different types of the T_1 phase [175].

The calculations of number and volume fractions are based on TEM and STEM observations (Figure 4.41, Figure 4.42, Figure 4.45, Figure 4.46). These highly selective observations might not correctly represent the whole volume of the specimen. To eliminate the local nature of the TEM and STEM observations, a ratio of $f_{VT1}/f_{V\theta}$ is calculated, and an estimate of maximum possible strengthening is made. This estimate assumes that all the non-equilibrium Cu dissolved in the matrix after standardization precipitates during aging. The solubility limit of Cu at 180 °C is 0.35 wt. % [159]. Differences between unit cells of the two precipitated phases and the Al matrix must be considered to refine the estimate. The unit cell of θ' is tetragonal with $a_\theta = 0.404$ nm and $c_\theta = 0.580$ nm [176]. The unit cell of T_1 is hexagonal with $a_{T1} = 0.495$ nm and $c_{T1} = 0.933$ nm [29]. These unit cells correspond to 33.0 Å^3 per atom for the Al matrix cell, 31.6 Å^3 per atom for the θ' matrix cell, and 49.5 Å^3 per atom for the T_1 matrix cell. Once the maximum volume fractions of each phase are established, the strengthening contributions are calculated according to Equation 1.1 and Equation 1.3.

The measured volume fraction ratios differ substantially across the states, ranging from 0.5 $f_{VT1}/f_{V\theta}$ for the MC material to approximately 40 $f_{VT1}/f_{V\theta}$ for the 3CGP T8 states (Table 4.24). In general, the ratio increases with the addition of Sc and then further increases in the T8 temper. In both cases, it results from increased nucleation of the phase by increasing the volume fraction of subgrain boundaries or by increased dislocation density. This ratio, however, does not reflect the homogeneity of the T_1 phase distribution, which is improved in the T8 states. Additionally, materials of alloy B in the T8 temper have a comparable or higher $f_{VT1}/f_{V\theta}$ ratio, likely induced by a homogeneous dislocation density in the large subgrain-free grains.

The $f_{VT1}/f_{V\theta}$ ratio in the melt-spun materials is similar to that in the MC material (Table 4.24) despite the significantly lower subgrain size. This suggests that the overall volume fraction of the phase in these materials is low due to a low Li content due to surface evaporation during standardization.

Table 4.24 The $f_{VT1}/f_{V\theta}$ ratios in the materials in T6 and T8 tempers.

T6	MC	MC CGP	T	T SR	T AR	T 3CGP	MS
$f_{VT1}/f_{V\theta}$	0.5	0.6	1.3	0.7	0.8	3.5	0.6
T6	MCSc	MCSc CGP	TSc	TSc SR	TSc AR	TSc 3CGP	MSSc
$f_{VT1}/f_{V\theta}$	0.8	21	1	7.5	6.1	6.6	0.5
T8		MCCGP	T	TSR	TAR	T 3CGP	
$f_{VT1}/f_{V\theta}$		5.4	6.8	31	30	38	
T8		MCSc CGP	TSc	TSc SR	Tsc AR	TSc 3CGP	
$f_{VT1}/f_{V\theta}$		8.2	7.5	11	8	24	

The strengthening contributions of the two phases are comparable for mold-cast materials of alloy B in the T6 temper (Table 4.25). The ratio of strengthening contributions of the two phases remains close to 1 for alloy B in the T6 temper except for the MS material, where the contribution of the θ' is twice as high as that of T_1. The MCSc material in the T6 temper has comparable contributions of the two phases. Twin-roll cast materials of Alloy A have noticeably higher contributions of the T_1 phase as the subgrain size decreases, leading to higher T_1 precipitation and refinement. A similar effect is observed in the MCSc CGP material, where subgrain refinement was reached through deformation.

Materials in the T8 temper show a further increase in the T_1 strengthening effect. Depending on the specific thermomechanical treatment, the resulting strengthening contribution of the T_1 phase can be eight times higher than the contribution of the θ' phase.

Table 4.25 Strengthening contributions of the T_1 phase and the θ' phase in the materials with T6 and T8 tempers

T6	MC	MC CGP	T	T SR	T AR	T 3CGP	MS
σ_{T1} [MPa]	71	62	56	94	100	53	110
$\sigma_{\theta'}$[MPa]	50	56	94	110	120	132	45
T6	MCSc	MCSc CGP	TSc	TSc SR	TSc AR	TSc 3CGP	MSSc
σ_{T1} [MPa]	65	21	72	40	44	43	100
$\sigma_{\theta'}$[MPa]	64	58	110	116	113	125	34
T8		MCCGP	T	TSR	TAR	T 3CGP	
σ_{T1} [MPa]		51	49	25	26	14	
$\sigma_{\theta'}$[MPa]		82	130	150	130	140	
T8		MCSc CGP	TSc	TSc SR	Tsc AR	TSc 3CGP	
σ_{T1} [MPa]		37	55	35	41	20	
$\sigma_{\theta'}$[MPa]		110	170	170	150	170	

While the strengthening contribution ratio changes, the sum of the two strengthening phase contributions remains relatively constant in the TRC materials, mostly between 150 MPa and 200 MPa. Tensile tests performed on standardized TRC materials without aging have yield strengths around 110 MPa (Figure 4.49). The material strengthens by approximately 50 MPa during the 3 % pre-stretching, indirectly reflected in the higher average yield strength than materials in the T6 temper (Figure 4.50).

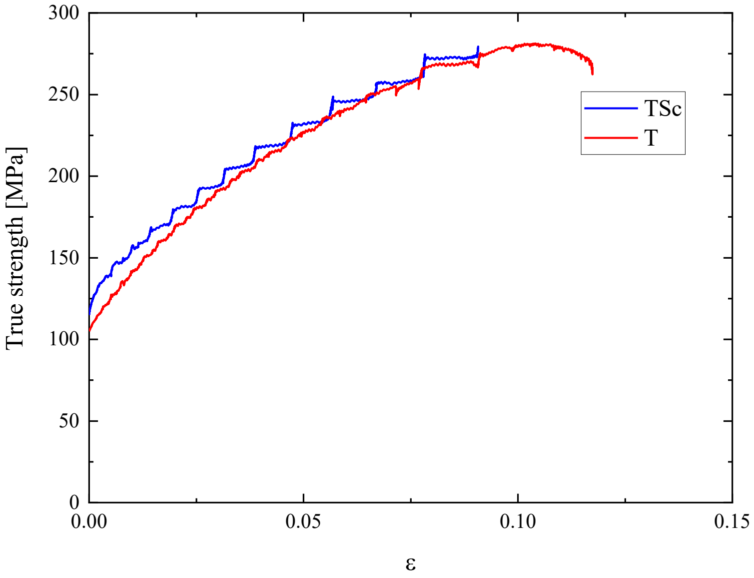

Figure 4.49 Stress/strain curves of the twin-roll cast materials after standardization.

The strength of pure Al is generally reported as 17 MPa [177]. Solid solution strengthening contribution of the equilibrium concentration of alloying elements in

Al-Cu-Li-based alloys can be estimated as approximately 65 MPa [178,179]. The total sums of all the contributions are summarized in Figure 4.50.

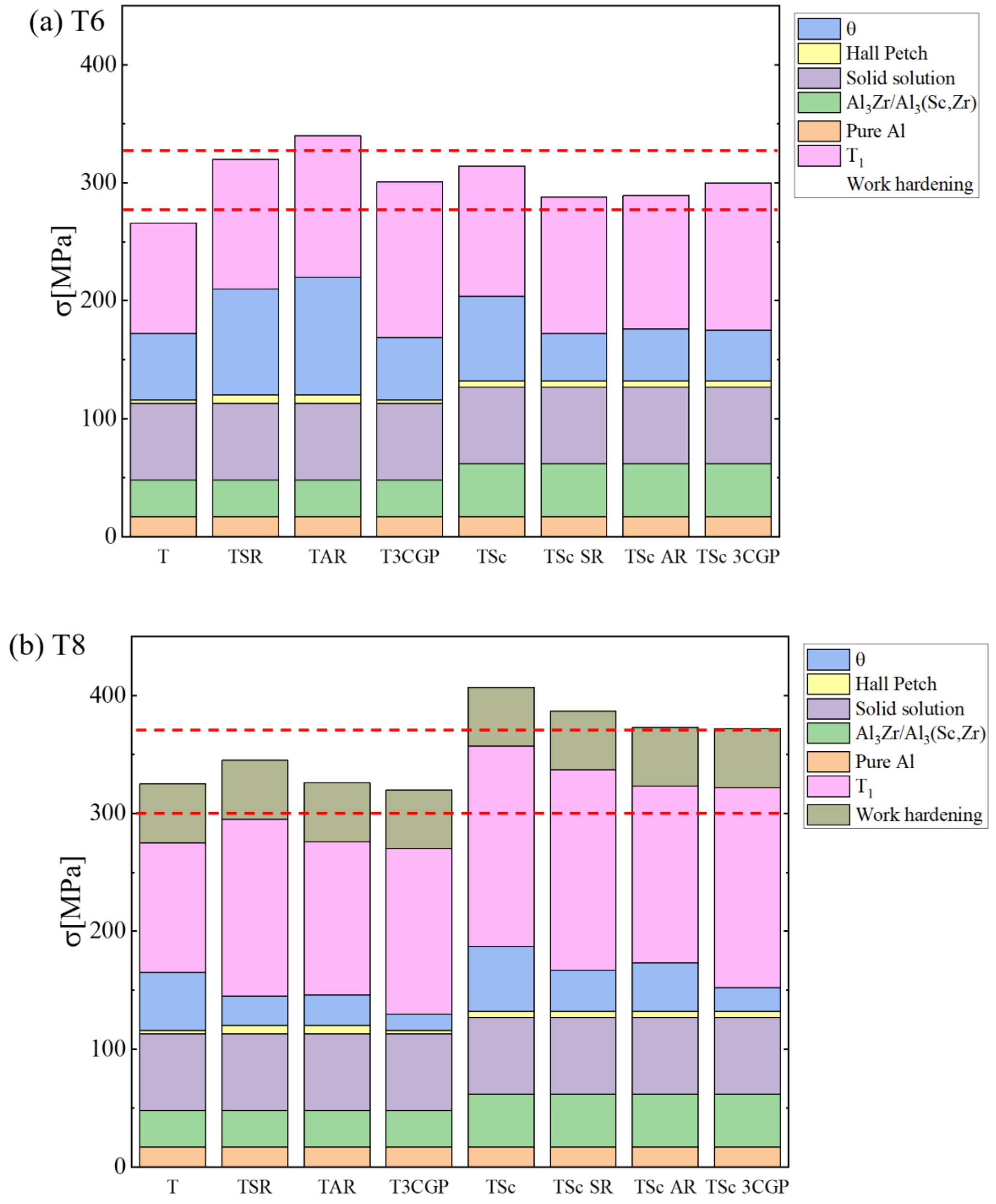

Figure 4.50 Summary of strengthening contributions in TRC materials in the T6 (a) and T8 (b) tempers. Ranges of measured yield strengths highlighted by red lines.

The estimated sum of all the contributions agrees with the measured yield strengths of TRC materials, especially considering the potential errors of individual estimates. Mainly, the strengthening precipitate calculations suffer from the highest error due to inaccuracies of observed sample thickness (up to 20 %) and measured precipitate thickness (up to 10 %).

Standard AA2195 alloys have significantly higher tensile strengths, above 500 MPa and up to 600 MPa in SPD-processed materials. However, standard AA2195 alloys contain a higher concentration of Cu and Li (up to 70 %), with the capability to increase the volume fraction of strengthening precipitates by approximately 80 %, which increases the contribution of precipitation strengthening by 35 % (50 - 70 MPa). Also, pre-stretching up to 8 % performed during standard AA2195 alloys increases the work-hardening contribution by 150 MPa [8,31,108,124,180,181]. These two contributions make up the 200 MPa difference between our alloys and the standard AA2195 materials.

4.4.4. Elongation to fracture

Higher ETF was consistently reached in the materials in the T8 temper, associated with the refinement of the T_1 phase, and improved homogeneity of strengthening particle precipitation induced by a small pre-deformation and heterogeneous precipitation on dislocations.

The highest ETF was observed in the TSc 3CGP materials in the T8 temper (Figure 4.43, Figure 4.47). This material has a high ratio of T_1/θ' strengthening contribution. While the T_1 phase contributes mainly to strength, the improved homogeneity of its precipitation contributes to improved ductility. Additionally, the shear deformation of CGP leads to a homogeneous distribution of partially recovered equiaxed grains across the strip. CGP also generates a strong <111> texture component, which is retained during standardization due to a high Zener drag of the $Al_3(Sc,Zr)$ phase (Figure 4.36).

In general, textured FCC materials show decreased formability compared to random textured FCC materials [182]. However, not all textures are equal in this regard. <100> textures significantly increase strain localization and decrease ductility [182,183]. This texture dominates in the standardized T, T SR, and T AR. Regardless, rolling positively influences the ductility of T SR and T AR by reducing grain size and improving the homogeneity of the grain size distribution (Figure 4.43, Figure 4.47). Reduction of the <100> component further improves the ductility of the T CGP material despite the grain growth.

The <100> component is weak in the standardized TSc material. The rolled TSc materials retain the strong <110> component typical for a rolled structure due to a lack of recrystallization. While no grain refinement occurs, the <110> texture improves ductility compared to the TSc material (Figure 4.43, Figure 4.47). However, a strong <111> textural component (in the TSc 3CGP material) results in the best formability compared to other components [183].

Standard AA2195 alloys generally reach elongations to fracture 8-10 % [79,106,133]. Our TSc 3CGP material has comparable properties. This high ductility highlights the strong anti-recrystallization effect of Sc-rich dispersoids, stabilizing the grain structure even at high temperatures during deformation (450 °C) and the final standardization (530 °C). These findings contradict previous attempts to add Sc into DC-cast materials [79,123,124]. No positive impact on strength or ductility in DC materials was reported because the Al3(Sc,Zr) dispersoids coarsened, losing their beneficial properties. This further highlights the optimization achieved by the proposed model processing.

5. Discussion summary

Long homogenization holding times are commonly applied for standard ingot-cast materials due to Cu segregation and coarse primary phases at the boundaries of extensive eutectic cells. Even current literature on Al-Cu-Li-based twin-roll cast strips applies homogenization holding times exceeding six hours [130] because such homogenization conditions are commonly applied to TRC strips of other systems [90,184-186]. Simulation and optimization of TRC materials performed in the present study reveal that these holding times can be reduced by an order of magnitude (below one hour). Moreover, multi-step annealing at lower temperatures facilitates the formation of sufficiently effective grain refining $Al_3(Sc,Zr)$ dispersoids, which agrees with previous experiments on Al-Mg-Sc-Zr-based materials [163]. Once these dispersoids are formed, a plastic deformation step can be inserted to modify the grain size distribution and texture (SR, AR, CGP). A final homogenization annealing and solution treatment can be significantly shortened and combined into a single step, thus limiting the risk of surface Li evaporation and $Al_3(Sc,Zr)$ dispersoid coarsening. The only constituents that remain after the model standardization are transformed complex Al_7Cu_2Fe phase precipitates. This phase is expected in Al wrought alloys due to the presence of Fe as an impurity [100,187,188]. The accumulation of stress near the phase increases the likelihood of crack initiation. Its presence can never be excluded but can be suppressed using higher-purity input materials in the aerospace industry.

The opportunity to improve mechanical properties by deformation-induced strengthening and grain structure optimization is limited in TRC alloys because of their near-net shape in the as-cast state. An improvement in ductility is the primary focus of the deformation-induced microstructural changes. Applying the AR and standard SR improves the ductility of TRC materials, especially in alloy A, where the rolling-induced <110> texture is retained after standardization. However, the ductilities achieved by rolling are still lower than those of standard AA2195 materials. Additionally, both rolling methods require further thickness reductions and are associated with similar drawbacks induced by rolling in standard AA2195 materials. As proposed in this study, a further ductility increase can be achieved by applying highly progressive SPD methods, such as CGP. CGP eliminates the negative <100> texture in standardized alloy B and induces a highly beneficial <111> texture in alloy A. This beneficial texture leads to the TSc 3CGP material in the T8 temper having ductility better than 10 %, comparable to standard AA2195 alloys. The role of Sc is decisive since it is the only element capable of preventing grain coarsening during high-temperature thermomechanical processing.

The individual contributions to the total strength were calculated for the TRC materials. The contribution of the strengthening T_1 phase is crucial and depends on its homogeneous distribution in the grain structure modified by CGP and the beneficial effect of $Al_3(Sc,Zr)$ dispersoids. Additionally, the dispersion of this phase is improved by a dense dislocation network induced by the pre-deformation step after standardization, suppressing the precipitation of the θ' phase in the matrix.

6. Conclusion

The approaches of physical metallurgy were used to identify the processes controlling the formation of cast and post-processed structures in Al-Cu-Li-Mg-Zr-(Sc)-based materials.

- The relation between the inhomogeneous distribution of solutes (size of eutectic cells) and solidification rate was identified in the 0.1 K·s^{-1} to 10^8 K·s^{-1} range. Solidification rates below 10^7 K·s^{-1} lead to a formation of eutectic cells with sizes ranging from 1 μm for the rapidly solidified melt-spun alloys, through 10 μm for the TRC materials, and above 100 μm in the ingot-cast materials. Higher solidification rates achieved in contact areas of the melt-spun strips lead to near-diffusionless solidification and the formation of supersaturated columnar grains by cellular growth. Near-diffusionless solidification leads to a sharp deviation from power laws established for the materials formed by eutectic growth.
- Diffusion models predict the dependence of homogenization holding times on the size of the eutectic cells as 1/ECS^2. The calculated values range from 10 s for the melt-spun strips, through 25 min for the TRC materials, to 32 h in the ingot-cast materials. The high solidification rate of TRC provides sufficient refinement of the cast structure to combine homogenization and solution treatment into a single 530 °C/30 min annealing step.
- A constrained groove pressing before the final standardization step breaks up the inhomogeneity of grain size distribution and the undesirable texture imparted by TRC, which limits the ductility of the material.
- The role of $Al_3(Sc,Zr)$ precipitates formed during intermediary annealing (300 °C/30 min, 450 °C/30 min) is crucial in stabilizing textures in the deformed TRC materials, preventing the coarsening of grains and preventing the formation of undesirable <100> textures typical for recrystallized rolled materials.
- Identifying and analyzing particular contributions to the total strength of peak-aged TRC alloys and their extending to higher concentrations of alloying elements validates the use of Sc in this type of alloy and the superiority of the proposed near-net-shaped processing route in comparison with standard AA2195 materials prepared by a standard ingot-cast technology.

References

[1] KERRY, J. (2012) Aluminum foil packaging. *Packaging Technology, Fundamentals, Materials, and Processes* 163-177. ISBN: 978-1-84569-665-8.

[2] HATCH, J. E. (1984) *Aluminum: Physical properties and metallurgy*. American Society for Metals. Metals Park, OH. ISBN: 9780871701763.

[3] NING, H., LI, J., MA, P., CHEN, Y., ZHANG, X., ZHANG, K., ZHANG, R. (2020). Evolution of aging precipitates in an Al–Li alloy with 1.5 wt% Li concentration. *Vacuum,* **182**, 109677.

[4] RIOJA, R. J, LIU, J. (2012). The Evolution of Al-Li Base Products for Aerospace and Space Applications. *Metallurgical and Materials Transactions A,* **43**, 3325-3337.

[5] LAVERNIA, E. J., GRANT, N. J. (1987). Aluminium-lithium alloys. *Journal of Materials Science,* **22**, 1521-1589.

[6] GRUSHKO, O., OVCHINNIKOV, V. OVYSANNIKOV, B. (2016). *Aluminum-Lithium Alloys: Process Metallurgy, Physical Metallurgy, and Welding*. Boca Raton: CRC Press. ISBN: 9781498737173

[7] KUMAR, K. S., HEUBAUM, F. H. (1997). THE EFFECT OF Li CONTENT ON THE NATURAL AGING RESPONSE OF Al-Cu-Li-Mg-Ag-Zr ALLOYS. *Acta Metallurgica,* **45**, 2317-2327.

[8] GABLE, B. M., ZHU, A. W., CSONTOS, A. A., STARKE, E. A. (2001). The role of plastic deformation on the competitive microstructural evolution and mechanical properties of a novel Al–Li–Cu–X alloy. *Journal of Light Metals,* **1**, 1-14.

[9] GASIOR, W., MOSER, Z. (2002). Chemical diffusion coefficients in solid Al-Li alloys at low Li concentrations. *Scandinavian Journal of Metallurgy,* **31**, 353-358.

[10] KURIYAMA, K., MASAKI, N. (1975). The crystal structure of AlLi. *Acta Crystallographica,* **B31**, 1793, 1975.

[11] WILLIAMS, D. B., EDINGTON, J. W. (1976). The discontinuous precipitation reaction in dilute Al-Li alloys. *Acta Metallurgica,* **24**, 323-332.

[12] OKAMOTO, H. (2012). Al-Li (Aluminum-Lithium). *Journal of Phase Equilibria and Diffusion,* **33**, 500-501.

[13] GUINIER, A. (1959). Heterogeneities in Solid Solutions. *Solid State Physics,* **9**, 293-398.

[14] GORNOSTYREV, Y. N., KATSNELSON, M. I. (2015).Misfit stabilized embedded nanoparticles in metallic alloys. *Physical Chemistry Chemical Physics,* **17**, 27249-27257.

[15] ELSAYED, M., IBRAHIM, A. M., STAAB, T. E. M. (2021). A new perspective on the precipitation sequence in a high-purity Al-1.74 at.% Cu alloy by employing positron annihilation spectroscopy: experiment and theory. *Journal of Physics of Condensed Matter,* **33**, 435401.

[16] DECREUS, B., DESCHAMPS, A., DE GEUSSER, F., DONNADIEU, P., SIGLI, C., WEYLAND, M. (2013). The influence of Cu/Li ratio on precipitation in Al–Cu–Li–x alloys. *Acta Materialia,* **61**, 2207-2218.

[17] WANG, S. C., STARINK, M. J. (2005). Precipitates and intermetallic phases in precipitation hardening Al–Cu–Mg–(Li) based alloys. *International Materials Reviews,* **50**, 193-215.

[18] WOLVERTON, C. (2000). First principles theory of 250000-atom coherent alloy microstructure. *Modelling and Simulation in Materials Science and Engineering,* **8**, 323-333.

[19] KONNO, T. J., KAWASAKI, M., HIRAKA, K. (2009). Guinier-Preston zones observed by high-angle annular detector dark-field scanning transmission electron microscopy. *Philosophical Magazine B,* **81**, 1713-1724.

[20] WOLVERTON, C. (1999). First-principles prediction of equilibrium precipitate shapes in Al-Cu alloys. *Philosophical Magazine Letters,* **79**, 683-690.

[21] WOLVERTON, C., OZOLINŠ, V. (2001). Entropically Favored Ordering: The Metallurgy of Al2Cu Revisited. *Physical Review Letters,* **86**, 5518-5521.

[22] SILCOCK, J. M., TEAL, T. J., HARDY, H. K. (1954). STRUCTURAL AGEING CHARACTERISTICS OF BINARY ALUMINIUM-COPPER ALLOYS. *Journal of the Institute of Metals,* **82**, 239-248.

[23] MOKHTARI, O., KIM, M.-S., NISHIKAWA, H., KAWASHIRO, F. (2014). Investigation of Formation and Growth Behavior of Cu/Al Intermetallic Compounds during Isothermal Aging. *Transactions of The Japan Institute of Electronics Packaging,* **7**, 1-7.

[24] BAHL, S., XIONG, L., ALLARD, L. F., MICHI, R. A., POPLAWSKY, J. D., CHUANG, A. C., SINGH, D., WATKINS, T. R., SHIN, D., HAYNES, J. A., SHYAM, A. (2021). Aging behavior and strengthening mechanisms of coarsening resistant metastable θ' precipitates in an Al–Cu alloy. *Materials and Design,* **198**, 109378.

[25] GAYLE, F. W., GOODWAY, M. (1994). Precipitation Hardening in the First Aerospace Aluminum Alloy: The Wright Flyer Crankcase. *Science,* **266**, 1015-1017.

[26] QIU, R., LU, H., AO, B., HUANG, L., TANG, T., CHEN, P. (2017). Energetics of point defects in aluminum via orbital-free density functional theory. *Philosophical magazine,* **97**, 2164-2181.

[27] TZANETAKIS, P., HILLAIRET, J., REVEL, G. (1976). The Formation

Energy of Vacancies in Aluminium and Magnesium. *Physica Status Solidi B,* **75**, 433-439.

[28] CZERWINSKI, F. (2020). Thermal Stability of Aluminum Alloys. *Materials,* **13**, 3441.

[29] VAN SMAALEN, S., BRONSWELD, P., DE BOER, J. L. (1990).Refinement of the crystal structure of hexagonal Al2CuLi. *Journal of Solid State Chemistry,* **85**, 293-298.

[30] DONNADIEU, P., SHAO, Y., DE HEUSSER, F., BOTTON, G. A., LAZAR, S., CHEYNET, M., DE BOISSIEU, M., DESCHAMPS, A. (2011). Atomic structure of T1 precipitates in Al–Li–Cu alloys revisited with HAADF-STEM imaging and small-angle X-ray scattering. *Acta Materialia,* **59**, 462-472.

[31] CASSADA, W. A., SHIFLET, G. J., STARKE, E. A. (1991) Mechanism of AI2CuLi (T1) Nucleation and Growth. *METALLURGICAL TRANSACTIONS A,* **22**, 287-297.

[32] SCHULTHESS, T. C., TURCHI, P. E. A., GONIS, A., NIEH, T. G. (1998). Systematic study of stacking fault energies of random Al-based alloys. *Acta Materialia,* **46**, 2215-2221.

[33] MANG, X. J. J. (2018). Effects of Precipitation of Al 3Zr Particles on Microstructures and Properties of the Al-3.55Cu-1.51Li-0.11Zr Alloy. *Materials Science Forum,* **921**, 214-221.

[34] NES, E., RYUM, N., HUNDERI, O. (1985). On the Zener drag. *Acta Metallurgica,* **33**, 11-22.

[35] DORIN, T., DESCHAMPS, A., DE GEUSSER, F., SIGLI, C. (2014). Quantification and modelling of the microstructure/strength relationship by tailoring the morphological parameters of the T1 phase in an Al–Cu–Li alloy. *Acta Materialia,* **75**, 134-146.

[36] KNIPLING, K. E., DUNAND, D. C., SEIDMAN, N. (2007). Nucleation and Precipitation Strengthening in Dilute Al-Ti and Al-Zr Alloys. *Metallurgical and Materials Transactions A,* **38**, 2552-2563.

[37] JIA, Z., COUZINIE, J., CHERDOUDI, N., GUILLOT, I., ARNBERG, L., ASHOLT, P., BRUSETHAUG, S., BARLAS, B., MASSINON, D. (2012). Precipitation behaviour of Al3Zr precipitate in Al−Cu−Zr and Al−Cu−Zr−Ti−V alloys. *Transactions of Nonferrous Metals Society of China,* **22**, 1860-1865.

[38] RYUM, N. (1969). Precipitation and recrystallization in an Al-0.5 WT.% Zr-alloy,“ *Acta Metallurgica,* **17**, 269-278.

[39] CLOUET, E., NASTAR, M., SIGIL, C. (2004). Nucleation of Al3Zr and Al3Sc in aluminum alloys: From kinetic Monte Carlo simulations to classical theory. *Physical Review B,* **69**, 064109.

[40] CLOUET, E., SANCHEZ, J. M., SIGIL, C. (2002). First-principles study of the solubility of Zr in Al. *Physical Review B,* **65**, 094105.

[41] ROBSON, J., PRAGNELL, P. B. (2001). Dispersoid precipitation and process modelling in zirconium containing commercial aluminium alloys. *Acta Materialia,* **49**, 599-613.

[42] JIA, Z., HU, G., FORBOD, B., SOLBERG, J. K. (2008). Ehancement of recrystallization resistance of Al-Zr-Mn by two-step precipitation annealing. *Materials Science and Engineering: A,* **483**, 195-198.

[43] SATO, T., KAMIO, A., LORIMER, G. (1996). Effects of Si and Ti additions on the nucleation and phase stability of the L12-type Al3Zr phase in Al-Zr alloys. *Materials Science Forum,* **222**, 895-900.

[44] YOSHIDA, H., BABA, Y. (1982). The Role of Zirconium to Improve Strength and Stress-corrosion Resistance of Al–Zn–Mg and Al–Zn–Mg–Cu Alloys. *Transactions of the Japan Institute of Metals,* **23**, 620-630.

[45] SMITH, C. S. (1948). Introduction to grains, phases, and interfaces – an interpretation of microstructure. *Transactions of the International Society of AIME,* **175**, 15-51.

[46] GARLBRAITH, J. M., TOSTEN, M. H., HOWELL, P. R. (1987). On the nucleation of theta' and T1 on AI3Zr precipitates in AI-Li-Cu-Zr alloys. *Journal of Materials Science,* **22**, 27-36.

[47] TIAN, S., LI, J., ZHANG, Z., ZHUMABIEKE, W., DAN, L. (2019). Effect of Zr and Sc on microstructure and properties of 7136 aluminum alloy. *Journal of Materials Research and Technology,* **8**, 4130-4140.

[48] ROYSET, J., RYUM, N. (2005). Scandium in Aluminium Alloys. *International Materials Review,* **50**, 19-44.

[49] SCHEVCHENKO, M. O., KUDIN, V. G., BEREZUTSKII, V. V., IVANOV, M. I., SUDAVTSOVA, V. S. (2014). Thermodynamic Properties of Al–Sc Alloys. *Powder Metallurgy and Metal Ceramics volume,* **53**, 234-239.

[50] DRITS, M. E., KADANER, E. S., NGUEN, D. S. (1973). Character of Interaction between Scandium and Aluminum in the Al-Rich Portion of the Al-Sc System. *Izv. Akad. Nauk SSSR, Met.,* **4**, 213-217.

[51] MURRAY, J. (1998). The Al-Sc (aluminum-scandium) system. *Journal of Phase Equilibria,* **19**, 380.

[52] ROBSON, J. D., JONES, M. J., PRAGNELL, P. B. (2003). Extension of the N-model to Predict Competing Homogeneous and Heterogeneous Precipitation in Al-Sc Alloys. *Acta Materiallia,* **51**, 1453-1468.

[53] FUJIKAVA, S., SUGAYA, M., TAKEI, H., HIRANO, K. (1979). Solid solubility and residual resistivity of scandium in aluminum. *Journal of the Less Common Metals,* **63**, 87-97.

[54] DORIN, T., RAMAJAYAM, M., VAHID, A., LANGAN, T. (2018). *Fundamentals of Aluminum Metallurgy: Aluminum Scandium alloys*, Elsevier Ltd., Amsterdam, *439-494*. ISBN: 978-0-08-102063-0.

[55] DAVYDOV, V. G., ROSTOVA, T. D., ZAKHAROV, V., FILATOV, Y. A., YELAGIN, V. I. (2000). Scientific principles of making an alloying addition of scandium to aluminium alloys. *Materials Science and Engineering: A*, **280**, 30-36.

[56] CLOUET, E., LAE, L., EPICIER, T., LEFEBVRE, W., NASTAR, M., DESCHAMPS, A. (2006). Complex precipitation pathways in multicomponent alloys. *Nature Materials,* **5**, 482-488.

[57] BAGARYATSKY, Y. A. (1952). Structural changes on aging Al-Cu-Mg alloys. *Proceedings of the USSR Academy of Sciences ,* **87**, 397-401.

[58] SILCOCK, J. M. (1961). The structural ageing characteristics of Al-Cu-Mg alloys with copper-magnesium weight ratios of 7-1 and 2.2-1. *Journal of the Institute of Metals,* **89**, 203-210.

[59] PERLITZ, H., WESTGREN, A. (1942). The crystal structure of Al8Si6Mg3Fe. *Arkiv för kemi, mineralogi och geologi,* **16**.

[60] KILAAS, R., RADMILOVIC, V. (2001). Structure determination and structure refinement of Al2CuMg precipitates by quantitative high-resolution electron microscopy. *Ultramicroscopy,* **88**, 63-72.

[61] WOLVERTON, C. (2001). Crystal structure and stability of complex precipitate phases in Al–Cu–Mg–(Si) and Al–Zn–Mg alloys. *Acta Materialia,* **49**, 3129-3142.

[62] WANG, S. C., STARINK, M. J. (2004). The assessment of GPB2/S″ structures in Al–Cu–Mg alloys. *Materials Science and Engineering: A,* **386**, 156-163.

[63] GAO, N., DAVIN, L., WANG, S., CEREZO, A., STARINK, M. J. (2002). Precipitation in stretched Al-Cu-Mg alloys with reduced alloying content studied by DSC, TEM and atom probe. *Materials Science forum,* **402**, 923-928.

[64] CHARAI, A., WALTHER, T., ALFONSO, C., ZAHRA, A. M., ZAHRA, C. Y. (2000). Coexistence of clusters, GPB zones, S″-, S′- and S-phases in an Al–0.9% Cu–1.4% Mg alloy. *Acta Materialia,* **48**, 2751-2764.

[65] WYSS, R. K., SANDERS, R. E. J. (1988). Microstructure-property relationship in a 2xxx aluminum alloy with mg addition. *Metallurgical Transactions A,* **19**, 2523-2530.

[66] HUANG, B. P., ZHENG, Z. Q. (1998). Independent and combined roles of trace Mg and Ag additions in properties precipitation process and precipitation kinetics of Al–Cu–Li–(Mg)–(Ag)–Zr–Ti alloys. *Acta Materialia,* **46**, 4381-4393.

[67] GARG, A., HOWE, J. M. (1991). Convergent-beam electron diffraction analysis of the Ω phase in an Al-4.0 Cu-0.5 Mg-0.5 Ag alloy. *Acta*

Metallurgica et Materialia, **39**, 1939-1946.

[68] HAO, M., WANG, L., CHEN, J. Z., LI, G. A. (2021). Intrinsic Fatigue Crack Growth in Al-Cu-Li-Mg-Zr Alloys: The Effect of the Iron Constituent Particles. *Metals,* **11**, 110.

[69] XU, X., HAO, M., CHEN, J., HE, W., LI, G., LI, K., JIAO, C., ZHONG, X. L., MOORE, K. L., BURNETT, T. L., ZHOU, X. (2022). Role of constituent intermetallic phases and precipitates in initiation and propagation of intergranular corrosion of an Al-Li-Cu-Mg alloy. *Corrosion Science,* **201**, 110294.

[70] MUKHOPADHYAY, A. K., ZHOU, D. S., YANG, Q. B. (1992). Effect of variation in the Cu:Mg ratios on the formation of T2 and C phases in AA 8090 alloys. *Scripta Metallurgica et Materialia,* **26**, 237-242.

[71] AUDIER, M., JANOT, C., DE BOSSIEU, M., DUBOST, B. (1989). Structural relationships in intermetallic compounds of the Al-Li-(Cu, Mg, Zn) system. *Philosophical Magazine B,* **60**, 437-466.

[72] WANG, S. C., LI, C. Z., YAN, M. G. (1994). A transmission-electron-microscopy study of a face-centred-cubic phase in an Al-Li-Cu-Mg-Zr alloy. *Journal of Materials Science ,* **29**, 384-388.

[73] NADELLA, R., ESKIN, D. G., DU, Q., KATGERMAN, L. (2008). Macrosegregation in direct-chill casting of aluminium alloys. *Progress in Materials Science,* **53**, 421-480.

[74] ZALOŽNIK, M., ŠARLER, B. (2005). Modeling of macrosegregation in direct-chill casting of aluminum alloys: Estimating the influence of casting parameters. *Materials Science and Engineering: A,* **414**, 85-91.

[75] DU, Q., ESKIN, D. G., KARGERMAN, L. (2007). Modeling Macrosegregation during Direct-Chill Casting of Multicomponent Aluminum Alloys. *Metallurgical and Materials Transactions A,* **38**, 180-189.

[76] GUO, G., YAO, T., LIU, W., TANG, S., XIAO, D., HUANG, L., WU, L., FENG, Z., GAO, X. (2024). Numerical Simulation and Machine Learning Prediction of the Direct Chill Casting Process of Large-Scale Aluminum Ingots. *Materials,* **17**, 1409.

[77] HEKMAT-ARDAKAN, A., ELGALLAD, E. M., AJERSCH, F., CHEN, X. G. (2012). Microstructural evolution and mechanical properties of as-cast and T6-treated AA2195 DC cast alloy. *Materials Science and Engineering: A,* **558**, 76-81.

[78] SURESH, M., SHARMA, A., MORE, A. M., KALSAR, R., BISHT, A., NAYAN, N., SUWAS, S. (2019). Effect of equal channel angular pressing (ECAP) on the evolution of texture, microstructure and mechanical properties in the Al-Cu-Li alloy AA2195. *Journal of Alloys and compounds,* **785**, 972-983.

[79] SURESH, M., SHARMA, A., MORE, A. M., NAYAN, N., SUWAS, S. (2018). Effect of Scandium addition on evolution of microstructure, texture and mechanical properties of thermo-mechanically processed Al-Li alloy AA2195. *Journal of Alloys and Compounds,* **740**, 364-374.

[80] SLAMOVA, M., KARLIK, M., ROBAUT, F., SLAMA, P., VERON, M. (2003). Differences in microstructure and texture of Al–Mg sheets produced by twin-roll continuous casting and by direct-chill casting. *Materials Characterization,* **49**, 231-240.

[81] BAREKAR, N. S., DHINDAW, B. K. (2014). Twin-Roll Casting of Aluminum Alloys – An Overview. *Materials and Manufacturing Processes,* **29**, 651-661.

[82] COOK, R., GROCOCK, P. G., THOMAS, P. M., EDMONDS, D. V., HUNT, J. D. (1995). Development of the twin-roll casting process. *Journal of Materials Processing Technology,* **55**, 76-84.

[83] HAGA, T., INUI, H., WATARI, H., KUMAI, S. (2007). Casting of Al–Si hypereutectic aluminum alloy strip using an unequal diameter twin roll caster. *Journal of Materials Processing Technology,* **191**, 238-241.

[84] MERCHANT, H. D., KATTAMIS, T. Z., MORRIS, J. G. (1989). Continuous casting of non ferrous metals and alloys. *TMS conference proceedings,* 1-66.

[85] FERRY, M. (2006). Direct strip casting of metals and alloys, Cambridge, England: Woodhead publishing limited, 2006. ISBN: 978-1-84569-049-6.

[86] ESKIN, D., DU, Q., RUVALCABA, D., KATGERMAN, L. (2005) Experimental study of structure formation in binary Al–Cu alloys at different cooling rates. *Materials Science and Engineering: A,* **405**, 1-10.

[87] LI, S., HE, C., FU, J., XU, J., XU, G., WANG, Z. (2020). Evolution of microstructure and properties of novel aluminum-lithium alloy with different roll casting process parameters during twin-roll casting. *Materials Characterization,* **161**, 110145.

[88] HADADZADEH, A., WELLS, M. A. (2013). Thermal fluid mathematical modelling of twin roll casting (TRC) process for AZ31 magnesium alloy. *International Journal of Cast Metals research,* **26**, 228-238.

[89] DAS, S., LIM, N. S., KIM, H. W., PARK, C. G. (2011). Effect of rolling speed on microstructure and age-hardening behaviour of Al–Mg–Si alloy produced by twin roll casting process. *Materials and Design,* **32**, 4603-4607.

[90] BIROL, Y. (2007). The performance of Al–Ti–C grain refiners in twin-roll casting of aluminum foilstock. *Journa of alloys and compounds,* **430**, 179-187.

[91] YUN, M., LOCKYER, S. A., HUNT, J. D., COOK, R., BRISTOW, D. J. (2000). A study of TiCAl 315™ grain refinement in roll cast AA8111 aluminum alloy. *Light Metals,* 857-864.

[92] DUWEZ, P., WILLIENS, R. H., KLEMENT, W. (1960). Continuous series of Metastable Solid Solutions in Silver-Copper Alloys. *Journal of Applied Physics,* **31**, 1136.

[93] VEGARD, L. (1921).Die Konstitution der Mischkristalle und die Raumfüllung der Atome. *Zeitschrift für Physik,* **5**, 17-26.

[94] GUSAKOVA, O., SHEPELEVICH, V., ALEXANDROV, D. V., STARODUMOV, I. O. (2020). Formation of the microstructure of rapidly solidified hypoeutectic Al-Si alloy. *The European Physical Journal Special Topics,* **229**, 417-425.

[95] GRYDIN, O., GARTHE, K. U., YUAN, X., BROER, J., KESSLER, O., KRÁLÍK, R., CIESLAR, M., SCHAPER, M. (2023). Numerical and Experimental Investigation of Twin-Roll Casting of Aluminum–Lithium Strips. *Light metals*, 1031-1037.

[96] GUSAKOVA, O. (2023). Chemically partitionless crystallization in near-eutectic rapidly solidified Al–12, 6Si–0, 8Mg–0, 4Mn–0, 7Fe–0, 9Ni–1, 8Cu alloy *The European Physical Journal Special Topics,* **232**, 1281-1291.

[97] CHUANBING, R., BAOGEN, S. (2018). Nanocrystalline and nanocomposite permanent magnets by melt spinning technique. *Chinese Physics B,* **27**, 117502.

[98] GUO, S., LIU, Y. (2012). Estimation of critical cooling rates for formation of amorphous alloys from critical size. *Journal of Non-crystalline solids,* **358**, 2753-2758.

[99] DORIN, T., VAHID, A., JAMB, J. (2018). *Fundamentals of Aluminum Metallurgy: Aluminum Lithium alloys*, Amsterdam: Elsevier Ltd., 387-438. ISBN: 978-0-08-102063-0.

[100] JIANG, N., GAO, X., ZHENG, Z. (2010). Microstructure evolution of aluminum-lithium alloy 2195 undergoing commercial production. *Transactions of Nonferrous Metals Society of China,* **20**, 740-745.

[101] DENG, Y., XU, J., CHEN, J., GUO, X. (2020). Effect of double-step homogenization treatments on the microstructure and mechanical properties of Al–Cu–Li–Zr alloy. *Materials Science and Engineering: A,* **795**, p. 139975

[102] LIU, Q., ZHU, R., LI, J. F., CHEN, Y. L., ZHANG, X. H., ZHANG, L., ZHENG, Z. (2016). Microstructural evolution of Mg, Ag and Zn micro-alloyed Al–Cu–Li alloy during homogenization. *Transactions of Nonferrous Metals Society of China,* **26**, 607-619.

[103] TSIVOULAS, D., ROBSON, J. D. (2015). Heterogeneous Zr solute segregation and Al3Zr dispersoid distributions in Al–Cu–Li alloys. *Acta Materialia,* **93**, 73-86.

[104] YANG, S., SHEN, J., YAN, X., LI, X., FEI, Z., SUN, B. (2017). Homogenization Treatment Parameter Optimization and Microstructural

Evolution of Al-Cu-Li Alloy. *Rare Metal Materials and Engineering,* **46**, 28-34.

[105] YU, H., JIN, L., HU, L., WANG, Y. (2020). Mechanical properties of the solution treated and quenched Al–Cu–Li alloy (AA2195) sheet during high strain rate deformation at room temperature. *Materials Science and Engineering: A,* **793**, 139880.

[106] KIM, J.-H., JEUN, J. H., CHUN, H. J., LEE, Y. R., TOO, J. T., YOON, Y. H., LEE, H. S. (2016). Effect of precipitates on mechanical properties of AA2195. *Journal of Alloys and Compounds,* **669**, 187-198.

[107] WALKER, W., MARLOTH, R., HEIN, Y. T., ES-SAID, O. S. (2019). The Effect of Incomplete Solution Treatment on the Tensile Behavior and Mechanical Anisotropy of 2195 Aluminum Lithium Alloy. *Diffusion foundations,* **22**, 109-117.

[108] DUAN, S., GUO, F., ZHANG, Y., CHONG, K., LEE, S., MATSUDA, K., ZOU, Y. (2021). Effects of texture and precipitates characteristics on anisotropic hardness evolution during artificial aging for an Al–Cu–Li alloy. *Materials and Design,* **212**, 110216.

[109] MA, P., ZHAN, L., LIU, C., WANG, Q., LI, H., LIU, D., HU, Z. (2019). Pre-strain-dependent natural ageing and its effect on subsequent artificial ageing of an Al-Cu-Li alloy. *Journal of Alloys and Compounds,* **790**, 8-19.

[110] CSONTOS, A. A., STARKE, E. A. (2000). The effect of processing and microstructure development on the slip and fracture behavior of the 2.1 wt pct Li AF/C-489 and 1.8 wt pct Li AF/C-458 Al-Li-Cu-X alloys. *Metallurgical and Materials Transactions: A,* **31**, 1965-1976.

[111] SUN, J., SONG, M., HE, Y. (2010). Effects of Sc content on the mechanical properties of Al-Sc alloys. *Rare Metals,* **29**, 451-455.

[112] DORIN, T., JIANG, L., LANGAN, T. (2023). Formation of Al3Sc Dispersoids and Associated Strengthening. *Light Metals,* 1207-1212.

[113] MARQUIS, E. A., SEIDMAN, D. N. (2001). NANOSCALE STRUCTURAL EVOLUTION OF Al3Sc PRECIPITATES IN Al(Sc) ALLOYS. *Acta Materialia,* **49**, 1909-1919.

[114] AHMAD, Z. (2003). The properties and application of scandium-reinforced aluminum. *JOM,* **55**, 35-39.

[115] ZAKHAROV, V. V., FILATOV, Y. A., FISENKO, I . A. (2020). SCANDIUM ALLOYING OF ALUMINUM ALLOYS. *Metal Science and Heat treatment,* **62**, 31-36.

[116] PARKER, B. A., ZHOU, Z. F., NOLLE, P. (1997). The effect of small additions of scandium on the properties of aluminium alloys. *Journal of Materials Science,* **30**, 452-458.

[117] ZAKHAROV, V. V., ROSTOVA, T. D. (1995). ON THE POSSIBILITY OF SCANDIUM ALLOYING OF COPPER-CONTAINING ALUMINUM ALLOYS. *Metal Science and Heat Treatment,* **37**, 65-69.

[118] DE POTTEY, A., JIANG, L., DORIN, T., WOOD, T., LANGAN, T. SANDERS, P. (2023). Effect of Cooling Rate on W-Phase Formation in Al-Cu-Sc Alloys. *Light Metals,* 1238-1245.

[119] MORRISON, C. B., DUNAND, D. C., SEIDMAN, D. N. (2011). Coarsening resistance at 400 °C of precipitation-strengthened Al–Zr–Sc–Er alloys. *Acta Materialia,* **59**, 7029-7042.

[120] MARQUIS, E. A., SEDIMAN, D. N. (2002). A Subnanoscale Study of Mg Segregation at Al/Al3Sc Interfaces. *Microscopy and Microanalysis,* **8**, 1100-1101.

[121] CHEN, B. A., LIU, G., WANG, R. H., ZHANG, Y., LIANG, L., SONG, J. J., SUN, J. (2013). Effect of interfacial solute segregation on ductile fracture of Al–Cu–Sc alloys. *Acta Materialia,* **61**, 1676-1690.

[122] YU, K., LI, W., LI, S., ZHAO, J. (2004). Mechanical properties and microstructure of aluminum alloy 2618 with Al3(Sc, Zr) phases. *Materials Science and Engineering: A,* **368**, 88-93.

[123] JIANG, B., YI, D., YI, X., ZHENG, F., WANG, H., WANG, B., LIU, H., HU, Z. (2018). Effect of trace amounts of added Sc on microstructure and mechanical properties of 2055 aluminum alloy. *Materials Characterization,* **141**, 248-259.

[124] ZHANG, J., WU, G., ZHANG, L., ZHANG, X., SHI, C., TONG, X. (2022). Addressing the strength-ductility trade-off in a cast Al-Li-Cu alloy—Synergistic effect of Sc-alloying and optimized artificial ageing scheme. *Journal of Materials Science and Technology,* **96**, 212-225.

[125] LIANG, L., KI, J. K., CHENG, P. M., LIU, G., WANG, R. H., CHEN, B. A., ZHANG, J. Y., SUN, J., YANG, M. X., YANG, G. (2014). Experiment and modeling of ultrafast precipitation in an ultrafine-grained Al–Cu–Sc alloy. *Materials Science and Engineering: A,* **607**, 596-604.

[126] JINDAL, V., DE, P. K., VENKATESWARLU, K. (2006). Effect of Al3Sc precipitates on the work hardening behavior of aluminum–scandium alloys. *Materials Letters,* **60**, 3373-3375.

[127] YIN, Z., PAN, Q., ZHANG, Y., JIANG, F. (2000). Effect of minor Sc and Zr on the microstructure and mechanical properties of Al–Mg based alloys. *Materials Science and Engineering: A,* **280**, 151-155.

[128] NOVIKOV, I., GRUSHKO, O. E. (1995). Hot cracking susceptibility of AI-Cu-Li and AI-Cu-Li-Mn alloys. *Materials Science and Technology,* **11**, 926-932.

[129] BELOV, N. A., ALABIN, A. N., ESKIN, D. G., ISTOMIN-KASTROVSKII,

V. V. (2006). Optimization of hardening of Al–Zr–Sc cast alloys. *Journal of Materials Science,* **41**, 5890-5899.

[130] LI, S., WEI, B., YU, C., LI, Y., XU, G., LI, Y. (2020). Evolution of microstructure and properties during homogenization of the novel Al–Li alloy fabricated by electromagnetic oscillation twin-roll casting. *Journal of Materials Research and Technology,* **9**, 3304-3317.

[131] LI, S., JIANG, T., WANG, J., CHEN, L., WEI, B., LI, Y., XU, G., WANG, Z. (2019). Effects of different external fields on the microstructure and mechanical properties of novel Alsingle bondCusingle bondLi alloy during twin-roll casting. *Materials Science and Engineering: A,* **757**, 14-22.

[132] GUO, Y. J., LI, J. F., LU, D. D., DENG, S. X., MA, Y. L., YOU, W., CHEN, Y. L., ZHANG, X. H., ZHANG, R. F. (2021). Characterization of Al3Zr precipitation via double-step homogenization and recrystallization behavior after subsequent de-formation in 2195 Al-Li alloy. *Materials Characterization,* **182**, 111549.

[133] YE, F., MAO, L., RONG, J., ZHANG, B., WEI, L., WEN, S., JIAO, H., WU, S. (2022). Influence of different rolling processes on microstructure and strength of the Al–Cu–Li alloy AA2195. *Progress in Natural Science: Materials International,* **32**, 87-95.

[134] JIN, Y., HU, Y. (2022). Enhanced formability and hardness of AA2195-T6 during electromagnetic forming. *Journal of Alloys and Compounds,* **890**, 161891.

[135] VINCZE, G., SIMOES, F. J. P., BUTUC, M. C. (2020). Asymmetrical Rolling of Aluminum Alloys and Steels: A Review. *Metals,* **10**, 1126.

[136] LI, L., MATSUMOTO, R., UTSUNOMIYA, H. (2019). Curling of Sheet in Asymmetric Rolling Investigated by Profile Measurement of Partly Rolled Sheet. *ISIJ International,* **59**, 489-495.

[137] KIM, K. H., LEE, D. N. (2001). Analysis of deformation textures of asymmetrically rolled aluminum sheets. *Acta Materialia,* **49**, 2583-2595.

[138] SIMOES, F. P., ALVES DE SOUSA, R., GRACIO, J. J. A., BARLAT, F., YOON, J. W. (2009). Effect of asymmetrical rolling and annealing the mechanical response of an 1050-o sheet. *International Journal of Material Forming,* **2**, 891-894.

[139] SHIN, D. H., PARK, J. J., KIM, Y. S., PARK, K. T. (2002). Constrained groove pressing and its application to grain refinement of aluminum. *Materials Science and Engineering: A,* **328**, 98-103.

[140] SURAJ, P. (2021). CONSTRAINED GROOVE PRESSING: A REVIEW. *Metallurgy and Materials,* **27**, 96-106.

[141] GUPTA, A. K., MADDUKURI, T. S., SINGH, S. K. (2016). Constrained groove pressing for sheet metal processing. *Progress in Materials Science,* **84**,

403-462.

[142] WANG, Z. S., GUAN, Y. J., WANG, G. C., ZHONG, C. K. (2015). Influences of die structure on constrained groove pressing of commercially pure Ni sheets. *Journal of Materials Processing Technology,* **215**, 205-218.

[143] ASGARI, M., HONARPISHEH, M., AMINI, S., MANSOURI, H. (2020). Investigation of Residual Stress in the Ultrasonic Assisted Constraint Groove Pressing Process of Copper Sheets. *Journal of Stress Analysis,* **4**, 107-114.

[144] ZRNIK, A., KOVARIK, T., NOVY, Z., CIESLAR, M. (2009). Ultrafine-grained structure development and deformation behavior of aluminium processed by constrained groove pressing. *Materials Science and Engineering: A,* **503**, 126-129.

[145] HOSSEINI, E., KAZEMINEZHAD, M. (2010). Integration of physically based models into FE analysis: Homogeneity of copper sheets under large plastic deformations. *Computational Materials Science,* **48**, 166-173.

[146] HOSSEINI, E., KAZEMINEZHAD, M. (2011). A new microstructural model based on dislocation generation and consumption mechanisms through severe plastic deformation. *Computational Materials Science,* **50**, 1123-1135.

[147] UL-HAMID, A. (2018). Contrast Formation in the SEM in *A Beginners' Guide to Scanning Electron Microscopy*, New York City, Springer Publishing Company, 77-128. ISBN: 978-3-319-98482-7.

[148] TIKANEN, A. *Vickers hardness, mineralogy.* Encyclopedia Britannica. Available from: https://www.britannica.com/science/Vickers-hardness. [1.05.2024].

[149] WILLIS, D. J., LAKE, J. S. (1987). Measurement of grain size using the circle intercept method. *Scripta Metallurgica,* **21**, 1733-1736.

[150] CIESLAR, M., KŘIVSKÁ, B., KRÁLÍK, R., BAJTOŠOVÁ, L. (2022). HOMOGENIZATION OF TWIN-ROLL CAST AL-LI-BASED ALLOY STUDIED BY IN-SITU ELECTRON MICROSCOPY in: *Proceedings 31st International Conference on Metallurgy and Materials, Brno, Czechia, May 18-19,* 593-598. ISBN: 978-80-88365-06-8.

[151] TOMKEIEFF S. I. (1945). Linear Intercepts, Areas and Volumes. *Nature,* **24**, 155.

[152] XU, C., XIAO, W., ZHENG, R., HANADA, S., YAMAGATA, H., MA, C. (2015). The synergic effects of Sc and Zr on the microstructure and mechanical properties of Al–Si–Mg alloy. *Materials and Design,* **88**, 485-492.

[153] PRACH, O., TRUDONOSHYN, O., RANDELZHOFER, P., KORNER, C., DURST, K. (2020). Multi-alloying effect of Sc, Zr, Cr on the Al-Mg-Si-Mn high-pressure die casting alloys. *Materials Characterization,* **168**, 110537.

[154] PEET, M. J., HASAN, H. S. BHADESHIA, H. K. D. H. (2011). Prediction of thermal conductivity of steel. *International Journal of Heat and Mass*

Transfer, **54**, 2602-2608.

[155] GRYDIN, O., STOLBCHENKO, M., SCHAPER, M., BELEJOVÁ, S., KRÁLÍK, R., BAJTOŠOVÁ, L., KŘIVSKÁ, B., HÁJEK, M., CIESLAR, M. (2020). New Twin-Roll Cast Al-Li Based Alloys for High-Strength Applications. *Metals,* **10**, 987.

[156] FLEMINGS, M. C., Solidification processing. *Metallurgical transactions,* **5**, 2121-2134.

[157] WANG, L. (2018). Influence of Homogenization on Microstructural Response and Mechanical Property of Al-Cu-Mn Alloy. *Materials,* **11**, 914.

[158] QI, Y., ZHANG, H., NIE, X., HU, Z., ZHU, H., ZENG, X. (2020). A high strength Al–Li alloy produced by laser powder bed fusion: Densification, microstructure, and mechanical properties. *Additive manufacturing,* **35**, 101346.

[159] STEFANESCU, D. M., RUXANDA, R. M. (2004) *Fundamentals of solidification*. ASM International, Detroit, USA. ISBN: 978-1-62708-177-1.

[160] GIANOGOLIO, D., CIFTCI, N., ARMSTRONG, S., UHLENWINKEL, V., BETTEZATI, L. (2021). On the Cooling Rate-Microstructure Relationship in Molten Metal Gas Atomization. *Metallurgical and Materials Transactions: A,* **52**, 3750 – 3758.

[161] SARREAL, J. A., ABBASCHIAN, G. J. (1986). The Effect of Solidification Rate on Microsegregation. *Metallurgical Transactions A,* **17**, 2064-2073.

[162] ZHANG, F., SHEN, J., YAN, X., SUN, J., SUN, X., YANG, Y. (2014). Homogenization heat treatment of 2099 Al-Li alloy. *Rare Metals,* **33**, 28-36.

[163] CIESLAR, M., BAJER, J., ZIMINA, M., ŠLAPÁKOVÁ, M., GRYDIN, O. (2017). Properties and microstructure of twin-roll cast Al-Mg alloy containing Sc and Zr. *IOP Conference Series: Materials Science and Engineering*, **179**, 012012.

[164] HUMPHREYS, J., ROHRER, G. S., ROLLET, A. (2004). *Recrystallization and Related Annealing Phenomena*; 2nd edition, Amsterdam, Netherlands: Elsevier. ISBN: 978-0-08-044164-1.

[165] LIU, Q., FAN, G., TAN, Z., LI, Z., ZHANG, D., WANG, J., ZHANG, H. (2021). Precipitation of Al3Zr by two-step homogenization and its effect on the recrystallization and mechanical property in 2195 Al–Cu–Li alloys. *Materials Science and Engineering: A,* **821**, 141637.

[166] WATANABE, C., WATANABE, D., MONZEN, R. (2006). Coarsening Behavior of Al3Sc Precipitates in an Al–Mg–Sc Alloy. *Materials Transactions,* **47**, 2285-2291.

[167] ROBSON, J. D., PRANGNELL, P. B. (2003). Modelling Al3Zr dispersoid precipitation in multicomponent aluminium alloys. *Materials Science and*

Engineering: A, **352**, 240-250.

[168] DING, Y., GAO, K., GUO, S., WEN, S., HUANG, H., WU, X., NIE, Z., ZHOU, D. (2019). The recrystallization behavior of Al-6Mg-0.4Mn-0.15Zr-xSc. *Materials Characterization,* **147**, 262-270.

[169] HAUSLER, I., SCHWARZE, C., BILAL, M. U., RAMIREZ, D. V., HETABA, KAMACHALI, R. D., SKROTZKI, B. (2017). Precipitation of T1 and θ′ Phase in Al-4Cu-1Li-0.25Mn During Age Hardening: Microstructural Investigation and Phase-Field Simulation. *Materials,* **10**, 117.

[170] HE, G., LI, K., YANG, Y., LIU, Y., WU, W., HUANG, C. (2021) Effect of heat treatment on the microstructure and mechanical properties of cryogenic rolling 2195 Al–Cu–Li alloy. *Materials Science & Engineering A,* **882**, 141682.

[171] ZHANG, P., LI, S. X., ZHANG, Z. F. (2011). General relationship between strength and hardness. *Materials Science and Engineering: A,* **529**, 62-73.

[172] ZHAO, Y., ZHANG, W., YANG, C., ZHANG, D., WANG, Z. (2017). Effect of Si on Fe-rich intermetallic formation and mechanical properties of heat-treated Al–Cu–Mn–Fe alloys. *Journal of Materials Research ,* **33**, 898-911.

[173] XUE, S., FAN, L. Q. Z., WANG, H., ZHANG, Y., DING, J., WANG, H., ZHANG, X. (2018). Strengthening mechanisms and deformability of nanotwinned AlMg alloys. *Journal of Materials Research ,* **33**, 3739-3749.

[174] NIE, J. F., MUDDLE, B. C. (2008). Strengthening of an Al–Cu–Sn alloy by deformation-resistant precipitate plates. *Acta Materialia,* **56**, 3490-3501.

[175] HAUSLER, I., KAMACHALI, R. D., HETABA, W., SKROTZKI, B. (2019). Thickening of T1 Precipitates during Aging of a High Purity Al–4Cu–1Li–0.25Mn Alloy. *Materials,* **12**, 30.

[176] LIU, H., PAPADIMITRIOU, I., XIN, F. X., LLORCA, J. (2019). Precipitation during high temperature aging of Al−Cu alloys: A multiscale analysis based on first principles calculations. *Acta Materialia,* **167**, 121-135.

[177] SHANMUGASUNDARAM, T., HEILMAIER, M., MURTY, B. S., SUBRAMANYA SARMA, V. (2010) On the Hall–Petch relationship in a nanostructured Al–Cu alloy. *Materials Science and Engineering: A,* **527**, 7821-7825.

[178] BURŠÍK J. (1992). Vliv příměsí na žíhací spektrum deformovaného hliníku. *Disertation thesis, Faculty of Mathematics and Physics, Charles University, Prague.*

[179] CIESLAR, M. (2004). Mikrostrukturní příčiny nehomogenit profilů z polykrystalických hliníkových slitin. *Habilitation thesis, Faculty of Mathematics and Physics, Charles University, Prague.*

[180] LI, Y., LU, B., YU, W., FU, J., XU, G., WANG, Z. (2021). Two-stage homogenization of Al-Zn-Mg-Cu-Zr alloy processed by twin-roll casting to

improve L12 Al3Zr precipitation, recrystallization resistance, and performance. *Journal of Alloys and Compounds,* **882**, 160789..

[181] RODGERS, B. I., PRANGNELL, P. B. (2016). Quantification of the influence of increased pre-stretching on microstructure-strength relationships in the Al–Cu–Li alloy AA2195. *Acta Materialia,* **108**, 55-67.

[182] LADEMO, O., PEDERSEN, K., BERSTAD, T., FURU, T., HOPPERSTAD, O. S. (2007). An experimental and numerical study on the formability of textured AlZnMg alloys. *European journal of mechanics: A,* **27**, 116-140.

[183] SHABADI, R., SUWAS, S., KUMAR, S., ROVEN, H. J., DWARKADASA, E. S. (2012) Texture and formability studies on AA7020 Al alloy sheets. *Materials Science & Engineering A,* **558**, 439-445.

[184] BIROL, Y. (2009). Homogenization of a twin-roll cast thin Al–Mn strip. *Journal of alloys and compounds,* **471**, 122-127.

[185] CHEN, Z., LI, S., JING, Z. (2012). Homogenization of twin-roll cast A8006 alloy. *Transactions of Nonferrous Metals Society of China,* **22**, 1280-1285.

[186] SUN, N., PATTERSON, B. R., SUNI, J. P., SIMIELLI, E. A., WEILAND, H., ALLARD, L. F. (2006) Microstructural evolution in twin roll cast AA3105 during homogenization. *Materials Science and Engineering: A,* **416**, 232-239.

[187] ZHANG, J., LIU, Z., SHI, D. (2022). Hot Compression Deformation Behavior and Microstructure of As-Cast and Homogenized AA2195 Al-Li Alloy. *Metals,* **12**, 1580.

[188] FU, R., HUANG, Y., LIU, Y., LI, H., WANG, Z. Influence of homogenization treatment on microstructure and recrystallization behavior of 2195 Al–Li alloy. *Transactions of Nonferrous Metals Society of China,* **33**, 2255-2271.

List of Figures

List of Tables

List of abbreviations

M – Taylor factor

G – shear modulus

b – Burgers vector

υ – Poisson ration

λ – particle spacing

d – precipitate diameter

t_p – precipitate thickness

f_N, f_V – precipitate number fraction, precipitate volume fraction

Γ – dislocation line tension

(S)DAS – (secondary) dendrite arm spacing

A, n – solidification constants

G_T – thermal gradient

R_D – dendrite tip velocity

V – solidification rate

T – temperature

t – time

x – distance

α, k – thermal diffusivity, thermal conductivity

C – heat capacity

ρ – density

K_1, K_2 – solidification boundary condition constants

δ_1 – melt-spun ribbon thickness

T_{i0} – initial temperature

F – force

d_I, d_1, d_2 – indentation diagonals

GS – grain size

l – circumference in the circular intercept method

L_i – intercepted segment length

N_i – number of intercepted segments

w – particle width

C_x, j_x – general power rule constants

L – diffusion length

D, D_0 – diffusion coefficient, diffusion constant

Q – activation energy

R – gas constant

P_Z – Zener drag

γ – grain boundary energy

r – dispersoid diameter

σ – strength

k_{GS} – Hall-Petch constant

N_P – number of particles

V_P, V_S – volume of a single particle, volume of the observed area

t_S, t_P – sample thickness, precipitate thickness

d_m – measured particle diameter

SSSS – supersaturated solid solution

PFZ – precipitate free zone

SEM, TEM, STEM – scanning, transmission, scanning transmission electron microscopy

BF, DF, HAADF – bright, dark, high angle annular dark field

ECS – eutectic cell size

HRTEM – high-resolution TEM

SFE – stacking fault energy

RS – rapid solidification

TRC – twin-roll casting

RD, ND, TD – rolling, normal, transversal direction

SPD – severe plastic deformation

CGP – constrained groove pressing

ECAP – equal channel angular pressing

SE, BSE – secondary, back-scattered electron

EBSD – electron backscatter diffraction

EDS – energy dispersive X-ray spectroscopy

SAED – selected area electron diffraction